# OBSERVATION OF SURFACE AND MASS TRANSPORT ON SELECTIVELY REDUCIBLE SPINEL OXIDES

BY

ALEC C. LADONIS

A THESIS

SUBMITTED TO THE FACULTY OF

ALFRED UNIVERSITY

IN PARTIAL FULFILLMENT OF THE REQUIREMENTS
FOR THE DEGREE OF

DOCTOR OF PHILOSOPHY

IN

MATERIALS SCIENCE AND ENGINEERING

ALFRED, NEW YORK

DECEMBER, 2020

OBSERVATION OF SURFACE AND MASS TRANSPORT ON SELECTIVELY REDUCIBLE SPINEL OXIDES

BY

ALEC C. LADONIS

B.S. ALFRED UNIVERSITY (2014)

M.S. ALFRED UNIVERSITY (2016)

SIGNATURE OF AUTHOR _____

APPROVED BY _____
SCOTT T. MISTURE, ADVISOR

_____
ALASTAIR N. CORMACK, ADVISORY COMMITTEE

_____
STEVEN C. TIDROW, ADVISORY COMMITTEE

_____
JUNJUN DING, ADVISORY COMMITTEE

_____
YIQUAN WU, CHAIR, ORAL THESIS DEFENSE

ACCEPTED BY _____
GABRIELLE G. GAUSTAD, DEAN
KAZUO INAMORI SCHOOL OF ENGINEERING

ACCEPTED BY _____
DR. BETH ANN DOBIE
PROVOST AND VP FOR ACADEMIC AFFAIRS
ALFRED UNIVERSITY

# ACKNOWLEDGMENTS

Throughout the research and writing process, I've received a great deal of support and assistance. Foremost, some of the materials used in this work were supported by the National Science Foundation under Grant CBET-1033810. Part of this material (Raman data) is based upon work supported by the National Science Foundation under Grant No. DMR-1626164. This work made use of a Helios FIB supported by NSF (DMR-1539918) and the Cornell Center for Materials Research Shared Facilities which are supported through the NSF MRSEC program (DMR-1719875). Without these funding sources, much of the background and main work for this thesis would not be possible.

I would first like to thank my supervisor, Dr. Misture, for allowing me the freedom and flexibility to determine the direction of this work, meanwhile always pursuing a greater understanding of materials science. Under his guidance, I've learned invaluable research and professional skills that I will always remember and attempt to pass on to further generations of scientists.

Next, I would like to thank Gerry Wynick, Jim Thiebaud, Swavek Zdzieszynski, Dr. Darren Stohr for all the technical expertise in their respective areas, as well as ***many*** valuable and a few inefficient conversations. I'd like to thank my committee members, Drs. Steven Tidrow, Alastair Cormack, and Junjun Ding for their valuable input. Dr. Eric Payton was also integral to the inception of this work, in which he initially guided me in this direction.

Dr. Michelene Hall, Dr. Brendan Hill, Kyle McDevitt also deserve credit for preparing some of the samples used in this work, as well as laying the initial groundwork for this thesis. In this vein, all my friends and fellow graduate students past and present at Alfred University deserve thanks for fruitful conversations, help on equipment, and most importantly friendship and comradery throughout my time at Alfred.

I want to also thank my parents for instilling in me the curiousness, perseverance, work ethic, and skills that allowed me to pursue whatever career path I chose. Without their love and support, I would not be where I am today.

Finally, I'd like to thank myself for not giving up, always being curious, and persistently doing things to the best of my ability. This path was extremely mentally and physically taxing, with an array of external challenges, from the loss of 2 advisors to the COVID-19 pandemic. With the support of everyone mentioned above as well as perseverance, I was able to overcome these challenges. I put this here to inspire anyone who is having hardships in their studies, to remind them that they are not alone, and perseverance will eventually pay its dividends. Keep up the hard work, you are almost there, and don't give up.

# TABLE OF CONTENTS

# LIST OF TABLES

**Page**

# LIST OF FIGURES

**Page**

# ABSTRACT

While many investigations rely on macro- or nanoscale techniques to determine the deactivation mechanisms on selectively reducible oxide catalysts, little attention is paid to the surfaces and near-surface effects. This study addresses the literature gap by investigation of a model $NiAl_2O_4$ catalyst by novel low voltage *in-situ* high temperature scanning electron microscopy and other complementary techniques. Extensions to other compositions of Ni bearing aluminate spinel are presented. Expedited mass transport was identified on a bulk scale, on the surface, and around modifying oxide particles by *in-situ* techniques at relevant service $p_{O_2}$ and temperatures.

The regeneration pathway was found to depend on system $p_{O_2}$. Oxidative atmosphere favors NiO formation and reaction with the remnant spinel whereas vacuum favors Ni reincorporation via either reaction at the triple phase boundary or by formation of a core-shell structure. Structural relaxation at the surface is evidenced by Raman spectroscopy, where vacuum reoxidized samples show band sharpening and splitting as compared to the reduced analogue, however, some surface defects are retained.

The unusual nature of the surface of the selectively reduced spinel is highlighted by enhanced surface diffusion in the form of metal particle migration and coalescence, which was observed on the spinel above the reduction temperature. Comparison of Ni migration distances on two supports with varied defect content exhibit diffusional distances up to 350 times the predicted value. Additional surface pits are revealed during migration and coalescence, which are crystallographically registered to the spinel. These features do not heal; however, they sharpen with extended time at high temperature.

Extensions to technologically relevant Ni-Mg-Co catalysts show that phase assemblages during redox cycling are indeed reversible. Morphological changes during reduction and oxidation were proven to be irreversible, creating new features on each reduction. The catalyst upon the second reduction exhibits 50% more exsolved metal, a 4x increase in particle number density, and over a 50% decrease in particle size as compared to the initial reduction. Irreversible changes in the surface metal dispersion and surface area are attributed to microstructural maturation, where surface features promote better metal dispersion and surface area for catalytic reactions.

A unique and unusual tunneling phenomenon was identified at the interface of the spinel and modifying oxide at elevated temperatures, implying the process is thermally activated. Changing the modifying oxide from $ZrO_2$ to $HfO_2$ increased the onset temperature by 200°C but had similar rates. Further investigation of the interface revealed non-homogeneously distributed voids form beneath the tunneled $ZrO_2$, where the interface between the spinel and $ZrO_2$ is Ni deficient, reminiscent of a defective spinel structure. A model is proposed based on enhanced interfacial diffusion, where voids occur due to variations in the magnitude of diffusional fluxes arising from the modifying oxide additions.

# GRAPHICAL ABSTRACT

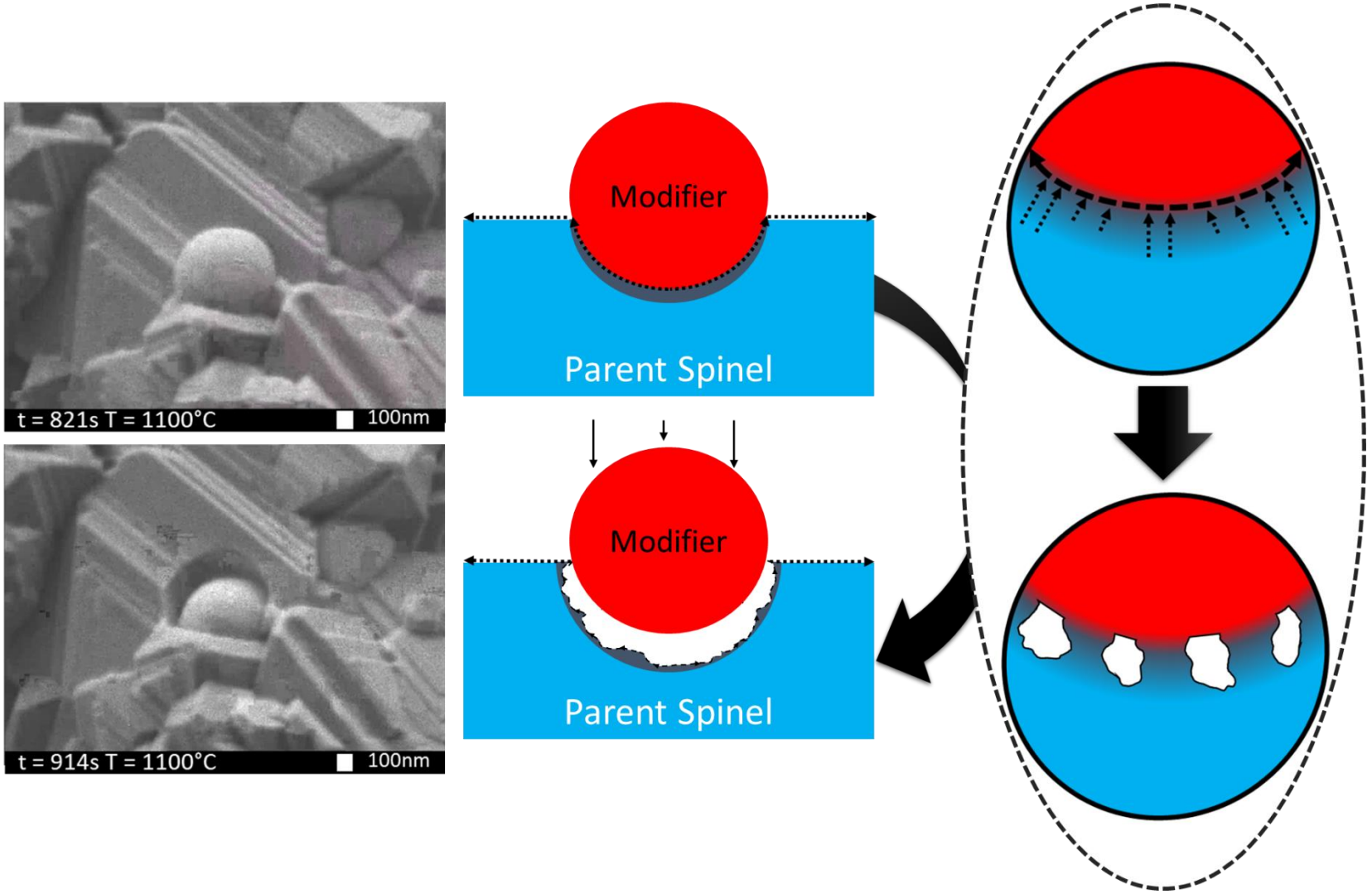

# I. INTRODUCTION

## A. Motivation

Energy demand worldwide is increasing by the year, with non-renewable resources as the dominant energy source. Approximately 82% of the United States' total energy consumption was attributed to non-renewable fossil fuels in 2015.[1] With the depletion of the reserves of fossil fuel, clean energy has been an area of intense interest. A movement toward utilizing renewable and nuclear energy sources has been growing, but they still only account for 17% and 20% respectively of the total US consumption as of 2017.[2] Engineering new materials for $H_2$ fuel production and energy storage have been at the forefront of materials research, driving innovations.

Metal-supported ceramic composites derived from reducible oxides are the focus of catalysis studies in which, at operation temperatures, reduced metal particles are deactivated via contamination or by particle sintering, ultimately destroying the catalytic activity. Regeneration of the catalyst can occur by oxidation of the contaminating species and metal, which reacts with the support, creating the original phase. Both deactivation and regeneration occur on the surface of the oxide, therefore it is paramount to understand the mass transport and surface mechanisms of these two reactions as they occur *in-situ*.

## B. Catalysts – Early Work and Material Selection

A catalyst is, by definition, an accelerant to a chemical reaction that alters the activation energy of that reaction but does not undergo a permanent change throughout the chemical process. A depiction is shown in Figure 1. Scholars throughout the 1700s such as Joseph Priestley, Martinus van Marum, Louis Jacques Thénard, and Pierre Dulong pioneered this work although the first concise revelation of metal catalysts was by Humphry Davy in 1817.[3] Commercial use ensued just 20 years after Davy's discovery, for ammonia oxidation over Pt to form nitric acid by similar catalytic means.[4]

Active phase transition metals are typically used due to the best reforming activities (the most efficient) attributable to their ability to vary oxidation state or to absorb compounds on their surface. Following the lead of Davy's research with platinum, precious metals were heavily researched along with nickel, cobalt, copper, iron, and zinc.[5-9] From

these studies, it was found that Rh, Ni, and Pt were the best catalysts in terms of activity. Due to the high costs of Rh and Pt, Ni-based catalysts have emerged to be the front runner in research for industrial applications.

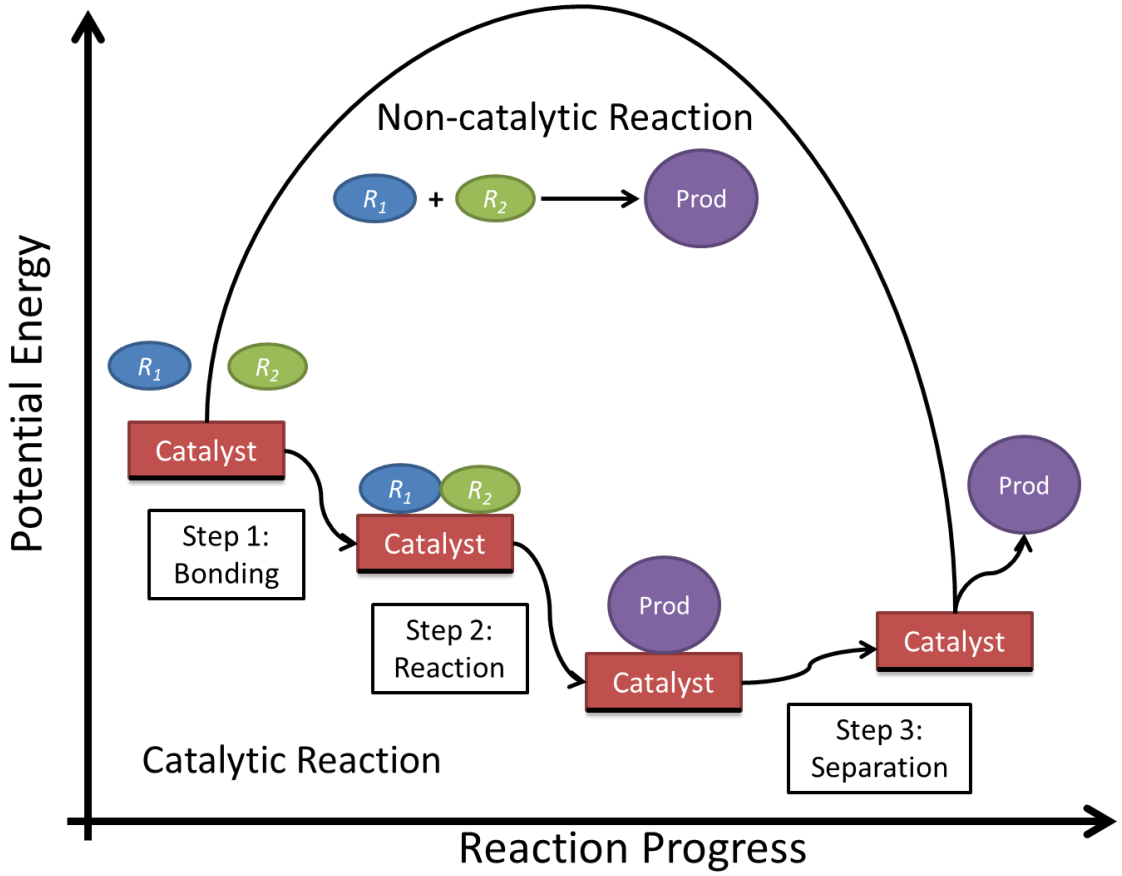


**Figure 1: Schematic of the catalytic and non-catalytic processes as a function of potential energy as the reaction progresses.**

Owing to low cost and high activity, nickel-based catalysts are the most common among researchers but must be supported on stable substrates at high temperatures. Alumina ($Al_2O_3$) supports have been commonly used for natural gas and steam reforming but falter with reforming biomass and syngas (CO and $H_2$ mixture) due to contamination. Biomass and syngas are hot topics for energy concerns; many researchers have either switched to different supports or have attempted to modify the alumina structure for compensation. Many other metal oxides and minerals have been studied such as $CeO_2$ (ceria), dolomite, olivine, sand, perovskite, $MnO_2$, $TiO_2$, YSZ (yttria stabilized zirconia), and zeolites (aluminosilicates). A concise table of these can be found in the review paper

by Yung et al.[10] Spinel has been identified as an ideal system due to the ability of the crystal lattice to accommodate catalytically active cations which can be selectively reduced out of the parent oxide with advantageous properties for catalytic reactions.

Spinel reduction allows the possibility of point defects, which have been masterfully demonstrated through a series of papers from the Neagu and Irvine group[11-17] as well as others.[18] Most notably, exsolved metallic particles exhibit "chemistry at a point", which allows for tailorable compositions and morphologies while retaining the initial spatial arrangement, with catalytic activity rivaling analogous Pt-based model systems with better deactivation resistance.[15]

## C. Structure of Spinel

The general chemical formula of spinel is $AB_2X_4$ where A and B are metals and X is an anion to maintain charge neutrality. Spinel is considered a simple structure type; however, this is an oversimplification as the structure is quite complex, accounting for site rearrangement and cation substitution. Typically, the metallic A and B cations have +2 and +3 charges, residing on the tetrahedral and octahedral sites, respectively. The anion, X, is typically oxygen, however, chemistries containing chalcogenides have been synthesized.[19] Crystallizing in a face-centered cubic Bravais lattice and space group $Fd\bar{3}m$ (International Crystallographic Tables number 227), spinel consists of a basis of two formula units and a unit cell of 8 formula units, resulting in 32 anions and 24 cations. With 64 tetrahedral and 32 octahedral interstices for the anions, only 16 octahedral and 8 tetrahedral interstices are occupied. Figure 2 exhibits two perspectives of the spinel structure highlighting the differing cation coordination. Two points of origin can be envisioned for this space group, $\bar{4}3m$ and $\bar{3}m$; the latter will be used in this work. For this choice of origin, the tetrahedral and octahedral sites are special positions, located at x = y = z = 0.125 (Wycoff position 8a), and x = y = z = 0.5 (Wyckoff position 16d) respectively.[20]

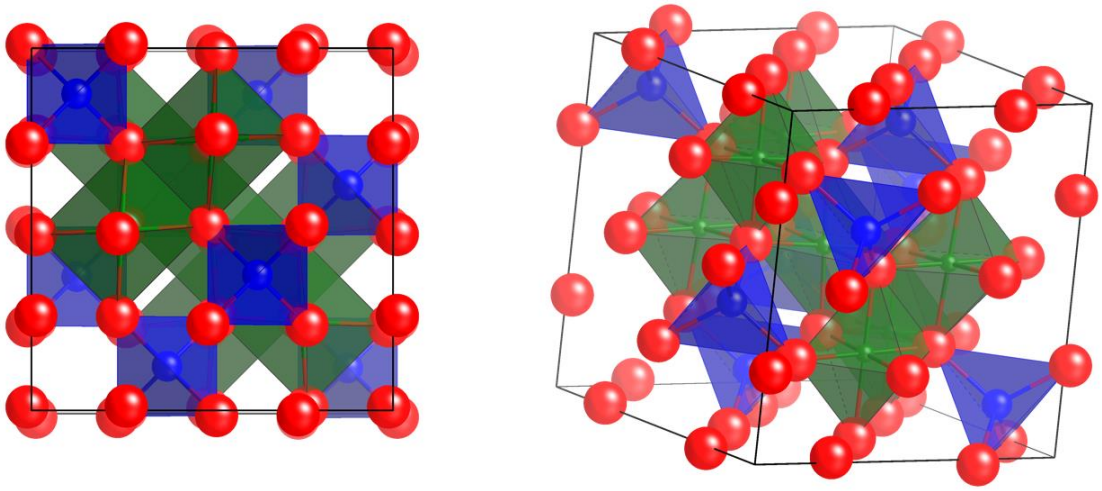

**Figure 2: General unit cell of spinel. Left: [001] perspective, Right: tilted perspective. Red atoms represent oxygen while blue and green represent cations. Colors emphasize octahedral (green) vs. tetrahedral (blue) coordination.**

Assuming oxygen as the anion, an ideal lattice consists of a cubic close packing (CCP) direction along the [111] trace, although non-stoichiometry creates deviations in this ideal case. Three parameters have been devised to describe the degrees of freedom in the spinel lattice to account for the wide array of compositions and stoichiometries: the lattice parameter, *a*, the inversion parameter, *i*, and the anion parameter, *u*. Structural parameters for two typical spinel compounds, $NiAl_2O_4$ and $MgAl_2O_4$, are shown in Table I. Ni containing spinel has a larger density, but smaller lattice parameter compared to the Mg spinel due to the atomic weight of Ni compared to Mg. A difference of note is in the inversion parameter, where the Ni spinel is highly inverse comparatively to the relatively normal Mg spinel. The amount of inversion has been linked to the long equilibration time for the cation distribution at low synthesis temperatures, varying the reported parameter with heat treatment.

**Table I: Structural parameters for two common spinel chemistries.**

| | $\rho\ \left[{}^{g}/_{cm^3}\right]$ [21] | Lattice Parameter ($a$) [Å] [22, 23] | Oxygen Parameter ($u$) [22, 24] | Inversion Parameter ($i$) [24, 25] |
|---|---|---|---|---|
| $MgAl_2O_4$ | 3.58 | 8.083 | 0.2624 | 0.05-0.33 |
| $NiAl_2O_4$ | 4.5 | 8.045-8.048 | 0.254-.0256 | 0.86-0.9 |

Spinel has an inherently large lattice parameter, $a$ = 8.083 Å and 8.045-8.048 Å for $MgAl_2O_4$ and $NiAl_2O_4$, respectively.[22, 23] Inversion is represented by the parameter $i$, which is mathematically represented by the fraction of B cations occupying the tetrahedral sites over the total amount of tetrahedral sites. Classes of spinel inversion are regular, random, and inverse having corresponding values of $i$ = 0, $i$ = 0.66, and $i$ = 1, respectively. In normal spinel where $i$ = 0, A cations occupy all tetrahedral sites and some octahedral sites whereas B cations are in octahedral coordination. Random spinel is defined as when 66% of the B cations are tetrahedrally coordinated, resulting in an $i$ = 0.66. Inverse spinel is defined to be when the B cations occupy the tetrahedral sites, with equally distributed A and B cations on the octahedral sites. Inversion parameters of real spinel vary between normal and inverse, and are contingent on composition, synthesis pressure and temperature, ionic charge, ionic radius, and anion polarization.[23, 26-28] Recently, local inversion has been shown via neutron diffraction and Pair Distribution Function analysis on $Ni_xMg_{1-x}Al_2O_4$ to change the local symmetry to a tetragonal space group ($P4_122$), where the solid solution series is best modeled as a mixture of cubic $Fd\bar{3}m$ + tetragonal $P4_122$ for the interatomic distances.[29] Although thorough, an in-depth description of the local atomic disorder is beyond the scope of this investigation.

The oxygen parameter, $u$, ranges from 0.24 to 0.275 where a value of 0.25 represents perfect close packing along the [111] direction trace for $\bar{3}m$ symmetry. This value is derived from the tetrahedral and octahedral bond lengths.[22, 27] Deviations from the ideal close packing value are derived from the oxygen anion relocating along the [111] degenerating symmetry, where the tetrahedral site expands resulting in the shrinkage of the octahedral site. Mathematically, O'Neill and Navrotsky have expressed the octahedral and tetrahedral cation-anion bond lengths in terms of the oxygen and lattice parameter shown in Equations (1) and (2).[27]

$$R_{tet} = a\sqrt{3\left[u - \frac{1}{8}\right]} \quad (1)$$

$$R_{oct} = a\sqrt{3u^2 - 2u + \frac{3}{8}} \quad (2)$$

## D. Non-Stoichiometric Spinel

Both $MgAl_2O_4$ as well as $NiAl_2O_4$ can accommodate non-stoichiometry. In the case of $MgAl_2O_4$, excess MgO and $Al_2O_3$ can be incorporated, however, less MgO can be accommodated than $Al_2O_3$ and requires higher temperatures. Excess $Al_2O_3$ is compensated by randomly distributed cation vacancies,[30, 31] and possibly some additional anion vacancies.[32-34] $NiAl_2O_4$ does not incorporate excess NiO; however, $Al_2O_3$ can be dissolved to a limited extent.[35] Excess $Al_2O_3$ causes the lattice parameter to shrink for both compositions.[30, 36-38]

Okuyama et al. propose a defect model in which excess $Al_2O_3$ creates not only $V''_{Mg}$, but also oxygen vacancies by way of Equation (3).[32]

$$17Al_2O_3 \rightarrow 5V''_{Mg} + 8Al^{\cdot}_{Mg} + 26Al_{Al} + 51O_O + V^{\cdot\cdot}_O \quad (3)$$

In support of this work, Reddy and Cooper have demonstrated that $Al_2O_3$ excess spinel exhibits increased oxygen diffusion compared to the stoichiometric analog.[33] Ting and Lu came to the same conclusion as Okuyama et al. by evaluation of sintering kinetics and construction of a Brouwer diagram.[39]

## E. Metastable Spinel Phases

Metastable structures based on spinel have been studied by a few groups. These can all be described as having cubic pseudosymmetry, with a slightly distorted cubic close-packed array of oxygen with a corresponding disorder of cation vacancies.[35, 40-46] A compilation of the metastable phases are shown in Table II. Bassoul and Gilles propose a periodic antiphase boundary based on electron diffraction observations, where up to twelve twin and eight translation variants based on the ideal spinel structure are present.[44, 45] Based on their findings and others' work,[35, 40-43] a phase diagram between $NiAl_2O_4$ and $Al_2O_3$ was constructed, in which all the stable and metastable spinel phases are shown. The phase diagram shows the spinel phase-field extends almost to pure $Al_2O_3$ at high temperatures (≥1900°C). Metastable phases with stoichiometries of $NiO{\cdot}xAl_2O_3$ (x = 3.0, 5.0, 9.0, 13.0, 16.0) are shown as metastable line compounds as the NiO content is decreased. The only high-temperature phase field is between ε and A phases, which is compositionally small and only occurs at temperatures around 1750°C.

**Table II: Compilation of metastable spinel data.**

| Stoichiometry | Phase Name | Bravais Lattice | Space Group | PDF# | Reference |
|---|---|---|---|---|---|
| $NiAl_6O_{10}$ | A | Monoclinic | - | - | [42] |
| $NiAl_{10}O_{16}$ | B | Monoclinic | $P2_1/b$ | 00-037-1292 | [44, 45] |
| $NiAl_{10}O_{16}$ | ε | Monoclinic | - | - | [43] |
| $Ni_2Al_{18}O_{29}$ | - | - | - | 00-022-0451 | [41] |
| $NiAl_{26}O_{40}$ | $\delta_3$ | Tetragonal | - | 00-020-0776 | [40] |
| $NiAl_{32}O_{49}$ | φ | Monoclinic | - | 00-020-0777 | [40] |

## F. Transition Aluminas

With the most stable phase being corundum ($\alpha$-$Al_2O_3$), alumina has rich polymorphism, with many metastable compounds such as $\chi$, $\lambda$, $\kappa$, $\eta$, $\gamma$, $\delta$, $\theta$, and $\beta$, which are referred to as transition aluminas. $\beta$-$Al_2O_3$ which has multiple forms, is an alkali alumina with the $\beta''$ phase having a stoichiometric composition of $Na_2MgAl_{10}O_{17}$ and is used as a fast ion conductor.[47] Due to the necessity of additional cations needed to charge balance the structure, $\beta$-$Al_2O_3$ is not considered further. The term transition alumina derives from the dehydration of bayerite and boehmite, $\alpha$- and $\gamma$-$Al(OH)_3$ respectively, which follows the following phase transitions to corundum:.[48, 49]

$$bayerite \rightarrow \eta \rightarrow \theta \rightarrow \alpha$$

$$boehmite \rightarrow \gamma \rightarrow \delta \rightarrow \theta \rightarrow \alpha$$

Transition aluminas can be divided into two categories, based upon the arrangement of oxygen: as a CCP or as a hexagonal close-packed (HCP) arrangement. Cation positions within these oxygen arrangements differentiate between the polymorphs.[48] $\gamma$, $\eta$, $\theta$, and $\delta$-$Al_2O_3$ fall into the CCP derived category whereas $\alpha$, $\kappa$, and $\chi$-$Al_2O_3$ crystallize with HCP arrangements of oxygen. Spinel structure analogues are all the CCP transition alumina, apart from tetragonal $\theta$-$Al_2O_3$. This structure is initially akin to the spinel structure, though with time undergoes a reconstruction of the tetrahedral Al sublattice causing the collapse of the spinel structure to its monoclinic form and eventually conversion to corundum.[50] The previous sequences begin as hydrated states, then transition to spinel-like polymorphs

and then eventually to $\theta$- and $\alpha$-$Al_2O_3$. Specific surface area also decreases through the transition from $\gamma$- to $\alpha$-$Al_2O_3$, from 194 to 4 $m^2g^{-1}$, respectively, which decreases the functionalization in catalysis.[49, 51, 52]

$\gamma$- and $\eta$-$Al_2O_3$ have been described as defective spinel-like structures, modeled in the $Fd\bar{3}m$ space group. For the $\gamma$-$Al_2O_3$, it is assumed that $8/3$ Al (per formula unit) charge balance the structure and are randomly distributed, creating local disorder on the cation sublattice while the oxygen sublattice is fully occupied.[53] Site preference for the vacancies has been of some debate, where some methods show mixed site preference[50, 54, 55] while others show preference to vacancies on octahedral positions.[56] Recently, in-depth structural analysis has been applied to commercially produced $\gamma$-$Al_2O_3$ derived from boehmite where octahedral coordination was shown to be preferred via $^{27}$Al magic-angle-spinning nuclear magnetic resonance (MAS-NMR).[57] Furthermore, via synchrotron pair distribution function (PDF) analysis, local structure on a ≈1nm scale was modeled by a tetragonal motif while the long-range structure was better modeled with a traditional cubic lattice,[57, 58] which has been even more recently proposed for $Ni_xMg_{1-x}Al_2O_4$.[29, 59] A substantial amount of octahedrally coordinated Al was also found to be distributed over non-spinel sites; specifically, the 8c position in a Tetragonal-8c model used by Paglia et al. to determine the average local structure of $\gamma$-$Al_2O_3$.[58] These findings are also supported by Raman spectra of spinel, where additional phonon modes were observed consistent with local tetragonal symmetry.[60, 61] Results such as these give credence to neutron diffraction studies of Zhou and Snyder, where nearly no site preference for Al was found between octahedral and tetrahedral coordination; however, 25% of the cations were found on a quasi-octahedral site attributable to surface energy considerations.[50]

Nevertheless, disagreement within the literature is expected as transition aluminas are notorious for being poorly crystalline, as evidenced by broadened peaks in their diffraction patterns. Processing and measurement considerations can drastically affect the defect content as well as distribution, making structural solutions inherently difficult. Also, transitions between metastable alumina phases are continuous rather than at discrete temperatures. All these considerations factor into the elucidation of the transition alumina structures, which for the moment is still lacking within the literature.

## G. Relationship Between Transition Aluminas and Metastable Spinel

The transition of the metastable spinel eventually to corundum is analogous to the phase transformations of the transition aluminas, in the sense that a defective spinel structure is transitioning to the stable $\alpha$-$Al_2O_3$ polymorph by the removal of selectively reduced cations. Specifically, $\gamma$-$Al_2O_3$ is a poorly crystalline alumina rich defect spinel or remnant spinel which can be obtained by the selective reduction of Ni from $Ni_xMg_{1-x}Al_2O_4$,[62] and will be considered henceforth as such. Metastable spinel phases are typically regarded as transitional states between spinel and corundum,[44] which can be related to the phase progression of transition alumina.

In the following sections, $\gamma$-$Al_2O_3$, defect spinel, remnant spinel, and metastable spinel are used interchangeably, as the experimental distinction between the three terms is ambiguous. The ambiguity is directly related to the point defect content, which is inherently difficult to quantify and beyond the scope of this work.

## H. Reduction Process

Reduction is an essential processing step to creating the metal catalyst from the parent oxide host. Reduction of $NiAl_2O_4$ is prevalent within the literature,[62-70] as Ni is a relatively cheap catalytically active metal that is reducible at low temperatures and $Al_2O_3$ is thermally stable and can accommodate non-stoichiometry. $MgAl_2O_4$ is much harder to reduce at modest temperatures as is evident by simple investigation of the Ellingham Diagrams, where $\Delta H_f^{NiO} < \Delta H_f^{MgO}$. Little work has been done on selectively reduced $Ni_xMg_{1-x}Al_2O_4$ outside of our group; however, an investigation by Quénard et al. examines Ni and Co substitutions for Mg and the effects of particle size and oxidation state.[70]

Previous work by our group at Alfred University has investigated the $Ni_xMg_{1-x}Al_2O_4$ system, where $V_{Ni}''$ and $V_O^{\bullet\bullet}$ were found to remain in the spinel until metastable remnant spinel is formed,[62] which is also supported in other works.[32, 70] Roh et al. combined an alumina phase with magnesia (MgO) to attempt to minimize Ni deactivation from contaminants within syngas.[71] The new Ni/MgO-$Al_2O_3$ catalyst was compared to the commercially available Ni/$MgAl_2O_4$ catalyst, showing approximately 20% improvement on $CH_4$ and $CO_2$ conversion while decreasing the coke formation. B.E. Hill shows a thermodynamic assessment of the series $Ni_xMg_{1-x}Al_2O_4$ + 2.5 wt. % $ZrO_2$, demonstrating

the stability with respect to composition and temperature.[72] It was established that closed system reduction at temperatures exceeding 900°C exhibits metastable spinel phases for the x=1 and x=0.75 compositions while other stoichiometries are stable to 1100°C. It is of note that the x=0.75 sample is also unstable at 900°C which is due to Ni reduction kinetics for this composition.

During reduction, it has been shown via neutron diffraction that oxygen vacancies are expelled to the surface, where the Al cations redistribute as Ni is removed, forming the non-stoichiometric remnant spinel.[65] Vacancies most likely diffuse in a codependent manner to high energy features (cracks, pores, or the surface) to maintain local charge neutrality. The oxygen parameter also increased above ideality ($u$ = 0.25), indirectly implying that the spinel becomes less inverse during the reduction, as expected by $Ni^{2+}$ removal from octahedral sites. Furthermore, the reduction proceeds via nucleation and growth, most likely in a core-shell configuration as evidenced by dual spinel peaks in the neutron diffraction data during the progression of the reaction. The reduction process is demonstrated by Equation (4), showing the Ni removal from the spinel, and the resulting non-stoichiometric remnant spinel. This equation assumes that all the Ni is removed which is an oversimplification and does not completely reflect the fact that some Ni remains in the non-stoichiometric spinel upon reduction.

$$xH_2 + Ni_xMg_{1-x}Al_2O_4 \rightarrow xNi + Mg_{(1-x)\left(\frac{4}{4-x}\right)}Al_{2\left(\frac{4}{4-x}\right)}O_{4-x} + xV_{Ni}'' + xV_O^{\cdot\cdot} + xH_2O \quad (4)$$

Two types of reductions are available: closed system reductions as well as flowing reductions. Closed system reductions have limitations related to factors such as system mass or volume, temperature gradients, and moisture content determining the microstructure of the reduced product. When a closed reduction process is initiated, the system is typically purged with $N_2$ for air and $H_2O$ removal, then evacuated and heated. Once the predetermined temperature is reached, the reducing gas is introduced which will increase the ratio of reducing gas to $H_2O$. From this, the $p_{O_2}$ of the system can be determined as a function of temperature with Equations (5)-(9).

$$2H_2(g) + O_2(g) \leftrightharpoons 2H_2O(g) \quad (5)$$

$$\Delta G^{\circ} = -RTln(K_p) \quad (6)$$

$$K_p = \frac{\left(p_{H_2O}\right)^2}{\left(p_{H_2}\right)^2\left(p_{O_2}\right)} \tag{7}$$

$$p_{O_2} = e^{\frac{-\Delta G^\circ}{RT}}\left[\frac{\left(p_{H_2}\right)^2}{\left(p_{H_2O}\right)^2}\right] \tag{8}$$

$$H_2 + Ni_{Ni}^0 + O_O^0 \rightarrow H_2O + Ni^0 + V_{Ni}^{''} + V_O^{\cdot\cdot} \tag{9}$$

Equation (9) will progress forward as the oxygen pressure is below the dissociation pressure, consuming $H_2$ to yield $H_2O$. Equation (5) will shift to establish equilibrium, consequently increasing the $p_{O_2}$ of the ensemble decreasing the reaction kinetics. A drop in the reaction rate and increased diffusion distances allows the formation of a reaction layer, a diffusional barrier deficient of oxygen, where equilibrium is achieved once the net flux of oxygen through the barrier is zero. In theory, X moles of $H_2$ will reduce X moles of Ni, assuming the $p_{O_2}$ is below the dissociation pressure of the spinel, and the moles of Ni present is equal to the number of moles of $H_2$. These factors depend on sample mass, sample position in the furnace, furnace volume, and pressure.

Under flowing conditions, the reaction gas is pumped into the chamber while the reacted gas is swept away keeping the $p_{O_2}$ constant for any specific temperature. For Equation (5 to progress, the oxygen fugacity must be less than the dissociation pressure for the phases present.

Elrefaie and Smeltzer have determined equilibrium phase diagrams for both the Ni-NiO system as well as the $NiAl_2O_4$ + NiO – $NiAl_2O_4$ + Ni systems between 850 and 1150°C.[73] At 1000°C, equilibrium is reached in the spinel system when the $p_{O_2}$ reaches $3.76 \cdot 10^{-11}$ atm, which is slightly less than of the Ni-NiO system at a $p_{O_2}$ of $4.48 \cdot 10^{-11}$ atm at the same temperature. Ni-Al alloys were found to form only when the $p_{O_2}$ reached $10^{-23}$ atm. A later study by Taylor and Dinsdale showed that the small discrepancy in equilibrium pressure is much larger than originally estimated by Elrefaie and Smeltzer, demonstrating that at 1055°C an equilibrium is reached between Ni and NiO at a $p_{O_2}$ of $2 \cdot 10^{-10}$ atm which has been corroborated by others.[74, 75] $Ni^{2+}$ extraction (and subsequently $O^{2-}$) from the spinel structure unveils a defective non-stoichiometric spinel crystal structure that is rich in non-reduced ions ($Al^{3+}$, $Mg^{2+}$, etc.) which is dependent on the $p_{O_2}$ and reduction temperature.

Microstructurally, the extracted reduced metal is decorated on the surface. If it is assumed that the Ni content is x=1, then the remnant spinel structure can be described as an alumina rich spinel with cation vacancies and an oxygen sublattice resembling the spinel like γ-alumina structure.[62]

Since supports with high surface area are critical for catalytic activity, structures can be tailored to increase the surface area and be stable at the high temperatures needed for catalysis reactions. $\gamma$-alumina has been used in catalytic applications due to its high thermal stability as well as high surface area.[76, 77] It has been shown that the γ-alumina structure undergoes transitions to a mixture of γ + θ phases at 900°C, then to a mixture of θ + α phases at 1100°C, and finally to corundum at 1300°C, with decreasing surface area throughout the transition, from 194 to 4 $m^2/g$ for γ to α-alumina.[49, 52] It is advantageous to maintain the cubic oxygen sublattice as it requires lower temperatures and therefore less energy for parent phase regeneration.

## I. Catalyst Deactivation

Deactivation of the catalyst may occur in various manners, depending on the application. For Ni-based catalysts, typical uses are for the reforming of carbonaceous gas species for $H_2$ production, which requires high temperatures. This presents a few challenges, as the catalyst can be deactivated by thermal, mechanical, and chemical means. The most common mechanisms are poisoning/fouling, thermal degradation/sintering, and vapor/solid-solid reactions. As the subject of deactivation has breadth and depth, only a brief overview of mechanisms that pertain to Ni spinel catalysts will be discussed. Extensive reviews by Bartholomew and Argyle are recommended for further reading.[78, 79]

Poisoning/fouling can be defined as the chemisorption or deposition of reactants, intermediates, or products from the catalytic reaction, which blocks the otherwise active sites, thus reducing the catalytic activity. In Ni-based catalysts, specifically in the methane reforming reaction, carbon and sulfur deposition are the main deactivation species. Carbon can accumulate in thin monolayers in the mild case, and in an extreme case can envelop the Ni metal particles and even remove Ni particles completely from the support. Sulfur poisoning comprises of a complex interplay between temperature, $H_2S$ concentration,

sulfur coverage on the catalytically active sites, and pretreatment, making the phenomenon inherently difficult to thoroughly characterize due to the number of variables.

Thermal degradation can be either the loss of catalytic surface area for reactions to occur via crystallite growth, the loss of support area, or by the chemical transformation of catalytic to noncatalytic phases. Particle sintering on analogous Ni/$\theta$-$Al_2O_3$ and Ni/$MgAl_2O_4$ catalysts have been extensively characterized by Sehested and coworkers,[76, 80-82] and recently investigated via *in-situ* TEM by the Hansen and Crozier groups for other systems as well.[80, 83-87] The previous studies identify migration and coalescence, Ostwald ripening, and vapor transport mechanisms result in increases in catalytic particle size based on time, temperature, pressure, and gas composition.

The support thermal degradation considerations have already been discussed, as a transition from spinel-like $\gamma$-$Al_2O_3$ to $\theta$- or $\alpha$-$Al_2O_3$. This directly implies that the retention of the CCP oxygen sublattice is paramount to regenerating the parent spinel phase and retaining the specific surface area, which is directly related to catalytic particle dispersion and catalytic activity. Preservation of the oxygen sublattice will also have implications during the regeneration process.

Vapor-solid or solid-solid reactions can also degrade the catalytic activity, resulting in catalytically inactive phases. Formation of $Ni(CO)_4$ via reaction with gaseous CO produced by methanation or chemisorption can degrade the catalytic activity under extreme reforming conditions.[88, 89] It is also not difficult to envision that bulk reactions or diffusion of the catalytic material may be enhanced by changes in the pressure, oxygen content, temperature or even by the nucleation of secondary phases due to solid-solid reactions during deactivation processes.

## J. Regeneration Process

Regenerable catalysts that can remove carbon and sulfur contaminants provide advantages in cost reduction due to the active materials typically being noble metals or transition metals that tend to be expensive. Contaminant removal is imperative to maintain catalytic activity as carbon and sulfur deposition reduce and eventually eliminate the active sites. Oxidative regeneration removes the contaminants and recombines the deactivated

metal or metal oxide with the support, obtaining the parent phase with small degeneration of catalytic activity. The oxidative regeneration equation is shown in Equation (10).

$$Ni_{1-x}Al_2O_{4-x} + xNi + \frac{x}{2}O_2 \xrightarrow{O_2+heat} xNiO + Ni_{1-x}Al_2O_{4-x} \xrightarrow{time+heat} NiAl_2O_4 \quad (10)$$

Regeneration processes are dependent upon structure and composition which vary throughout the literature.[64, 90, 91] The regeneration process begins with a reducible oxide host that will eventually become the support decorated with catalytically active metal particles. This concept was first pioneered by Tanaka et al. for precious metal-based perovskite automotive catalysts.[92] Reduction yields a defective oxide support matrix with metallic particles decorating the surface. These metal particles are deactivated as previously explained but can be reincorporated with the defective support by supplying sufficient heat and oxygen to obtain the original or "parent" phase without contaminants. The subsequent process of thermal impregnation was developed by Felix and coworkers for glassy oxide supports.[93, 94]

Parent phase regeneration is only possible if the remnant structure is maintained throughout the reduction and oxidation processes. In the case of spinel and transition alumina, specifically the γ-alumina polymorph, the close-packed oxygen sublattice is inherited from the parent spinel phase, providing a blueprint to reconstruct the parent phase upon oxidation. It has been shown that for Ni-based catalysts modified with $ZrO_2$ that the reduction-oxidation process is completely reversible for temperatures below 1000°C in oxygen environments.[65] Under these conditions, the γ → α-alumina transition is suppressed so that the spinel structure can form again. It was also found that the overall microstructure remains intact, indicating that the phase assemblages also follow suit. It must be noted that the intermediate oxidation step of Ni to NiO is deemed necessary to recover the spinel from the defective remnant spinel at higher temperatures.[62, 95]

Regeneration of Ni supported on various alumina and aluminate polymorphs as well as reduced $NiAl_2O_4$ have been shown to remove both carbon and sulfur contaminants via oxidative regeneration.[65, 95-99] In most cases, the catalytic activity (if observed) shows decreases upon regeneration, likely to the loss of catalytic particles or only partial regeneration. However, there are a few reported cases in which the catalytic activity remains unchanged or even increases with regeneration. Hashemnejad and Parvari showed that for a $Ni/CaAl_2O_4$ catalyst a steam treatment showed a significant reduction in the size

of the Ni particles, with increased methane conversion and hydrogen yield to the deactivated samples but did not discuss the initial conversion and yield results.[96] Dega and Abatzoglou demonstrated that two regeneration pathways are possible for Ni catalysts derived from slag oxides which the oxidative treatment slightly increased the catalytic activity.[98] A Ni/$\alpha$-$Al_2O_3$ catalyst studied by Du et al. utilized the solid-state reaction between oxidation products to form spinel and subsequently reduced the ceramic to obtain a composite with superior particle dispersion as well as markedly improved catalytic activity.[99] Our group has previously investigated a Co-Ni-Mg spinel catalyst identical to the ones used in the present study, which was found to increase catalytic activity upon regeneration.[65] All of these examples hint at some type of support surface reconstruction as well as redistribution of the catalytic nanoparticles, which can be surmised as the maturation of the microstructure.

## K. Addition of Modifying Oxides

To hinder the decrease of the support surface area and promote regeneration, matrix modifying oxides have been used with moderate success. $ZrO_2$ is the most effective retardant of the γ to α-alumina phase transition. Although the exact mechanisms are unknown, the modifier is known to inhibit grain growth and (in the case of tetragonal and cubic $ZrO_2$) act as a fast ion conductor of oxygen to the structure, which may help in altering the phase field. Phase equilibria and the resulting microstructure of the NiO-$Al_2O_3$-$ZrO_2$ ternary system were first studied by Cheng, Chen, and Shen.[100-102] Üstündag et al. found that small additions of the modifier (not exceeding 2.5 wt. %) can prevent grain boundary cracking and inhibit spinel grain growth,[103] similar to $ZrO_2$ effects on $Al_2O_3$.[104, 105] This is also supported by Han et al. in which multiple Ni-$Al_2O_3$-$ZrO_2$ xerogel catalysts were synthesized, varying the Zr/Al ratio, finding that the support surface area, NiO – support interaction, and acidity (reducing catalytically active sites) are inversely proportional to the Zr/Al ratio and that a Zr/Al = 0.2 has the best ethanol reforming performance.[106] In a recent study by Zhan and coworkers, it was determined that low calcination temperatures (≈800°C) form γ-$(Al, Zr)_2O_3$, a Zr substituted defective spinel,[107] as $\gamma$-$Al_2O_3$ can accommodate 17 wt.% $ZrO_2$ and $\theta$-$Al_2O_3$ can dissolve 42 wt. % $ZrO_2$.[108] The authors, however, assume the formation of γ-$(Al, Zr)_2O_3$ as an X-ray amorphous phase,

by analysis of the poor signal to noise XRD patterns. In another work by Djuricic et al., Zr-doped $Al_2O_3$ was synthesized by an aqueous salt solution precipitation method, where XRD traced the phase composition from $\gamma$- to $\alpha$-$Al_2O_3$, in which $ZrO_2$ particles were only found within the alumina matrix at 1200°C.[109] This result suggests that Zr is incorporated into the $\gamma$-$Al_2O_3$ structure creating Al-O-Zr bonds which require additional energy to phase separate and diffuse to create $ZrO_2$ and α-alumina at elevated temperatures. A drawback of both studies is the inclusion of an unknown quantity of defects resulting from low-temperature calcination of solution-based precursors for both $ZrO_2$ and $Al_2O_3$, presumably allowing for enhanced diffusion of Zr throughout the matrix.

Interestingly, $HfO_2$ has not been investigated with spinel catalysts despite its nearly identical properties to $ZrO_2$. However, the use of small Hf additions in thermal barrier coating and high-temperature alloy applications drastically affects the oxidation kinetics.[110-112] Recently, the Chen and Harmer group from Lehigh University investigated Hf doping in bulk $Al_2O_3$, and found that Hf preferentially segregates to the grain boundary, slowing the oxygen transport kinetics by a factor of 3-8 depending on concentration.[113, 114] Reduced grain boundary mobility at similar temperatures is observed in Zr doped $Al_2O_3$ as compared to the undoped $Al_2O_3$ samples,[115] which implies that similar mechanisms are at play with Hf and Zr in alumina-based oxides.

Other modifying oxides such as $Nb_2O_5$,[64, 116] $CeO_2$,[117-123] other transition metals,[46] and rare earth oxides[124] have been investigated within the literature, mostly focusing on the catalytic activity of the modified spinel. Zhang, Üstündag, and Sass evaluated $NiAl_2O_4$ with multiple transition metal oxides, and found little dependence on the reduction kinetics except in the case of $TiO_2$ addition.[46] B.E. Hill in his thesis corroborates that $TiO_2$ additions have adverse effects, expediting the $\gamma$- to $\alpha$-$Al_2O_3$ transition while $Nb_2O_5$ has similar effects to $ZrO_2$ during reduction, however does not provide any mechanistic reasoning.[72]

## L. Catalyst Microstructure and Ni Crystallite Shape

Catalyst microstructure is indicative of particle/grain size, composition, and reduction temperature. Small grains and particles yield more expedient metal reduction than larger grains due to shorter diffusion distances, enhanced grain boundary, and defect

diffusion, as well as more defective sites for nucleation to occur. At high synthesis temperatures (≥1500°C), $NiAl_2O_4$ and analogous chemistries exhibit highly faceted and stepped surfaces, providing highly faceted supports for catalysis.

Nickel crystallizes in an FCC structure (space group 225), with low index planes of (111) and (100) family as the most energetically favorable due to surface energy minimization.[125-127] Simulations to determine the energetically favorable low index planes consist of using some variation of the Embedded Atom Model (EAM); however, the Meltzman et. al study is of experimental significance. In this investigation, the wetting conditions of Ni metal were observed on sapphire at high temperatures (1300 and 1350°C) under $H_2$. Using a Wulff shape simulation that depends on the Gibbs thermodynamic principle, Meltzman et al. were able to identify low index (111) and (100) family shapes consistent with the previous EAM simulations.[127] Temperature and $p_{O_2}$ also have effects on the reduction of the catalyst, specifically on Ni particle size, location, and number density. Temperature and number density are inversely proportional while size is proportional to the temperature, which suggests an Ostwald ripening or surface diffusion mechanism (particle migration and coalescence). Particles are typically ordered on the support along faceted edges; however, no explanation on mechanisms or metal particle registry is provided within the literature.

Extracting metal (Ni) from the spinel via $H_2$ reduction creates small crystallites decorating the resulting defective spinel. Shapes of the crystallites have direct effects on the catalytic activity and turnover frequency (TOF) of the ensemble. TOF is defined as revolutions of the catalytic cycle per unit time, typically seconds.[128] Generally speaking, the tip of a crystallite is the most catalytically active, followed by the facet edges and then by the flat crystal planes. It has been shown for Ni and Ni-Co supported on defective spinel that at 850°C, a TOF of approximately $4.0s^{-1}$ is obtained for the methane reforming reaction.[65] Pompeo et al. has conversely shown for a Ni-Pt α-alumina supported catalyst reacted at 550°C a TOF ranging from 1.7 to $3.7s^{-1}$ is obtained, while Pt catalysts supported on $\alpha$-$Al_2O_3$ and $ZrO_2$ exhibit TOFs $<2s^{-1}$.[77] These results demonstrate that Ni additions to traditional Pt catalysts (or just Ni as the catalyst) as well as supporting on a defective γ-alumina structure increase the catalytic activity notably.

Previous work from the Misture group shows that for stoichiometric and Mg (and/or Co) substituted $NiAl_2O_4$ + 2.5wt.% $ZrO_2$ high TOFs can be obtained ($\approx 4.0 s^{-1}$), as well as resistance to sulfur poisoning.[65] It was also discovered using *in-situ* neutron diffraction under 4%$H_2$ that the oxygen sublattice is maintained at full oxygen occupancy throughout the reduction at 900°C, indicating that oxygen vacancies diffuse to the surface while the Al is redistributed throughout the spinel. The increased resistance to sulfur is attributed to Co additions to the spinel and the sintering temperature for the exsolved nanoparticles which provide highly faceted edges facilitating fast oxygen diffusion. Support faceting was also thought to increase oxygen diffusion, as terminations on the support can accommodate oxygen vacancies, up to 40% for $MgAl_2O_4$,[129] and provide additional oxygen for the removal of sulfur and other contaminants.

## M. *In-situ* Microscopy on Catalysts

Investigations of the catalyst surface are rare, as many studies typically focus on bulk properties and ignore surface and microstructural effects. Recently, *in-situ* environmental TEM (ETEM) investigations have been performed on a host of catalyst materials, spearheaded by the Hansen and Crozier groups. These studies utilize controlled atmosphere and temperature in conjunction with aberration-corrected TEM to probe catalysts at the nanoscale under relevant operating conditions.[86] A review previous to their work can be found in Ref.84, as the technique became more commonplace at this time.

One major drawback of ETEM is the necessity for high voltage electrons as well as large dose rates required for imaging, in which many samples are beam sensitive. Although SEM cannot replicate the dynamic pressure capabilities of the TEM, it can alleviate the need for high dose rate imaging, by the use of low voltage.

$Ni/SiO_2$ catalysts were initially studied by ETEM, where $CH_4$ and $O_2$ were used to simulate reactor conditions. It was found that Ni particles transform to void like NiO particles due to a Kirkendall-like effect aided by accelerated surface diffusion.[130] Upon reduction of this system, the Ni was found to diffuse along grain boundaries of the NiO, resulting in surface NiO at intermediate stages of the reduction.[87] Sintering of catalytic Ni supported on $MgAl_2O_4$ catalysts was conducted by DeLaRiva et al., where a combination of *in-situ* ETEM, Monte Carlo simulations, and models were used to describe catalyst

sintering.[84] These authors further differentiate the mechanisms based on their observations into three distinct regions, where Ostwald Ripening occurs in all regions, and particle migration and coalescence occurs in the latter two regions as time is increased.[84, 85] Recently, $TiO_2$ support faceting was found to drastically affect the sintering mechanisms of distributed Au nanoparticles, where some surfaces do not exhibit any sintering.[131] In another study, Pt-Pd alloyed particles supported on $\gamma$-$Al_2O_3$ were observed to have enhanced mobility *in-situ* at 850°C.[132] Mobility accelerated as the support transitioned to higher alumina polymorphs at ≥1000°C. Both the Au/$TiO_2$ system and Pt-Pd/$\gamma$-$Al_2O_3$ system hint that particle-support interactions can have drastic effects on the transport, which will inevitably affect the catalytic activity.

# II. EXPERIMENTAL PROCEDURE

## A. Spinel Synthesis and Reduction

Samples were prepared by a modified wet impregnation procedure as described in previous works.[62, 64, 65] Aluminate spinel (A-site cation = Ni, Co, Mg and mixtures thereof) with 2.5 wt. % modifying oxide (modifying oxide = $ZrO_2$, $HfO_2$, $NiNb_2O_6$, $Nb_2O_5$ and $CeO_2$) were synthesized from appropriate mixtures of NiO (97%, Arcos Organics), $Mg(OH)_2$ (99%, Fisher Scientific), $Co_3O_4$ (99%, Alfa Aesar), $\alpha$-$Al_2O_3$ (99%, Fisher Scientific), $ZrO(NO_3)_2 \cdot 6H_2O$ (99%, Aldrich Chemistry), $HfCl_4$ (99.9% Alfa Aesar), $NbCl_5$ (99% Alfa Aesar), and $Ce(NO_3)_3 \cdot 6H_2O$ (99% Alfa Aesar). Nitrate and chloride precursors were stored in an inert glove box to prevent hydration and further degradation. Undoped, $ZrO_2$, and $HfO_2$ containing samples were milled with $Al_2O_3$ media in a McCrone Micronizing mill (McCrone Group, Westmont, IL) in deionized water for 30 minutes, and subsequently dried. The resulting powder was then calcined in an alumina crucible at 1500°C for 8 hours, with a heating and cooling rate of 5 K/min in air. The resulting spinel was then ground to a fine powder in an alumina mortar and pestle, then passed through a 297μm sieve (U.S. number 50). Correct phases were confirmed by X-ray diffraction. Small amounts of residual NiO were present, approximately 0.5 wt. % determined by XRD.[62]

$Nb_2O_5$ and $CeO_2$ containing spinel samples were prepared by a wash coating method, where the spinel was synthesized using the previous procedure without any modifying oxide additions. $Nb_2O_5$ and $NiNb_2O_6$ sols were prepared by sonication of appropriate amounts of $NbCl_5$ in an 80:20 ratio of ethanol to DI water for 30 min. After sonication, calcined spinel was added to the solution so that the total niobium oxide content reached 2.5 wt.%, which aged for 24 hours. $Nb_2O_5$ and $NiNb_2O_6$ modified spinel were calcined for 8 hours in air at 600 and 1000°C, respectively. $CeO_2$ modified spinel was prepared by sonication of $Ce(NO_3)_3 \cdot 6H_2O$ with water until dispersed, then addition of calcined spinel so that the total ceria content would reach 2.5 wt.%. $CeO_2$ wash coated samples were calcined at 600°C in air to produce the modified spinel composites.

Spinel reductions consisted of a charge of 3.30 ± 0.001g calcined spinel in an alumina crucible placed under an S-type thermocouple in a sealed tube furnace. The tube

was then evacuated to 0.1 Torr and heated to the target reduction temperature at a rate of 3 K/min. Once the desired temperature was achieved, the furnace was backfilled with 40±0.4 kPa of ultra-pure $H_2$, measured by a capacitance manometer. Reduction temperatures and times were conducted in a previous study using *in-situ* HTXRD in $N_2$-4%$H_2$ reducing atmosphere until the Ni reflections ceased increasing.[62] Atmosphere was maintained until the furnace reached room temperature at a rate of 3 K/min.

## B. Room Temperature X-Ray Diffraction

X-ray diffraction (XRD) was performed in Bragg-Brentano geometry on thick powder mounted samples. Patterns were collected on a Bruker D8 Advance using Cu K$\alpha$ radiation, a Ni K$\beta$ filter, 2.5° Soller slit, 30 RPM sample rotation, and a LynxEye detector over the range of 20-80° 2$\theta$ with a step size of 0.02 °2$\theta$ and a count time per step of 1.0s.

All phase identification for XRD patterns was conducted in Bruker-AXS EVA (v. 5.1) in conjunction with the ICDD PDF4+ 2019-2020 databases. Rietveld refinements utilized TOPAS (v. 6) for whole pattern fitting.

## C. *In-situ* High Temperature X-ray Diffraction

*In-situ* high temperature X-ray diffraction (HTXRD) was performed in a custom Bruker D8 Advance equipped with an Anton Paar HTK 1200 XRD furnace using Cu K$\alpha$ radiation. In addition, a custom Siemens D5000 equipped with a large volume atmosphere-controlled furnace and Cu K$\alpha$ radiation was also used for samples where background fluorescence masked crucial peaks.[133] Oxygen concentration effects on reduction/oxidation cycles were investigated by atmosphere control. Dry air was introduced at a flow rate of 150 mL/min for oxidizing conditions. Industrial grade $N_2$ (5-20 ppm $p_{O_2}$, 1 atm reference) blanket gas simulated low oxygen conditions. $N_2$-4%$H_2$ forming gas mixtures were used as reduction atmospheres. $N_2$ and $N_2$-4%$H_2$ flow rates were fixed at 20 mL/min, with at least 30 minutes of equilibration time before measurement.

Patterns in air flowed at 150 mL/min and $N_2$ flowed at 20 mL/min were collected under identical conditions consisting of 25-105° 2$\theta$ at a scan rate of 0.5° 2$\theta$/s. Patterns were collected at room temperature, then from 400-1100°C in 100 K increments and then

finally again at RT. Ramping rates were fixed at 0.5 K/s, with dwells of 1 hour before measurement for equilibration, shown in Figure 3A.

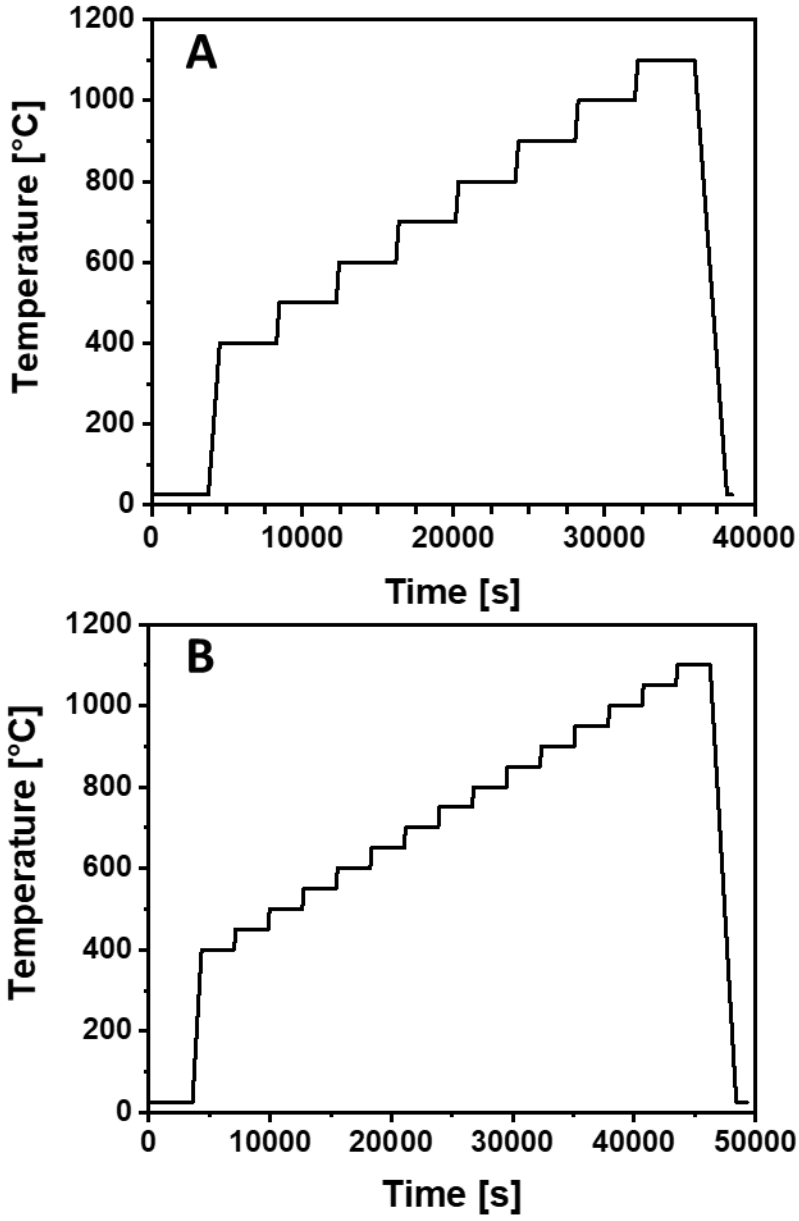


**Figure 3: HTXRD time vs. temperature profiles for A) Air and $N_2$ and B) 4%$H_2$-$N_2$ experiments.**

Patterns collected under reducing conditions in $N_2$-4%$H_2$ consisted of scans from 15-80° 2$\theta$ with a step size of 0.022° 2$\theta$ and a count time of 0.3 s/step, resulting in 15 minutes per pattern. A flow rate of 20 mL/min was used, with 45-minute dwells before

each measurement. Patterns were collected at room temperature, then from 400-1100°C in 50°C increments at a ramp rate of 0.5 K/s, then again at room temperature (Figure 3B).

Reduction/oxidation cycling was performed on the $Ni_{0.375}Co_{0.375}Mg_{0.25}Al_2O_4$ + 2.5 wt.% $ZrO_2$ sample *in-situ* using a modified version of the regeneration profile used in a previous work.[65] Patterns were collected from 10 to 65° 2$\theta$ with a step size of 0.03° 2$\theta$ and count time of 0.4 s/step. Samples were heated at a rate of 5.0 K/s to 900°C, where an equilibration time of ≈50 min was used before the 10 min measurement. Measurements were taken each hour in the same fashion for 12h during the reduction cycle and 20h during the oxidation cycle. The furnace was allowed to cool to room temperature at the same rate between cycles to extract samples for SEM analysis. The time vs. temperature profile for the redox cycling is shown in Figure 4.

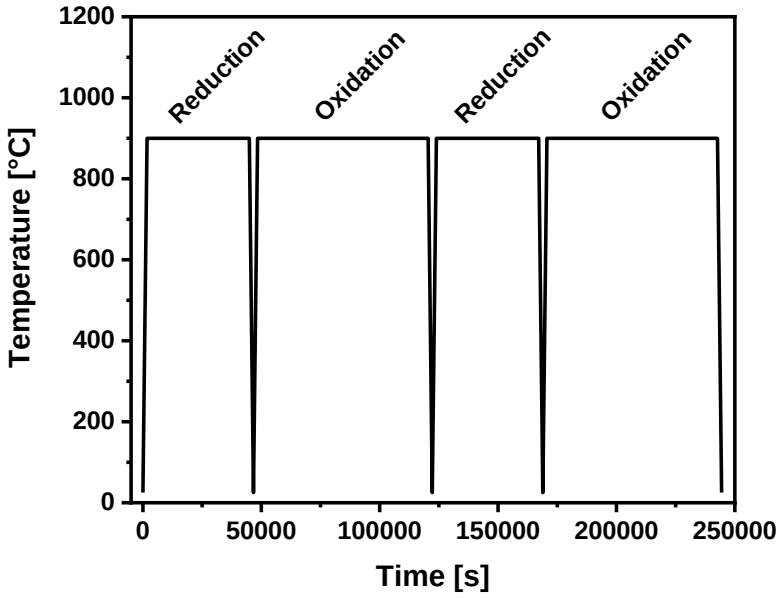


**Figure 4: HTXRD time vs. temperature profile for redox cycling. Reduction and oxidation regimes are labeled.**

## D. Scanning Electron Microscopy

Scanning electron microscopy (SEM) was conducted in a JEOL JSM 7800-F (JEOL, Tokyo, Japan) field emission electron microscope. Beam deceleration allowed for samples to be imaged at voltages at or below 2.0 keV without surface modification. Loose

powders were imaged on a carbon planchet, prepared by typical alcohol suspension loading procedures. No coating was necessary for low voltage imaging.

### E. High Temperature Scanning Electron Microscopy

High temperature scanning electron microscopy (HTSEM) was conducted within the JEOL JSM 7800-F equipped with an Aduro hot stage system (Protochips, Raleigh, NC) at 2 keV. The Protochips stage, controlled by an external computer running Aduro 200 (V2.2.4) software, was connected to a Keithley Model 2611B power supply (Tektronix, Beaverton, OR) via a pass-through port on the SEM chamber door. Heat is delivered to the sample by means of a semiconductor device (E-chip) which has a carbon film that dually acts as both heating element and support. The active area upon the chip consists of a 7x7 grid of 5.5 µm holes spaced such that they cover an area 100x100 µm in size. To obtain accurate temperatures (within ±10°C), only the center 3x3 grid of holes is used. Each chip is factory calibrated to apply the correct voltage to obtain accurate temperatures. The small heating element enables manufacturer quoted heating rates of up to 1000 K/ms to a maximum temperature of 1200°C within this central area of approximately 40x40 µm. Providing heat over the small element makes it possible to image the sample *in-situ* at elevated temperatures without specialized detectors; thus, standard high sensitivity detectors may be used during high temperature imaging with minimal risk of damage to the electronics. Furthermore, the E-chip offers good thermal stability and manageable beam drift during imaging.

Sample loading of the E-chip consisted of creating an ethanol-spinel suspension, which was then deposited upon the chip by transferring a drop on the tip of a set of precision tweezers (of the kind commonly used in TEM) and subsequently drying the specimen. Particle dispersions on the heating grid were checked by optical microscopy before loading the sample into the sample holder. External testing of the electrical connections between the chip and the sample holder was performed using a testing apparatus provided by Protochips. Failure of the connections test elicited repositioning of the chip on the sample holder. Upon passing the required resistance for the test voltage, the holder was placed in

the SEM, evacuated, and a temperature calibration file (provided for each individual chip by Protochips) was loaded for analysis.

Screen video captures were taken for the duration of heating for all HTSEM experiments to have the option of extracting individual frames. Open source video software provided by CamStudio (V. 2.7.2) was used for recording, later replaced by OBS Studio (V. 23.2.1). A Python (V 2.7.8, Anaconda Distribution V 2.3.0, Spyder 2.3.4 GUI) module, moviePy (V 0.2), was used to compile and edit the raw data into a video synchronized with the time and temperature recorded by the Protochips software. Video editing was done in such a way to compress the time scale of the video from an hour to a few minutes.

As each experiment has a unique set of collection challenges (i.e. focus, astigmatisms, thermal drift corrections, etc.), no specific time vs. temperature profile was followed. A typical time vs. temperature profile is shown in Figure 5, where all described experiments resembled similar profiles.

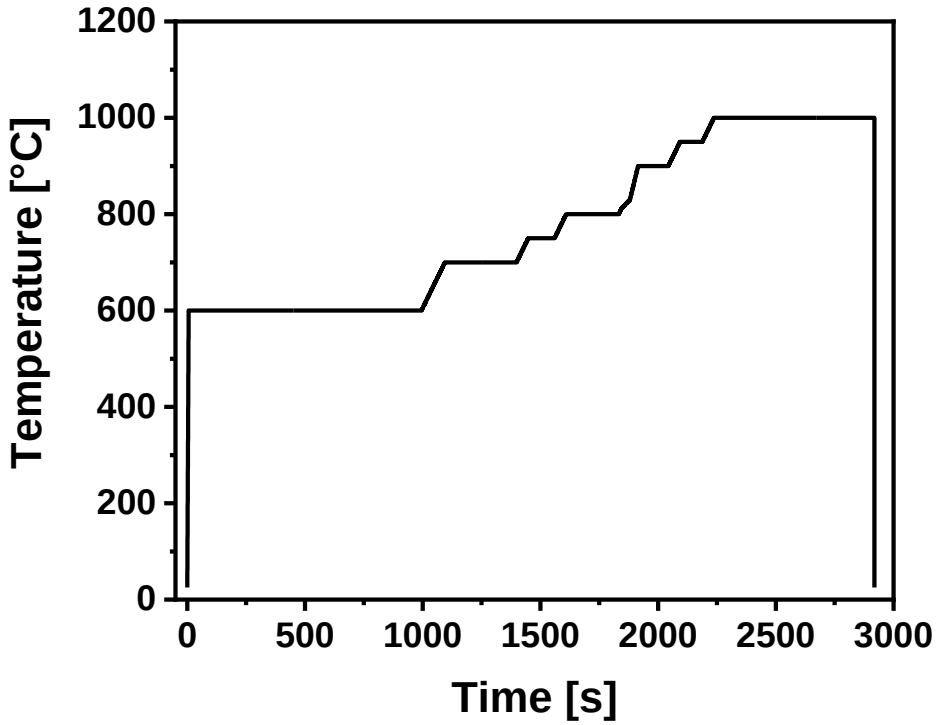


**Figure 5: Typical time vs. temperature profile for all HTSEM experiments, where the maximum temperature varies between 900-1200°C.**

## F. Raman Spectroscopy

Unpolarized Raman spectroscopy was performed with a WITec Alpha 300 RA (WITec GmbH, Germany) equipped with a variable power 488 nm laser and a Zeiss EC Epiplan 20x objective. Laser power varied between 5-15 mW due to sample fluorescence and laser spot size. Spectra were collected by averaging 150 measurements, each with 2s integration time. Cosmic ray removal and general processing of the spectra was conducted with Project FIVE+ software (Version 5.0, Build 5.0.3.43, WITec GmbH, Germany). Lorentzian peak profiles and a constant background term were used to model the Raman spectra, optimized by the software package, Fityk.[134] Estimated standard deviation of the peak positions is approximately 1 $cm^{-1}$.

## G. Transmission Electron Microscopy

### 1. Sample Preparation – Focused Ion Beam Milling

Focused Ion Beam (FIB) milled samples were prepared using a Thermo Fisher Helios G4 UX (Thermo Fisher, Waltham, MA) equipped with $Ga^+$ ion source at Cornell Center for Materials Research (CCMR) at Cornell University. Pt precursor gas was utilized to deposit a protective layer on the desired particle for surface retention under milling conditions. Lift-out samples were then welded to a nanomanipulator using the Pt precursor gas, removed from the milled section, and attached to an Omniprobe Cu FIB lift-out TEM grid on the protected "B" post.

### 2. Scanning Transmission Electron Microscopy

Scanning Transmission Electron Microscopy (STEM) was conducted on ion milled samples with a NION UltraSTEM 100 (NION, Kirkland, WA) at CCMR. In column spherical aberration corrections consisted of software optimization of multiple quadrupoles and octupoles, allowing for atomic level resolution. Accelerating potentials of 100 keV were used to image as well as EELS analysis (see below).

### 3. Electron Energy Loss Spectroscopy

Electron Energy Loss Spectroscopy (EELS) was performed on the aforementioned NION UltraSTEM 100 by means of a Gatan EELS spectrometer. Raw spectra were corrected for shifts around the zero-loss peak. Exposure time varied per element for single

spectra – Ni and O: 0.1 s exposure for 10 times resulting in a 1 s total spectra collection time; Zr: 2.0 s exposure time for 10 times resulting in 20 s total collection time per spectra. Map collection varied from 2-4 s per spectra for Ni and O over a total area of ≈15,000 $nm^2$ across the $ZrO_2$-spinel interface. Detector resolution was fixed for all conditions at 0.5 eV per channel. It is of note that to obtain sufficient Zr signal, 20 times the amount of time was needed, therefore it was not feasible to map Zr. Data analysis of the spectra was conducted in Gatan Digital Micrograph (V. 3.32.2403.0). Ni *L*-edge relative intensities were extracted by background subtraction of 240.0 eV pre-edge, with the signal region starting at 850.0 eV and ending at 960.0 eV. O *K*-edge relative intensity was analyzed in the same fashion, with a pre-edge background region of 28.0 eV and a signal region from 530 to 585 eV. Backgrounds were modeled by a typical power law.

# III. RESULTS AND DISCUSSION

## A. Evidence of Enhanced Transport on $NiAl_2O_4$ + 2.5 wt.% $ZrO_2$

Enhanced surface transport on reduced $NiAl_2O_4$ + 2.5 wt. % $ZrO_2$ has been observed previously in our group, where the reduced Ni particles on the surface migrate, coalesce, and resorb into the spinel via oxidative regeneration.[135] In an effort to shed light on enhanced mass transport and its relation to improved properties during redox processes, the morphology and stability (inherently the ability to accommodate defects via non-stoichiometry) will be evaluated for $NiAl_2O_4$. These results will be presented in the light of markedly improved surface and mass transport in subsequent sections, in conjunction with additional data on the solid solution series, $Ni_xMg_{1-x}Al_2O_4$ (x = 0 to 1.0) under redox conditions.

Improved mass transport on spinel of the form $NiAl_2O_4$ + 2.5 wt. % $ZrO_2$ was observed to exhibit what can be described as a "tunneling" phenomenon, where a presumably inert $ZrO_2$ particle burrows or tunnels into the supporting spinel oxide at temperatures exceeding 1000 °C. Tunneling is not defined by gravity; $ZrO_2$ particles travel inward towards the center of the spinel particle regardless of position on the support. Figure 6 exhibits typical $ZrO_2$ tunneling observed within the HTSEM experiments.

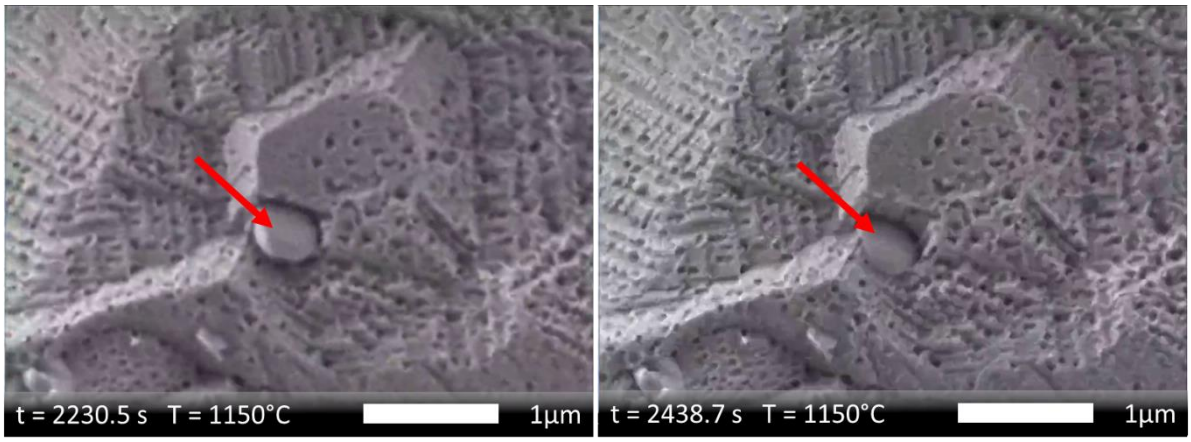


**Figure 6: $NiAl_2O_4$ + 2.5 wt.% $ZrO_2$ before (left) and after (right) tunneling observed *in-situ* at 1150 °C, $p_{O_2} \approx 2 \cdot 10^{-10}$ atm. $ZrO_2$ particles are marked with arrows.**

The subsequent sections are arranged to address the following questions regarding the tunneling phenomenon observed:

- Can other manifestations of enhanced mass transport be found under stable redox conditions for the spinel series?
- Does tunneling depend on systematic changes to the composition and consequently the structure and allowable defect content by the addition of Mg to the spinel?
- Does varying the modifier composition (i.e. $ZrO_2$ versus other oxides like $HfO_2$) affect the tunneling phenomenon?

## B. Compositional Variations – $Ni_xMg_{1-x}Al_2O_4$ + 2.5 wt. % $ZrO_2$

### 1. X-ray Diffraction

The substitution of Mg for Ni in the spinel results in marked changes to the overall structure, most notably the lessening of reducible species and subsequently the ability to have reduction induced point defects. Typical of solid solutions, one would expect the lattice parameter of the solid solution to obey Vegard's Law, however, slight deviations from linearity (observed in the x = 0.75 sample) arise from inherent variation in cation site occupancy as the spinel becomes more inverse.[23, 62, 72] XRD patterns for the series are shown in Figure 7, with Figure 8 depicting Vegard's Law as it pertains to the lattice parameter. Only pure spinel (x = 0, PDF# 04-014-4624; x = 1, PDF# 04-005-6872) was identified as the major phase, with small amounts of $ZrO_2$, crystallizing in monoclinic (Baddeleyite or m-$ZrO_2$) (PDF# 04-004-4339) and tetragonal (t-$ZrO_2$) (PDF# 04-005-4207) forms.

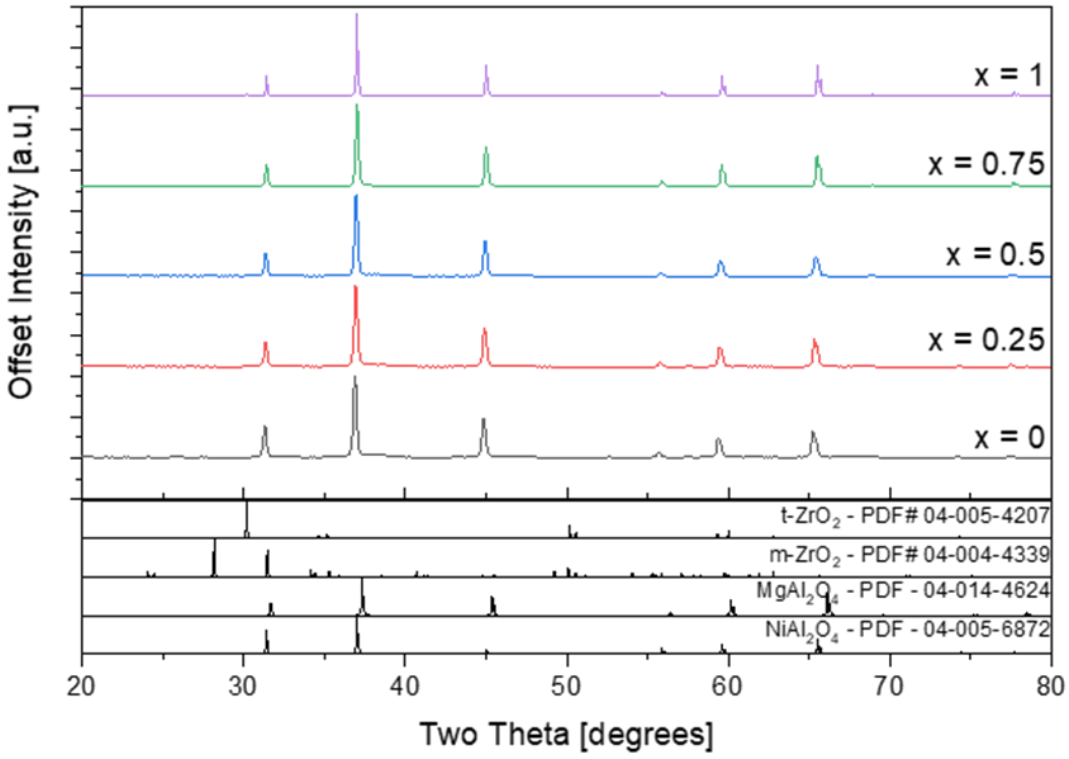


**Figure 7: XRD patterns of the solid solution series $Ni_xMg_{1-x}Al_2O_4$ from x = 0.0 to 1.0. PDF patterns are provided for each component present.**

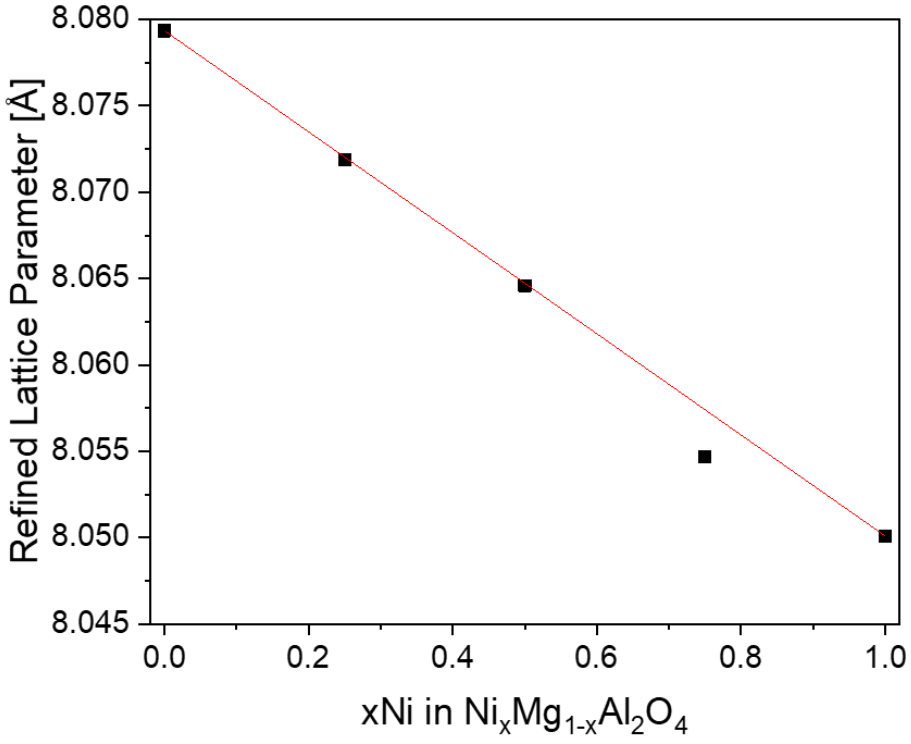


**Figure 8: Vegard's Law applied to the lattice parameter of the solid solution $Ni_xMg_{1-x}Al_2O_4$. The linear trace represents ideal behavior. Error bars are within plotted points.**

To assess the dual $ZrO_2$ phases, the amount of $ZrO_2$ (2.5, 10.0, and 20.0 wt. %) increased during the batching process and the calcined products were evaluated with Rietveld analysis (Figure 9). The amount of stabilized t-$ZrO_2$ remained constant while the m-$ZrO_2$ total wt. % increased, indicating that calcination can only stabilize a finite amount of t-$ZrO_2$. Tetragonal to monoclinic ratios varied dramatically, 0.94, 0.16, and 0.05 for 2.5, 10.0, and 20.0 wt. %, respectively. The spinel lattice parameter remained invariant with the amount of $ZrO_2$ added. Ni has been shown as well as other transition metals to stabilize tetragonal and even cubic $ZrO_2$ for a host of low temperature catalysis applications.[136-139] Direct evidence of the microstructural effects of $ZrO_2$, specifically the monoclinic and tetragonal phase, is presented by Shen et al. where confined $ZrO_2$ particles anisotropically strain the surrounding spinel matrix.[101, 102] Through rigorous TEM investigations by these authors, it was deduced that t-$ZrO_2$ caused the surrounding spinel to be under tensile stresses, while the m-$ZrO_2$ phase induced a compressive stress to the surrounding matrix. Üstündag et al. also found that small amounts of $ZrO_2$ (identical to the ones used in this study) inhibit $NiAl_2O_4$ grain growth,[103] which is supported by the more generalized grain boundary pinning found in $ZrO_2$ doped $Al_2O_3$.[140, 141] It can be concluded that in the system of interest with 2.5 wt. % $ZrO_2$ with about a 1:1 m:t ratio, that the spinel in contact with $ZrO_2$ may have local stress perturbations, in which mass diffusion along the boundary is facilitated to reduce the overall energy.

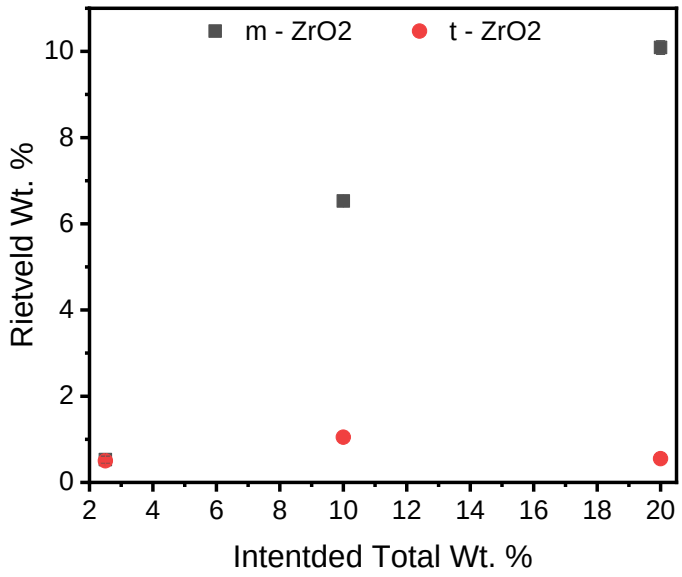


**Figure 9: Rietveld analysis of m-$ZrO_2$ and t-$ZrO_2$. Plotted error bars are smaller than the data points.**

## 2. High Temperature X-ray Diffraction

### a. Reduction Conditions – 4% $H_2/N_2$

Parent $NiAl_2O_4$ + 2.5 wt. % $ZrO_2$ was evaluated for stability under reducing conditions of 20 mL/min flowing 4% $H_2/N_2$ up to 1100 °C. Diffraction patterns starting at room temperature and increasing from 400 to 1100 °C appear in Figure 10. Trace amounts (0.71 wt.% by Rietveld) of Ni are first observed at 800 °C and increase as the measurement proceeds. Spinel, Ni metal (PDF# 04-013-4763), and the two low temperature polymorphs of $ZrO_2$ are present in the pattern until 1100 °C is reached. Ni metal dominates the diffraction pattern at the highest temperature with small reflections of the t- and m-$ZrO_2$ polymorphs, along with metastable spinel ($NiAl_{26}O_{40}$, PDF# 00-020-0776) and the appearance of θ-$Al_2O_3$ (PDF# 04-008-7261), shown in Figure 11.

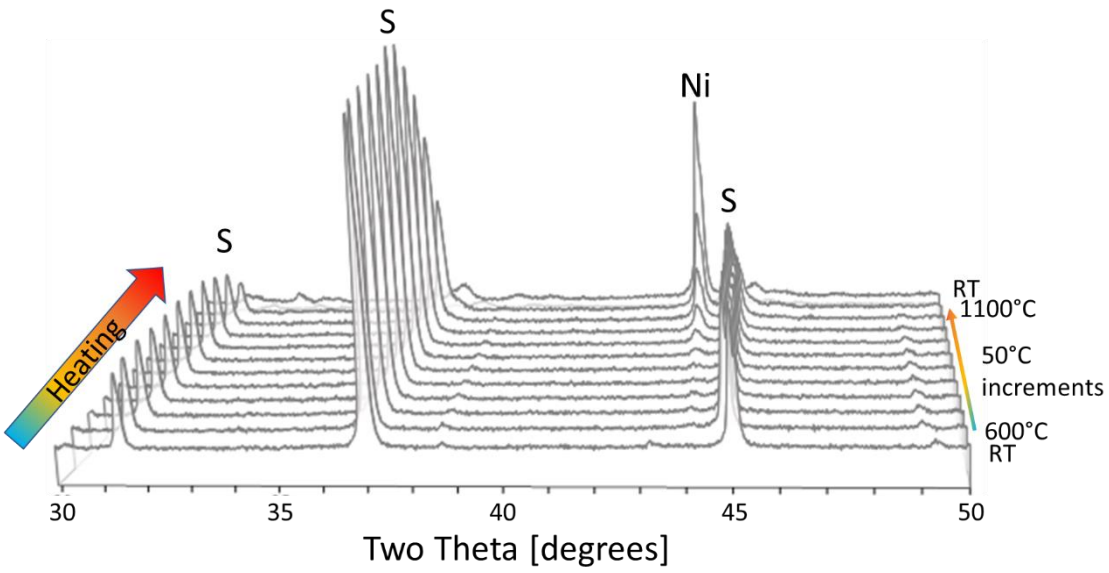


**Figure 10: HTXRD in 4% $H_2/N_2$ of $NiAl_2O_4$ + 2.5 wt. $ZrO_2$. S denotes spinel peaks, while Ni represents the Ni reflections.**

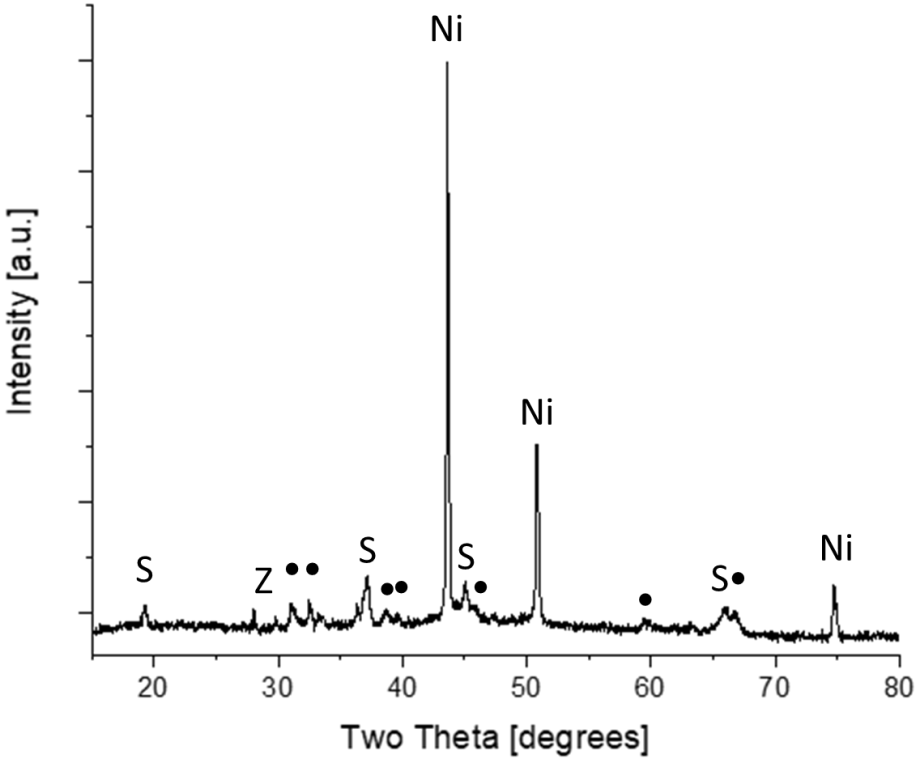


**Figure 11: 1100°C pattern of the HTXRD – $H_2$ experiment. Phases are labeled as S – spinel, Ni, Z – $ZrO_2$, and • – transition $Al_2O_3$/ metastable spinel.**

Extensions to the whole solid solution series $Ni_xMg_{1-x}Al_2O_4$ + 2.5 wt. % $ZrO_2$ were conducted previously to 1300 °C in 200 mL/min flowing 4% $H_2/N_2$ and are shown in Table III in terms of stability.[72] Stability is defined as the formation of the metastable spinel and/or $\gamma$-$Al_2O_3$, and the suppression of $\theta$-$Al_2O_3$ or corundum phases. The full Mg sample is naturally stable throughout the temperature range due to the lack of any reducible species under the experimental conditions. An interesting note is that the x = 0.75 sample is unstable at a lower temperature than the x = 1 sample which interrupts the expected trend. This unexpected discrepancy was discovered and thoroughly described elsewhere,[72] but mainly attributed to a shift in the reduction kinetics, associated with the $H_2$ dissociation pressure as well as the composition of the reaction layer and resulting changes in diffusional properties. It is also interesting to note that the entropy of free mixing for the x = 0.75 composition has been found to be lower than that of the x = 0.5 and x = 0.25 at 1000 °C, which may explain the hastened kinetic response.[142]

**Table III: HTXRD phase stability on solid solution $Ni_xMg_{1-x}Al_2O_4$ + 2.5 wt. % $ZrO_2$ (from Hill[72])**

| Temperature [°C] | x = 1 | x = 0.75 | x = 0.50 | x = 0.25 |
|---|---|---|---|---|
| 700 | Stable | Stable | Stable | Stable |
| 800 | Stable | Stable | Stable | Stable |
| 900 | Stable | Stable | Stable | Stable |
| 1000 | Stable | Unstable | Stable | Stable |
| 1100 | Unstable | Unstable | Stable | Stable |
| 1200 | Unstable | Unstable | Stable | Stable |
| 1300 | Unstable | Unstable | Stable | Stable |

It is worthwhile to consider the similarities in diffraction patterns between metastable spinel phases (for example, $NiAl_{10}O_{16}$ and $NiAl_{26}O_{40}$) and the transition alumina phases such as $\gamma$- and $\theta$-$Al_2O_3$, where differences are minute with multiple crucial overlapping features, making differentiation inherently difficult. Recall that $\gamma$-$Al_2O_3$ retains the CCP oxygen sublattice critical for regeneration of the parent spinel, whereas $\theta$-$Al_2O_3$ does not.[64] In addition, the lack of crystal perfection (and introduction of defects) in this system as denoted by the poorly defined broad Bragg reflections make phase identification even more problematic. It must be inferred that since the spinel phases

present are metastable, that the system is kinetically limited in the scope of the HTXRD experiment. Given enough time and temperature, a thermodynamically stable composite of Ni + $\alpha$-$Al_2O_3$ through increasing amounts of $\delta$- or $\theta$-$Al_2O_3$ will form rendering the sample non-regenerable as evidenced by the kinetic studies by Zheng et al.[46] It was found that given extended time, metastable spinel ($NiAl_{10}O_{16}$) transformed to Ni + $\theta$-$Al_2O_3$ after 24-48 h and to Ni + $\alpha$-$Al_2O_3$ after 144-168 h at 1100 °C and oxygen activity of $10^{-14.8}$. The same conclusion could be drawn if the system was allowed sufficient equilibration time under an air atmosphere, the observed metastable spinel will revert to the parent spinel phase. Therefore, the spinel is only rendered unstable by the loss of the CCP oxygen sublattice, i.e. the formation of any transition alumina, save $\gamma$-$Al_2O_3$. For the sake of these and findings presented subsequently, it must be understood that the HTXRD experiments were conducted in flowing 4% $H_2/N_2$ and that this is an extreme case in comparison to the HTSEM experiments presented later. Ergo, it is plausible to assume that since there are only trace amounts of transition alumina present under these extreme conditions, the nucleation of metastable spinel or transition alumina will not occur in the HTSEM experiments presented below, even at higher temperatures than experienced in the HTXRD.

**b. Oxidizing Conditions – Dry Air**

HTXRD in 150 mL/min of flowing air was conducted on previously reduced $NiAl_2O_4$ + 2.5 wt. % $ZrO_2$ at 900°C to evaluate the regeneration aspect of the redox cycle, shown in Figure 12. Phases characteristic of spinel, Ni metal, t- and m-$ZrO_2$ are seen in the initial patterns at room temperature. Structural alterations occur in the temperature range of 400-500°C where Ni is oxidizing to bunsenite (NiO, PDF# 00-047-1049), which is complete by 900°C. Stoichiometric parent spinel phase regeneration occurs above this temperature which is in agreement with previous studies,[62] indicated by the sharpening and intensity increase of the spinel reflections (Figure 12B). The improvement of spinel crystallinity translates to the elimination of point defects brought on by the reduction process. A minute amount of residual NiO is present at room temperature, presumably due to sluggish kinetics of the reforming reaction[99, 143] and the rate-limiting diffusion of cation vacancies in spinel systems in air.[30, 144, 145] In a simplification, if the kinetically limited reaction of NiO and defective spinel was given sufficient time to go to completion, the

HTXRD investigations suggest that the following equation (Equation (11)) can represent the bulk oxidation nature of the system for $NiAl_2O_4$:

$$Ni_{1-x}Al_2O_{4-x} + xNi + \frac{x}{2}O_2 \xrightarrow{O_2+heat} xNiO + Ni_{1-x}Al_2O_{4-x} \xrightarrow{time+heat} NiAl_2O_4 \qquad (11)$$

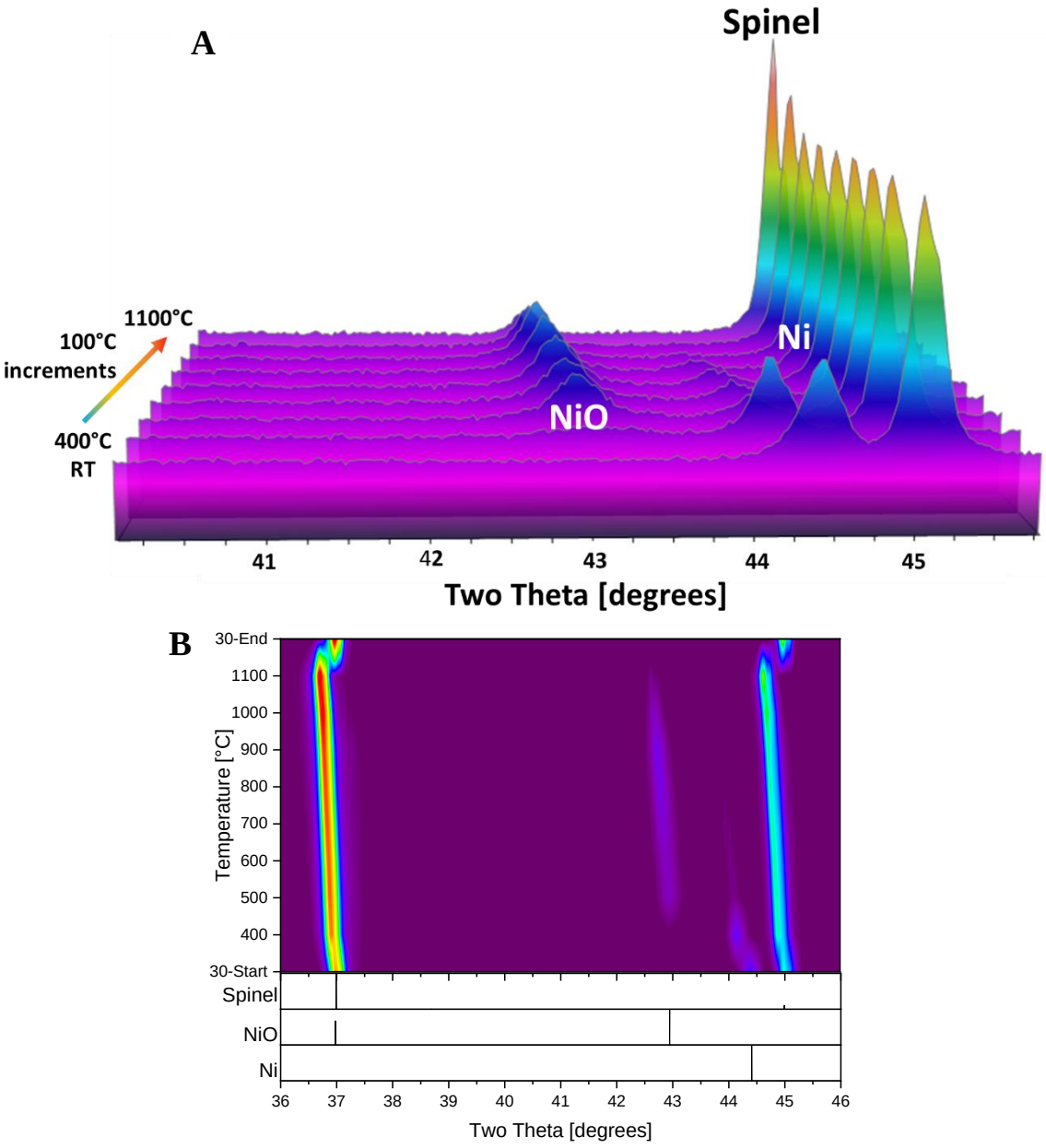


**Figure 12A: HTXRD patterns shown to 1100 °C of $NiAl_2O_4$ + 2.5 wt. % $ZrO_2$ in flowing air. Phases are labeled as spinel, Ni and NiO. B: Heat map of the patterns showing intensity and position evolution with temperature.**

With remnant NiO present in a quantity that is detectable by XRD, it can be assumed that some spinel remains non-stoichiometric and inherently defective. The NiO retains similar morphology to Ni as particles (see SEM section for an in-depth discussion on morphology), in which the NiO is concentrated such that a diffraction pattern can be collected. As for the defective spinel counterpart, if similar logic applies, defective spinel will retain the same morphological features. These features are, however, spread throughout the originally reduced area of the spinel particle, which is much larger than the islands of NiO.

### c. Neutral Conditions – $N_2$ with trace $p_{O_2}$

To evaluate bulk reactions at intermediate $p_{O_2}$, spinel of the form $NiAl_2O_4$ + 2.5 wt. % $ZrO_2$ previously reduced at 900 °C was exposed to 20 mL/min of industrial grade $N_2$ (5-20 ppm $O_2$, $\approx 10^{-5}$ atm. $p_{O_2}$) during *in-situ* HTXRD to 1100 °C with a temperature profile mirroring the experiment in the previous section. Patterns are shown in Figure 13. As expected, phase compositions paralleled the previous HTXRD experiment in dry air: spinel, Ni metal, t- and m-$ZrO_2$. All phases persisted through the maximum temperature of the experiment, with no observed phase transitions. No nucleation of $\theta$- or $\alpha$-$Al_2O_3$ occurred, indicating the stability of the initial phases present under neutral conditions. Absence of the strongest NiO reflection between 42.5-43.5° $2\theta$ also suggests no detectible oxidation occurs under these conditions.

Further investigation of the major spinel reflections reveal growth and sharpening of these features at 1000 °C and certainly at 1100 °C are indicative of structural relaxation at elevated temperatures, which prompted a Rietveld analysis on the Ni metal and spinel contributions to the pattern. The room temperature patterns before and after the HTXRD $N_2$ experiment as well as the refined wt.% of spinel and Ni up to 1100 °C are shown in Figure 14.

$ZrO_2$ phases were omitted from the Rietveld refinement analysis due to the elevated background at high temperature, masking the low intensity reflections of the phases, and causing overexaggerated fitting parameters of all phases included and unusually high RWPs.

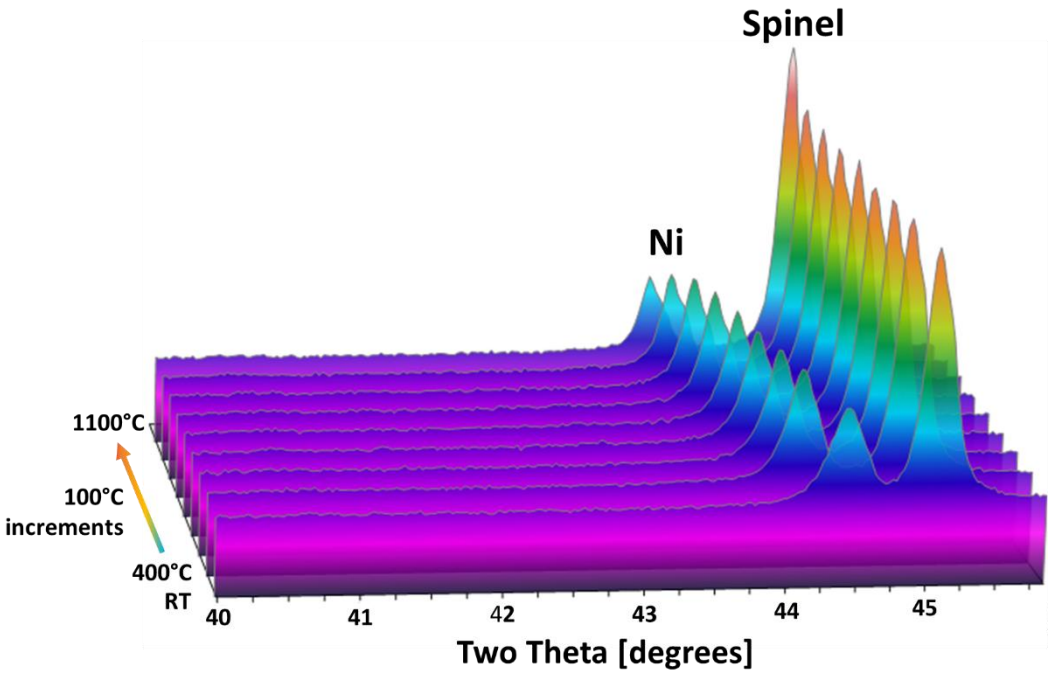


**Figure 13: HTXRD patterns of $NiAl_2O_4$ + 2.5 wt. % $ZrO_2$ in industrial grade $N_2$ with reflections marked for spinel and Ni metal.**

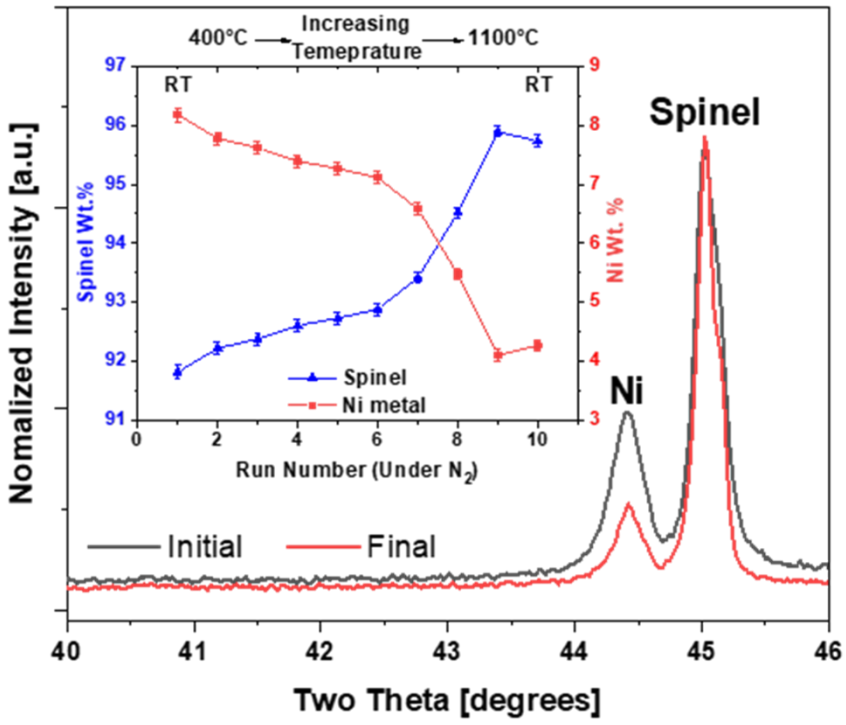


**Figure 14: XRD patterns of $NiAl_2O_4$ + 2.5 wt. % $ZrO_2$ before and after *in-situ* HTXRD in $N_2$ to 1100°C. Phases are labeled above the reflections. Inset: Rietveld refined weight percentages for Ni metal (red) and spinel (blue).**

Upon analysis, it was found that the refined spinel increased by ≈4 wt. % at the expense of the refined Ni wt. %. Microstrain of the spinel decreased markedly (Figure 15), especially at 1100°C for both air and $N_2$ experiments, indicating the loss of local perturbations (i.e. reduction induced volumetric strain) on the lattice. According to the Ellingham diagram, Ni oxidation is energetically favored at temperatures below ≈1500°C for both air and $N_2$ $p_{O_2}$ conditions. Taking into account Equation (11), it may be posited that the Ni is reacting with the trace amount of oxygen present, via either oxidation at the triple phase boundary or by oxidation in a Ni/NiO core-shell structure (both cases below the detectable limit), which immediately reacts with the remnant spinel. *In-situ* TEM evidence by Crozier and coworkers suggests that Ni/NiO core-shell structures form by a modified Kirkendall process in partial oxidation of methane reactions at 400°C.[83, 87] At higher temperatures, the rate at which NiO reacts with the defective spinel must be faster than the oxidation of Ni to NiO under these specific conditions, making the oxidation reaction rate limiting. Regardless of route, regeneration of the spinel phase is evident from Rietveld analysis.

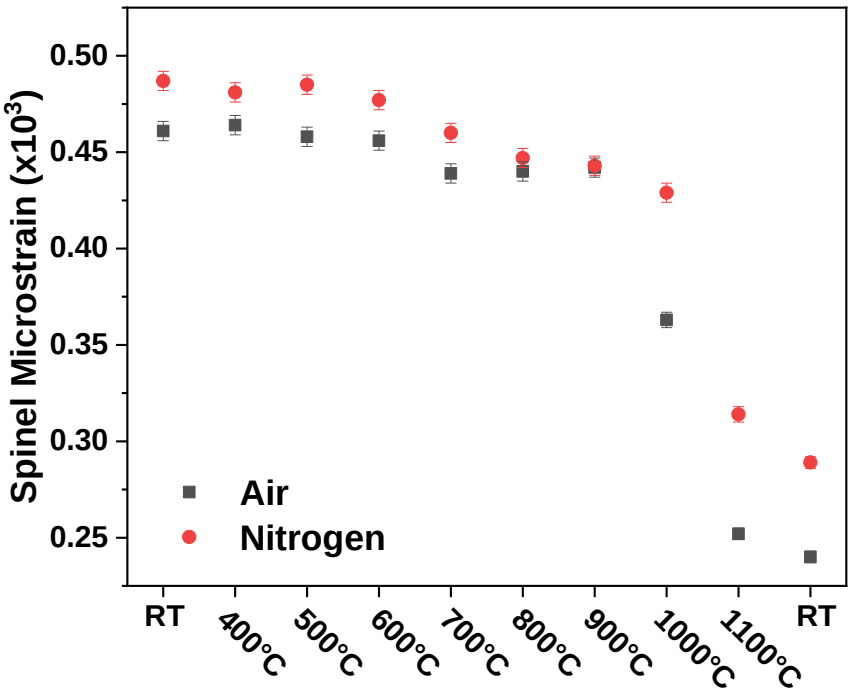


**Figure 15: Residual microstrain of reduced $NiAl_2O_4$ + 2.5 wt.% $ZrO_2$ reduced in air and $N_2$ derived from Rietveld analysis on *in-situ* HTXTD scans. Most error bars are smaller than their corresponding points.**

### 3. Raman Spectroscopy

Raman spectra of the parent solid solution (Figure 16) exhibit features consistent with typical band assignments of $NiAl_2O_4$[60] and $MgAl_2O_4$,[146, 147] where the Raman active modes are $A_{1g}$, $E_g$, and $T_{2g}$ for the $Fd\bar{3}m$ space group according to group theory.[148] Tabulated band positions are provided in Table IV, which are consistent with the literature values and assignments. Bands near 468 $cm^{-1}$ have an unassigned mode designation, due to absence of this band in single crystals but presence in polycrystalline samples.[60] All spectra exhibit an intense band between 360-410 $cm^{-1}$ ($E_g$) with weak side bands between 300 and 325 $cm^{-1}$ ($T_{2g}$). Close inspection of the strong $E_g$ band shows systematic decrease of position as Ni is substituted into the lattice, as well as noticeable broadening as soon as Ni is introduced. The low energy $T_{2g}$ band also shifts systematically, from being a separate peak in $MgAl_2O_4$ to a low energy shoulder in $NiAl_2O_4$. Spectral features between 550-650 ($T_{2g}$) and 650-850 $cm^{-1}$ ($A_{1g}$) are broadened, with multiple peak components contributing to the intensity. The m- and t-$ZrO_2$ contributions to the presented spectra have not been removed, and are represented by the dashed vertical lines in Figure 16. Not all spectra have contributions of $ZrO_2$, as the spatial arrangement is inconsistent throughout the microstructure. As some $ZrO_2$ spectral features are present between 600-650 $cm^{-1}$ for both polymorphs, the 550-650 $cm^{-1}$ region is not considered when comparing the solid-solution series. High wavenumber modes ranging from 650-850 $cm^{-1}$ have been attributed to metal oxygen bond deformation in tetrahedral and octahedral coordination, $M_t$-O bond and $M_o$-O respectively, resulting in complex multiplicity of the band for inverse II-III spinel.[60, 149-152]

The $E_g$ band broadens as Ni is introduced, likely due to localized regions of non-uniform cation disorder or local non-stoichiometry,[60] which is typical for inverse spinel as the octahedral positions are shared by $Ni^{2+}$ and $Al^{3+}$ cations. Furthermore, an argument can be made that the strongest band ($E_g$ mode at 360-410 $cm^{-1}$) can be solely attributed to the $M_o$-O bond vibration, which is noticeably different for inverse and normal spinel. On a crystallographic basis, differences in the lattice and oxygen parameter, *a* and *u* respectively, are associated with changes in tetrahedral and octahedral bond length. As the oxygen parameter is increased from ideality ($u = 0.25$), oxygen displace along [111], enlarging the tetrahedral site at the expense of the octahedral site.[27] From XRD data, the *u* value for

$NiAl_2O_4$ was refined to be 0.257 and 0.263 for $MgAl_2O_4$, which corresponds to a contraction of the average $M_o$-O bond by 0.03Å and an expansion of the $M_t$-O bond by 0.13Å as Mg replaces Ni in the spinel, based on the treatment of O'Neill and Navrotsky.[27] A smaller $M_o$-O bond will result in shifts to higher frequency with increasing Mg content, which is clearly observed in the data, whereas expansions will shift to lower frequency. This logic is supported by measurements on $MgAl_2O_4$ at high temperature which exhibit a shoulder feature on the low frequency side of the main $E_g$ band at elevated temperature as well as quenched samples, which has been attributed to the redistribution of $Al^{3+}$ cations from octahedral to tetrahedral sites.[146, 147, 153] This shoulder feature on the low frequency side is observed in the presented data for $MgAl_2O_4$, which matches the frequency of the main band as Ni is substituted into the lattice.

**Table IV: Fitted band positions for Raman spectra of as-prepared solid-solution series. $ZrO_2$ fitted bands have been omitted. * - denotes possible discrepancy with $ZrO_2$ Raman bands. X denotes unassigned bands.**

| | | **Mode Symmetry, $\nu$ [$cm^{-1}$]** | | | | | | | | | |
|---|---|---|---|---|---|---|---|---|---|---|---|
| **Sample** | **Ref** | **$E_g$** | **X** | **$T_{2g}$** | | | **$A_{1g}$** | | | | |
| $NiAl_2O_4$ | [60] | 370 | 468 | 323 | 564 | 600 | 686 | 720 | 766 | 800 | 830 |
| $NiAl_2O_4$ | This work | 367 | 452* | 315 | 553 | 602 | - | 717 | 763 | - | 825 |
| $Ni_{0.75}Mg_{0.25}Al_2O_4$ | This work | 370 | 473* | 315 | 567 | 607 | 681 | 719 | 777 | - | 832 |
| $Ni_{0.50}Mg_{0.50}Al_2O_4$ | This work | 377 | 471* | 310 | 568 | 609 | 682 | 720 | 755 | 787 | 831 |
| $Ni_{0.25}Mg_{0.75}Al_2O_4$ | This work | 388 | - | 305 | - | 600 | 680 | 721 | 756 | 789 | 829 |
| $MgAl_2O_4$ | This work | 404 | - | 303 | - | - | 663 | 719 | 763 | - | - |
| $MgAl_2O_4$ | [147] | 410 | - | 306 | - | - | 670 | 720 | 768 | - | - |

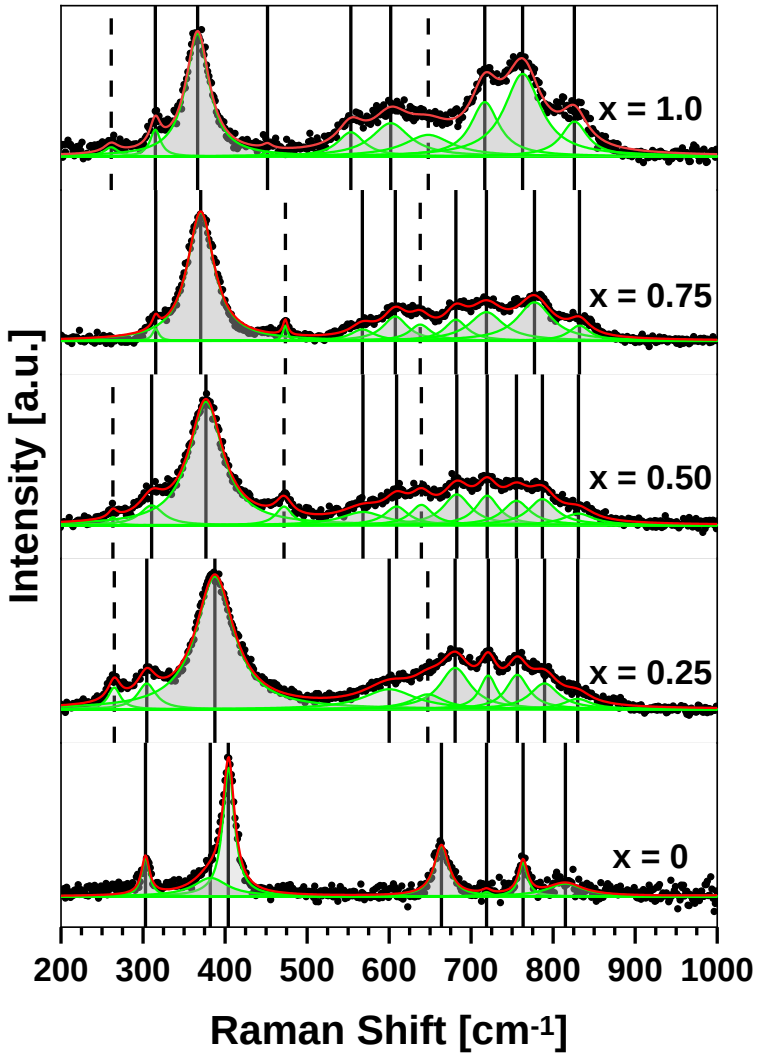


**Figure 16: Raman spectra of as prepared $Ni_xMg_{1-x}Al_2O_4$ + 2.5 wt. % $ZrO_2$ with varying x. Composite (red) and individual (green peaks) components for the fitted data. Dashed vertical lines represent band assignments for $ZrO_2$.**

Reduced spinel was also analyzed with Raman spectroscopy and is shown in Figure 17, with tabulated band positions in Table V. Spinel reduction temperature varies from composition to composition (see Table V) due to the amount of Raman inactive Ni on the surface, which diminishes the measurable spinel signal. Compositions were chosen by the amount of Ni removed, which ranged from 1.0 – 3.5 wt. % based on Rietveld analysis.[64]

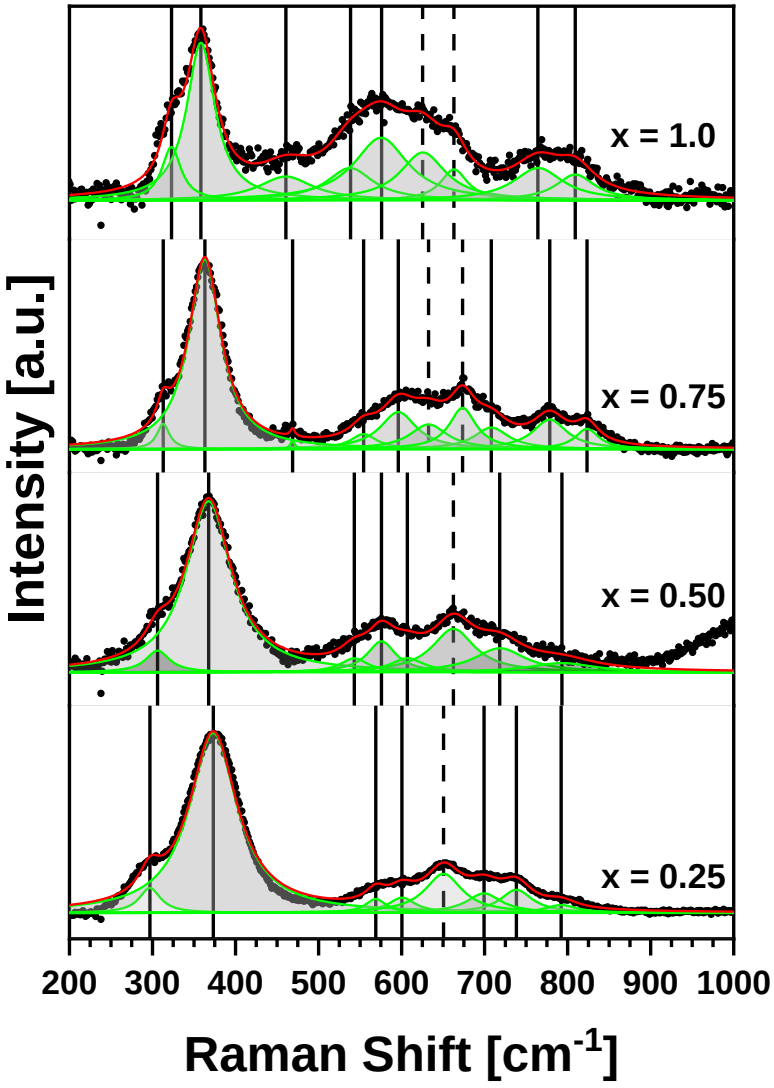


**Figure 17: Raman spectra of reduced $Ni_xMg_{1-x}Al_2O_4$ + 2.5 wt. % $ZrO_2$ with varying x. Compositions x = 0.25 and 0.50 are reduced at 900°C, while x = 0.75 and 1.0 are reduced at 900°C. Composite (red) and individual (green peaks) components for the fitted data. Dashed vertical lines represent band assignments for $ZrO_2$.**

**Table V: Fitted band positions for Raman spectra of reduced spinel solid-solution series. $ZrO_2$ fitted bands have been omitted. * - denotes possible discrepancy with $ZrO_2$ Raman bands. X denotes unassigned bands.**

| | | Mode Symmetry, $\nu$ [$cm^{-1}$] | | | | | | | | | |
|---|---|---|---|---|---|---|---|---|---|---|---|
| **Sample** | **$T_{red}$ [°C]** | **$E_g$** | **X** | **$T_{2g}$** | | | **$A_{1g}$** | | | | |
| $NiAl_2O_4$ | 750 | 358 | 461* | 323 | 576 | - | - | - | - | 764 | 809 |
| $Ni_{0.75}Mg_{0.25}Al_2O_4$ | 750 | 363 | 469* | 313 | 554 | 596 | 673 | 708 | - | 778 | 823 |
| $Ni_{0.50}Mg_{0.50}Al_2O_4$ | 900 | 368 | - | 306 | 576 | 607 | - | 718 | - | 793 | - |
| $Ni_{0.25}Mg_{0.75}Al_2O_4$ | 900 | 373 | - | 297 | 569 | 600 | - | 699 | 738 | 792 | - |

As discussed in the previous sections on diffraction, the phase composition of the reduced specimens consists of remnant spinel which is the major phase and analogous to the $\gamma$-$Al_2O_3$ structure. There is general disagreement within the literature on the Raman spectrum of pure $\gamma$-$Al_2O_3$, where $Al(OH)_3$ derived structures exhibit some Raman bands[154, 155] while other synthesis methods produce a fluorescence-like spectra with no discernable features.[156-158] Dyer et al. show that the hydration state of $\gamma$-$Al_2O_3$ is critical in determining the Raman spectrum, where a stable $Al(OH)_3$ layer is produced and provides the signal.[155] Liu et al. has demonstrated that for $\gamma$-$Al_2O_3$, a calculated spectrum resembling the spinel Raman fingerprint can be obtained through first principles calculations.[159] This result is logical, as $\gamma$-$Al_2O_3$ and the spinel share the same $Fd\bar{3}m$ space group, and therefore should have similar Raman responses, despite differences in the cations present. The samples described here are derived from stoichiometric spinel and will be treated as defective analogues rather than pure, well-crystalline $\gamma$-$Al_2O_3$.

While features generally resemble the parent spinel spectra, all bands exhibit broadening especially in the high frequency regions as cation inversion and local non-periodicity is introduced during the reduction process. Broadening of the $A_{1g}$ region is expected with the reduction and removal of Ni and redistribution of $Al^{3+}$ cations, as it is comprised of mixed octahedral and tetrahedral contributions. Ni resides mainly on the octahedral sites in inverse spinel, where it is logical to assume that upon reduction, a large amount of the extracted metal results in octahedral site defects. Furthermore, redistribution of the $Al^{3+}$ cations can occur to form the non-stoichiometric remnant spinel.[65] The $A_{1g}$ vibration perturbs three octahedral and one tetrahedral metal-oxygen bond,[60] and therefore the bands in this region are sensitive to cation vacancies as well as some redistribution of

$Al^{3+}$ from tetrahedral to octahedral coordination. $T_{2g}$ bands will be ignored due to the possible overlap with $ZrO_2$ polymorphs. Again, attention is paid to the major $E_g$ band, where shift to lower frequency is observed as more $Ni^{2+}$ is substituted onto the octahedral site in place of the $Al^{3+}$ for the reduced solid-solution series. This substitution causes changes in the oxygen positional parameter from 0.257 to 0.261 as Mg is substituted into the spinel for reduced samples[64] and consequently the average octahedral bond distance, shifting the band to lower energies as Ni content is increased. It is of note that the previous statement is only valid if the reduced amounts of Ni are comparable, as octahedral occupancy is inclined to change as $Ni^{2+}$ is removed, vacancies are created, and $Al^{3+}$ is redistributed during the reduction causing band broadening as well as shifts.

The position of the main $E_g$ band of the Raman spectra exhibits a negative deviation from linearity for the as-prepared series if compositions $0.25 \geq x \geq 1.0$ are considered (Figure 18). Gil-Calvo et al. have also discovered a similar trend by decreasing the Ni/Al ratio in $NiAl_2O_4$ from 0.50 (stoichiometric) to 0.13 (Ni deficient spinel), effectively trending the spinel toward a pseudo $\gamma$-$Al_2O_3$ structure.[160] One discrepancy comes at $x \approx 0.25$, where their measured $E_g$ value is much larger than the results presented here. This can be explained by examining the synthesis route, where coprecipitation methods and modest firing temperatures were used, which may affect the cation distribution and consequently the $M_o$-O bonds. The pairing of these result indicates that Ni bearing aluminate spinel, regardless of the Ni content down to $x \approx 0.25$, have Ni preferentially occupying the octahedral site which is in excellent agreement with the results found by Porta et al.[23] Furthermore, as Mg is substituted for Ni in $NiAl_2O_4$, the inversion parameter reduces to a value indicative of normal spinel, as observed by O'Quinn et al.[29] This suggests that Mg is not substituted onto the Ni octahedral sites, rather Mg occupies the tetrahedral positions. As most of the Ni is octahedrally coordinated in inverse spinel, Ni removal forces Al to switch from tetrahedral to octahedral coordination to account for the Mg additions on the tetrahedral sites. Inversion can be attributed to the negative deviation in the $E_g$ band with composition, where either defects or Mg substitution causes bonding changes that shift the band position below the linear trend.

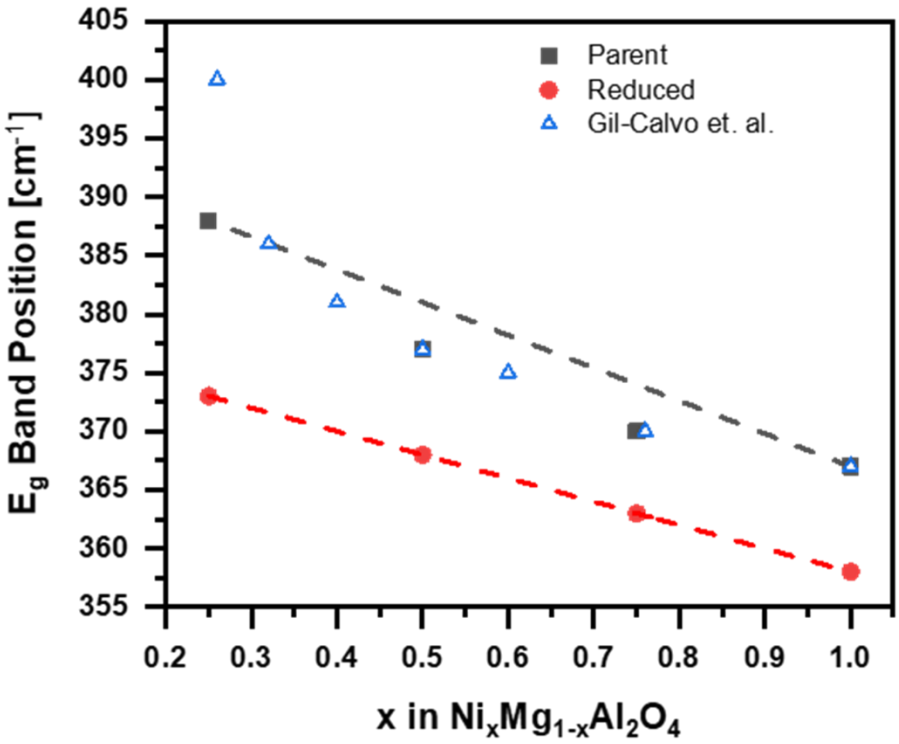


**Figure 18: Change in Raman band $E_g$ with spinel composition. Dotted lines represent linear fits between x = 0.25 and x = 1.0 members measured in this study.**

Now if one considers the $E_g$ band of the reduced spinel solid solution, a linear trend is observed with composition. The trend indicates that reduction along with Mg substitution orders the octahedral position linearly with composition. This is most likely due to cation octahedral site preference under the reduction conditions, where for the solid solution series refined values from XRD show the octahedral site is occupied more than the tetrahedral site, demonstrated by Hill.[64] This effect is apparent at the highest reduction temperature studied, where the tetrahedral occupancy decreases by ≈25%, and the octahedral occupancy decreases by ≈5% for the $NiAl_2O_4$ composition. Assuming that $NiAl_2O_4$ is completely inverse, i.e. all Ni is in octahedral coordination, the $Al^{3+}$ on the tetrahedral sites must change to the octahedral position upon reduction to describe the data trend. Even in the case where the inversion is slightly less than unity, which is the case for most inverse spinel,[23] only 11% of tetrahedral positions will be occupied by Ni, which is not enough to account for the ≈25% loss in tetrahedral occupancy. The remainder must be from $Al^{3+}$ changing from the tetrahedral to octahedral positions, which can occur for all solid solution

compositions. Therefore, it can be concluded that the effects of Mg additions as well as the reduction process results in a linear trend in the octahedral bond vibration by some cation redistribution from tetrahedral to octahedral lattice positions, aligning with previous *in-situ* neutron diffraction studies on reduced spinel from our group.[65]

To better correlate morphological to structural changes at the surface, Raman spectroscopy was performed on $NiAl_2O_4$ + 2.5 wt.% $ZrO_2$ previously reduced at 750°C and reoxidized in air at 1100°C and in the SEM at 1150°C (vacuum, $p_{O_2}$≈2·10$^{-10}$ atm.), as shown in Figure 19 (see Table VI for refined peak positions). The as-prepared parent oxide as well as the reduced analogue are provided as a reference. Clearly, the vacuum reoxidized spinel in comparison to the air reoxidized sample has major differences in the Raman fingerprint. Overall, bands appear much sharper in the air oxidized sample, with defined peaks at positions as described by Laguna-Bercero et al.[60] In comparison, the vacuum reoxidized sample has broad bands similar to the reduced analogue, indicative of some variation in the bonding, i.e. surface disorder. This result is not unexpected, as during the reduction it has been shown that Ni metal formation is accompanied by $V''_{Ni}$ and $V_{\ddot{O}}$ for charge neutrality[62], where the $V_{\ddot{O}}$ migrates to the surface as evidenced by neutron diffraction.[65] It is fathomable that not all of the oxygen point defects are eliminated in an atmosphere deficient of oxygen, i.e. under high vacuum conditions.

**Table VI: Fitted band positions for Raman spectra of $NiAl_2O_4$ + 2.5 wt.% $ZrO_2$ under various redox conditions. $ZrO_2$ fitted bands have been omitted. * - denotes possible discrepancy with $ZrO_2$ Raman bands. X denotes unassigned bands.**

| | **Mode Symmetry, $\nu$ [cm$^{-1}$]** | | | | | | | | | | |
|---|---|---|---|---|---|---|---|---|---|---|---|
| **Redox State** | **$E_g$** | **X** | **$T_{2g}$** | | | **$A_{1g}$** | | | | | |
| As-prepared | 367 | 452* | 315 | 553 | 602 | - | 717 | - | 763 | - | 825 |
| Reduced 750°C | 358 | 461 | 323 | 576 | - | 663 | - | - | 764 | - | 809 |
| Reoxidized in SEM Vacuum | 359 | 466 | 315 | 546 | 594 | 669 | - | - | 766 | 797 | 825 |
| Reoxidized in Air | 366 | 471 | 316 | 550 | 601 | 679 | 715 | 758 | 778 | 816 | 836 |

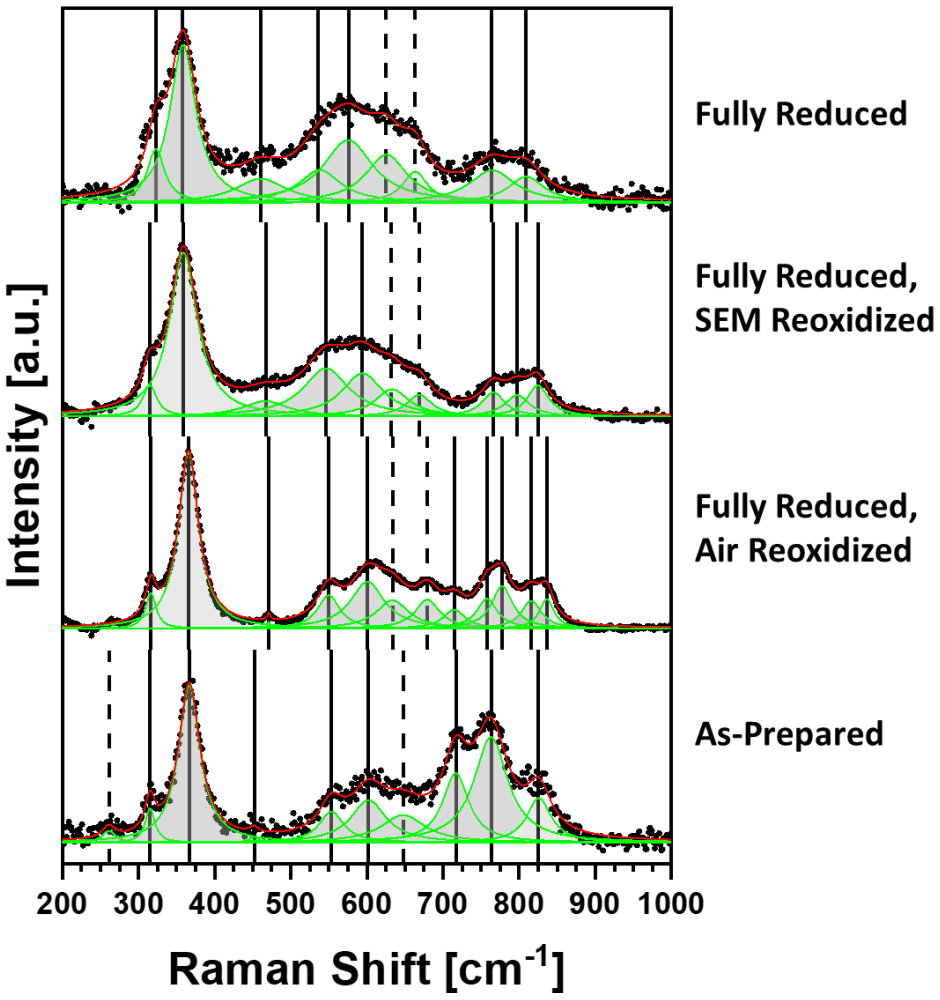


**Figure 19: Raman spectra of $NiAl_2O_4$ + 2.5 wt.% $ZrO_2$ at different redox conditions as labeled. Dotted lines represent fitted bands that overlap with $ZrO_2$ polymorphs.**

Band positions of the high frequency $A_{1g}$ region are diagnostic of the mixed $M_t$-O and $M_o$-O bond oscillations. The vacuum oxidized sample in this region exhibits band positions similar to those of the as-prepared oxide and are noticeably shifted compared to the reduced analogue. Interestingly, the air reoxidized sample has additional bands which, in comparison to the as-prepared sample, appear as doublets rather than single bands. The splitting and shifting of bands indicate some structural reorganization of the bonding after reduction and subsequent reoxidation in both air and vacuum, most likely manifesting as changes in the cation distribution over the tetrahedral and octahedral sites. Furthermore, inspection of the major $E_g$ band which is diagnostic of the $M_o$-O bond vibration, reveals

that the air reoxidized sample has a nearly identical band position compared to the as-prepared sample, where the vacuum reoxidized sample matches the reduced analogue. These results in combination suggest that after reduction and reoxidation, cations occupying the octahedral positions undergo minimal change, where the tetrahedral cation positions experience a much more dramatic transformation, at least in the near surface region under oxidation in air.

The vacuum oxidized sample exhibits some broadening due to the retention of reduction induced disorder, but to a lesser extent than the reduced sample. Again, as posited in the HTXRD section, band sharpening implies some structural reorganization occurs during oxidation in low $p_{O_2}$. Also, intensity changes in all features can be attributed to some structural relaxation from the reduced state. It is very likely that the vacuum oxidized sample is effectively a snapshot of the intermediate surface structure between the reduced and fully regenerated state, where neither the cation redistribution nor the elimination of defects has reached equilibrium. It is of note that the vacuum oxidized sample was held at the maximum temperature of 1150°C for less than an hour, whereas the air oxidized sample was equilibrated for 8h at 1100°C. If this quasi-equilibrium state is indeed the case, the presence of near surface defects most likely in the form of cation disorder may play a vital role in surface and or structural reconstruction as well as enhanced diffusion.

These results suggest the following sequence during the redox process:

1. On reduction: Removal of Ni (where a vast majority of Ni originally resides in octahedral coordination) results in noticeable changes for bands that perturb octahedral bonds, i.e. $E_g$ and $A_{1g}$.
    a. Vacancies are created on the sites and most likely some $Al^{3+}$ ions change from tetrahedral to octahedral coordination to maintain overall charge neutrality.
2. Reoxidation in air: Ni is reincorporated back into the structure with oxygen; however, the cation distribution is altered compared to the as-prepared sample.
    a. The $E_g$ band (solely $M_o$-O perturbation) changes very little, while mixed tetrahedral and octahedral $A_{1g}$ bands evolve from singlets to doublets. This indicates the cation redistribution experienced by reduction is not reversed

upon oxidation, i.e. the tetrahedral positions experience more change in cation occupancy.

3. Reoxidation at SEM $p_{O_2}$: Ni (and trace O) is reincorporated to a lesser extent than the air reoxidized sample, resembling the reduced spinel; however, some cation redistribution occurs.
    a. The $E_g$ band position is similar between the vacuum reoxidized sample and the reduced sample, indicating the bonding is similar. The vacuum reoxidized $E_g$ band is less broad than the reduced analogue, indicating some recovery of structural order.
    b. $A_{1g}$ mixed octahedral and tetrahedral bands change intensity, indicative of some cation redistribution.
    c. The vacuum oxidized sample can be viewed as a snapshot of an intermediate between reduced and reoxidized states.

**4. Scanning Electron Microscopy**

**a. Solid Solution Series – $Ni_xMg_{1-x}Al_2O_4$**

To address differences in the microstructure of the solid solution series, SEM analysis was undertaken. There is little difference between the two end members of the solid solution, as depicted in Figure 20, which is expected because the spinel inversion does not significantly alter morphology. Truncated triangles and squares characteristic of {111} and {100} planes are present throughout the microstructure, as these are the most energetically favored planes in the spinel system.[161] The amount of step edges and terraces of the particles is the main difference of note, which may be explained by the surface energy driven crystal roughening dependence upon the degree of inversion. Recall that $NiAl_2O_4$ is highly inverse, where $MgAl_2O_4$ is predominately a normal spinel. Increased inversion has been found in $MgAl_2O_4$ significantly stabilizing the {111} planes upon relaxation,[162, 163] demonstrating that inversion drives stabilization of this plane family in spinel. This causes terminations of the {111}, predominately by the {100} and some {110} in the form of steps and small terraces. It can be clearly seen that the $NiAl_2O_4$ sample exhibits a higher number of step and terraces, specifically with distinct truncated {111} triangles and {100} squares, while the $MgAl_2O_4$ sample exhibits smooth faces of the same planes, despite similar melting (and by extension crystal roughening) temperatures of 2110

and 2135 °C, respectively.[164, 165] The large bulbous features interrupting the microstructure are modifying $ZrO_2$.

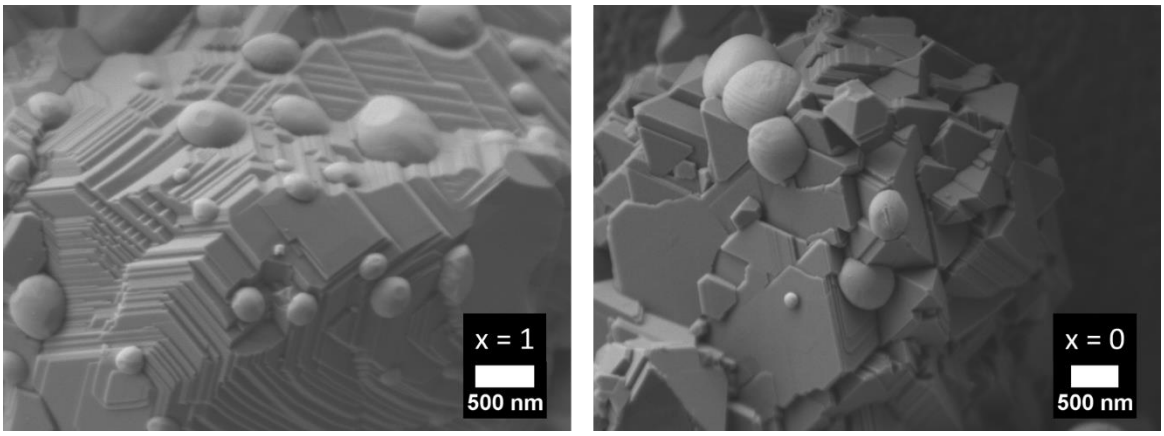


**Figure 20: SEM images of the end members of the solid solution, $Ni_xMg_{1-x}Al_2O_4$.**

### b. Morphological Changes upon Redox Cycling: Air

Exposure to reduction/oxidation conditions at high temperatures similar to the ones previously described in the HTXRD sections have marked effects on the microstructure; however, the general faceted motif in Figure 20 persists. Figure 21A-C illustrate the morphological progression of the redox process in air, as Figure 21A represents the as-prepared oxide. Upon reduction, metal particles are exsolved from the spinel (Figure 21B), where the size and number density are a function of temperature and time, based on previous studies.[62, 64] The removal of metallic Ni from the lattice causes up to a 6% contraction of the spinel which culminates visually as small pits and microcracks along the surface. Reoxidation in dry air at 900 °C for 1h (Figure 21C) produces relatively large metal oxide particles compared to the small metallic particles observed in the reduction. As mentioned previously, if allowed sufficient time at temperature, the NiO should react with defect and metastable spinel, completing the regeneration process.

Larger metal oxide particles arise, presumably, from surface transport and sintering mechanisms that minimize catalytic surface area. As catalyst efficiency is of interest to the scientific community and the surface area of catalytically active particles have been linked to higher catalysis rates,[11, 166, 167] the mechanism of the metallic oxide particle sintering is of importance and will be discussed in detail in subsequent sections.

Metal oxide particles persist throughout the oxidation process, even at 1100 °C, as evidenced in the HTXRD experiments. Microcracking, as well as pits induced by

reduction, is present even after oxidation, rendering the pits and microcracks permanent features of the microstructure under these conditions, effectively texturing the surface and evolving the microstructure as demonstrated in Figure 21C.

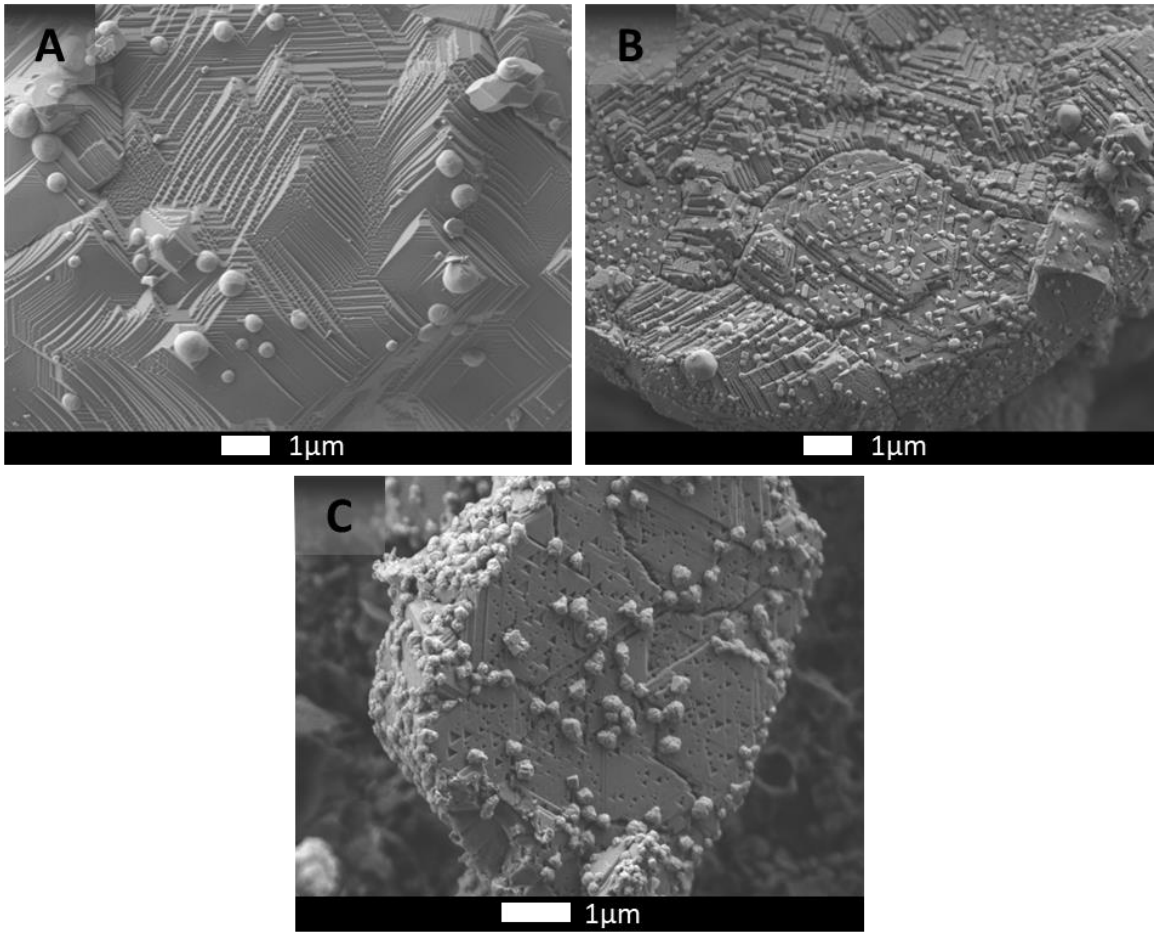


**Figure 21: $NiAl_2O_4$ + 2.5 wt. % $ZrO_2$ in the following states: A – as prepared, B – Reduced in $H_2$ at 900 °C for 12h, and C – regenerated at 900 °C in air for 1h.**

Observed pits from initial reduction and reoxidation resemble etch pits, which are known to be terminations of dislocations at the surface, as observed in LiF by Gilman.[168] Thermal etch pitting was also observed by Morita et al. on $MgAl_2O_4$ by deformation along specific crystallographic axes at high temperatures, specifically triangular etch pits on {111}.[169] It can be envisioned that the dislocation (or other defective features such as cracks from lattice constrictions upon reduction) act as short-circuit diffusion pathways which allow for enhanced diffusion of metal and oxygen to and from the bulk depending on the reduction or oxidation conditions. It should be noted that prototypical metallic crystals have

an inherently larger dislocation density, ρ, as compared to ceramic materials (stainless steel[170-172] – $\rho \approx 10^{14\text{-}15}\,m^2$, sapphire at 1400 °C[173] – $\rho \approx 10^{10}\,m^2$, YSZ 1% deformation at 600 °C[173] – $\rho \approx 10^{9}\,m^2$, $MgAl_2O_4$ at 1% deformation and 1400 °C[174] – $\rho \approx 10^{8}\,m^2$). Needle-like features on cross-sectioned reduced samples have been observed in the bulk for this system in the literature[103] as well as by our group,[72, 135] and for other mixed oxides with reduced metals[175] demonstrating that these short-circuit diffusion pathways occur in $NiAl_2O_4$. Internal reduction features demonstrate that reduction as well as oxidation and regeneration can occur via enhanced diffusion by short- circuit pathways to the bulk of the sample, allowing for oxidized metallic particles to react with remnant spinel. Alternatively, these conduits may be closed at the surface during the beginning of regeneration as they are in contact with the oxidative atmosphere, effectively severing the fast diffusion pathway and slowing the regeneration rate to that of bulk diffusion.

### c. Morphological Changes upon Redox Cycling: Low $p_{O_2}$

To further investigate the stability of surface pits created during reduction at low $p_{O_2}$, reoxidation was studied under an oxygen pressure of $\approx 9 \cdot 10^{-5}$ atm. via the low vacuum mode and the Protochips heating stage within the SEM. Since low vacuum *in-situ* observation is problematic at elevated temperatures due to thermal electron emission from the injected gaseous species, a post-mortem approach was used on previously reduced spinel at 750 °C. Exhibited in Figure 22A, the prototypical microstructure of spinel oxidized in vacuum at 1100°C can be seen. Pitting of the surface is most prevalent on the spinel surface, with some small microcracking observed. The absence of vast amounts of microcracking as shown in Figure 22 as compared to Figure 21 is expected due to the lower reduction temperature, resulting in less reduction induced lattice strain. The absence of the metal oxide particles is expected, as no reflections were observed in the HTSEM experiments. As shown in Figure 22B, the surface pitting and microcracking remain intact, despite heating to 1100°C for 4h in air, reinforcing their enduring imprint on the matured microstructure.

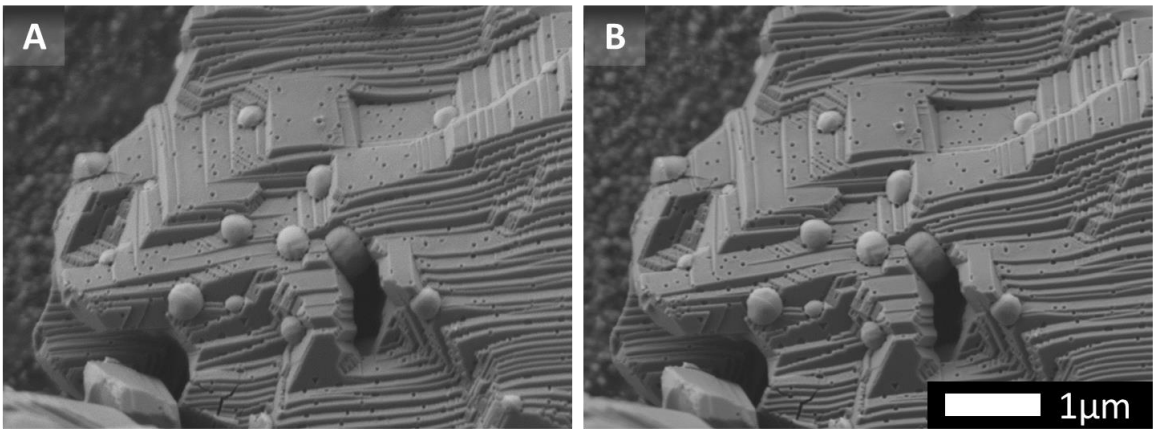


**Figure 22: $NiAl_2O_4$ + 2.5 wt. % $ZrO_2$ previously reduced at 750°C and A) reoxidized in vacuum (≈$2 \cdot 10^{-10}$ atm. $O_2$) at 1100°C; B) heat treated to 1100°C in air for 4 hours after reoxidation. Scale bars are the same for both images.**

Upon closer investigation, these observed pits and microcracks display fascinating morphological changes when exposed to heat and oxygen. Displayed in Figure 23, both pits and microcracks sharpen after 1h at 1100°C in $9 \cdot 10^{-5}$ atm. $p_{O_2}$ to minimize undercoordinated surface features as denoted by the image annotations. Hexagons sharpen into defined triangles indicative of {111} faces. As noted previously,[65] crystal faceting occurs rapidly above 1300°C, and certainly at the synthesis temperature of 1500°C. At 1100°C, it is not difficult to envision that surface reconstruction occurs, although qualitatively less than at 1300°C.

Regeneration induced microstructural evolution of this nature is in some cases favorable; for example, it was reported by our group that the methane conversions improved under 20 ppm $H_2S$ after regenerating a (Ni-Co-Mg)$Al_2O_4$ catalyst,[65] likely a result of improved $CO_2$ activation on the undercoordinated surface features. It has been found that cycled catalysts have similar if not improved catalytic properties,[95-97, 176] which also has been hypothesized as microstructural maturation.[65] While cycling and catalytic activity experiments were not conducted during this study, the work supports this claim that new surface features are responsible for the performance stabilization. Enhancement of the undercoordinated surface features also provides atomically defined step edges for methane reaction or additional Ni exsolution sites during reduction.

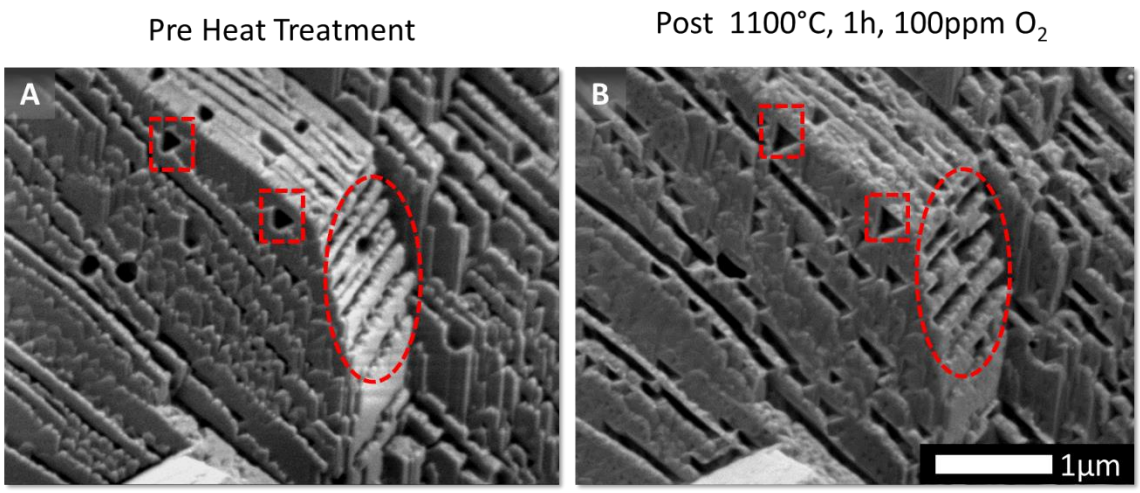


**Figure 23: $NiAl_2O_4$ + 2.5 wt. % $ZrO_2$ previously reduced at 900°C and reoxidized in vacuum (45 Pa ≈ $9 \cdot 10^{-5}$ atm $p_{O_2}$) at 1100°C, pre annealed sample (A) and post heat treatment (B) at 1100°C for 1 hour in air. Features are marked as discussed within the text. Scale bar is identical for both images.**

### 5. *In-situ* Low Voltage High Temperature Scanning Electron Microscopy

Previous sections addressed the *in-situ* stability and *ex-situ* microstructural ramifications of redox cycling on spinel in the solid solution $Ni_xMg_{1-x}Al_2O_4$ + 2.5 wt. % $ZrO_2$. The following section will address the *in-situ* microstructural changes on heating to shed light on the intermediate steps of the observed phenomena in the previous section, cast in terms of evidence of enhanced mass and surface transport.

#### a. Tracking Regeneration of Previously Reduced $NiAl_2O_4$ + 2.5 wt. % $ZrO_2$

Previous studies by the author on reduced spinel of the x = 1 composition was investigated by accelerated HTSEM experiments in vacuum, normally between 45 and 90 minutes in duration.[135] Results on the x = 1.0 composition in this section are from the aforementioned study, combined with similar experiments on other compositions and extended discussion pertaining to enhanced mass and surface transport.

$NiAl_2O_4$ + 2.5 wt. % $ZrO_2$ previously reduced at 900°C was used to track Ni particle movement on the defective support surface at relevant service $p_{O_2}$ ($2 \cdot 10^{-10}$ atm.) and temperatures (up to 1100°C). Individual photographs harvested from video recordings are compiled in Figure 24, showing the migration, coalescence, and resorption of the Ni surface particles. During heating, particles were observed to be stationary below ≈750°C,

as expected from the HTXRD in 4% $H_2/N_2$ and previous reports.[72] Above 900°C, which is above the reduction temperature, Ni particle migration and coalescence occur rapidly, within minutes. This particle migration and coalescence revealed an extensive amount of spinel surface pitting, originally masked by the reduced metal, indicating a Ni particle-surface pitting relationship characteristic of exsolved particles.[14, 17] As the temperature increased to 1100°C, particles unexpectedly resorbed into the support, suggesting oxidation of Ni to NiO which is highly reactive with the defective spinel surface. The oxygen source is unclear due to the low base pressure within the SEM, $p_{O_2} \approx 2 \cdot 10^{-10}$ atm, which according to the Ellingham diagram is slightly in the Ni reduction region at 1100°C.[177]

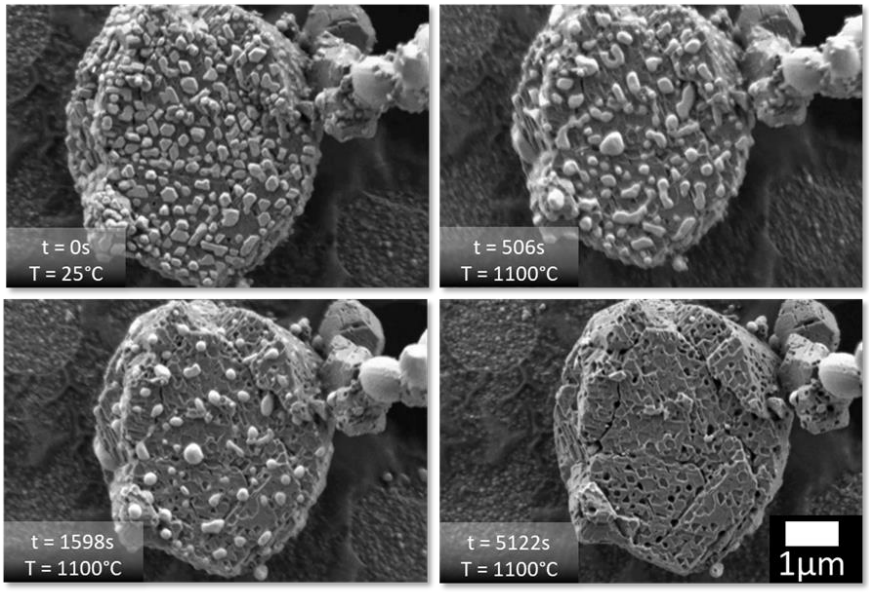


**Figure 24: Time lapse images of *in-situ* HTSEM on x = 1 composition. Time and temperature of each image is on the bottom left of the corresponding image. The provided scale bar is identical for all images.**

Another experiment was conducted at higher magnification to probe and identify any nanoscale mechanisms that might be affecting the observed particle migration and coalescence, as well as the resorption. Figure 25 shows time lapse images from the processed video, where Ni particles were shown to migrate and coalesce as in the previous experiment, highlighted by the annotations. The arrow denotes a modifying $ZrO_2$ particle. Above the reduction temperature, but below the temperature at which the particles cease migrating (1000°C), Ni particles are exsolved from the surface, leaving behind shallow

texturing, shown by the dotted circles and rectangles. The slight microstructural modifications reinforce the Ni particle – pit relationship. Exsolution is expected at 1000°C and sufficiently low $p_{O_2}$, given that the initial reduction temperature was 900°C, and that Ni exsolution is a thermally activated process.[64, 65] As the temperature increased to 1100°C, reincorporation of the Ni particles into the remnant spinel occurs as previously mentioned.

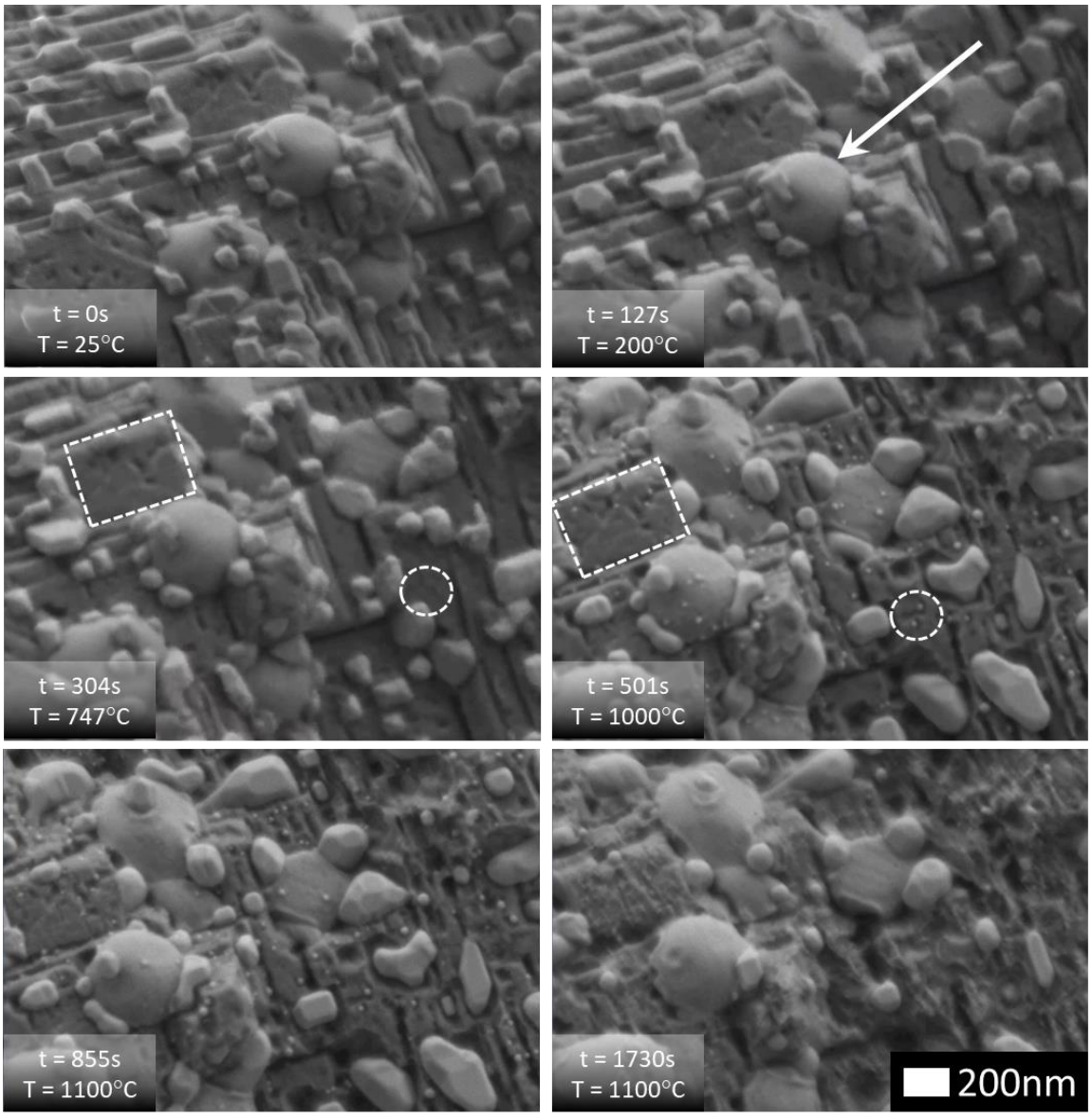


**Figure 25: Time lapse images from the HTSEM nanoscale investigation on the x = 1 composition with time and temperature denoted in the bottom left of each image. Features marked are discussed in the text. Scale bar is identical for all images.**

It is known that oxygen anion diffusion in spinel is remarkably slow, attributable to the close-packed oxygen sublattice even in highly defective spinel.[33, 178, 179] Cation diffusion is much faster, as the A and B site cations can jump through octahedral and tetrahedral interstitial sites on the oxygen sublattice and by vacancy mechanisms.[180] Defective spinel formed by reduction may have a large number of metal and oxygen vacancies not encountered in typical spinel, allowing for enhanced diffusion as evidenced by the previous XRD and Raman sections. Surface particle diffusion on this scale has not been studied previously, nor has the effect of the defective support. However, it is apparent from the HTSEM that the formation of large Ni particles creates surface texturing on the spinel in the form of pits which follow the contours of the metallic crystals. In other words, the crystallites are embedded within the spinel surface, not residing on the surface, with no preferred crystallographic registry. Embedded particles have been shown in studies focused on exsolvable perovskite systems, where particle size, distribution, anchoring, and coking resistance can be engineered, depending upon application.[11, 14-16]

Regarding the catalyst function as well as the regeneration process, the size and distribution of the metallic particles as well as the redox condition of the support are considered. The HTSEM results establish that mass particle migration and coalescence can occur rapidly, within seconds, depending on the temperature within the HTSEM and the original reduction temperature (i.e. above 750°C). Particle migration and coalescence of this nature has been studied on Ni based catalysts ($SiO_2$, $MgAl_2O_4$ and $MgAl_2O_4$ + $ZrO_2$ supports) by measurement of surface areas and modeling based upon kinetic rate laws from ≈500-600°C.[81, 82, 181] *In-situ* observations have been limited to TEM experiments, where both Ostwald ripening and particle migration type mechanisms have been identified in metallic nanoparticle systems (comprehensive reviews in [80, 84, 86]). The possibility of Ostwald ripening in the system under investigation is not discounted; however, it was only shown to occur for an analogous Ni/$MgAl_2O_4$ system during the initial stages of sintering at much lower temperatures than used in this study.[182] In addition, Ostwald ripening on short time scales (<5 seconds) in the aforementioned study is not expected to be observed as single atoms cannot be imaged by the SEM.

### b. Quantification of Particle Migration on Defective Supports

Spherical objects (bubbles, particles, etc.) are assumed to collide and coalesce as they migrate through a medium or along the surface. Analytical equations for spherical bubble migration were derived by Gruber using the Nernst-Einstein relation in combination with flux and force arguments.[183] Wynblatt and Gjostein extended these derivations to solid particles diffusing along a support surface, noting that particles must not wet the surface.[184] Based on these equations, Sehested and coworkers determined the mechanism for sintering on $Ni/MgAl_2O_4$ catalysts by examination of the metallic particle size distribution after sintering, identifying particle migration and coalescence as the dominant mechanism.[76, 81, 82]

Observed particle migration distances in the current investigation over relatively short periods of time are much larger than predicted by Sehested et al., indicating enhanced transport along the surface of the spinel. In the migration and coalescence model,[184] by assuming a random walk and non-wetting spherical particles, the migration distance can be estimated by,

$$X_c = 2\sqrt{D_p t} \tag{12}$$

where t is time and $D_p$ is the diffusivity of the particle as derived by Gruber[183] to be,

$$D_p = 0.301 D_s \cdot \left(\frac{a}{r}\right)^4 \tag{13}$$

where $D_s$ is the surface diffusion coefficient, a is the atomic diameter (in the $NiAl_2O_4$ case, diffusing surface particles are composed of Ni with $a_{Ni}$ = 0.24nm) and r is the radius of the particle. If the particle is wetting the surface, the effective particle size increases, and $D_p \rightarrow 0$. It is apparent that the particle size dominates the $D_p$ and therefore $X_c$. Ni mass loadings used to derive these relations are similar to our loadings, for example 7.5 wt.% Ni for these samples reduced at 900°C[72] and 7.6-36.5 wt.% in the work of Sehested.[82]

It should also be noted that faceting of the mobile Ni particles impedes the migration by reducing $D_s$ by orders of magnitude.[181] Wynblatt and Gjostein pointed out that movement via the particle migration model of faceted mobile particles requires nucleation of monatomic steps, followed by adatom diffusion to the new step, which inherently controls the migration rate of the particle.[184] Metal particles lose initial faceting from reduction during the heating process in the HTSEM, typically around 700°C before

migration commences. No apparent faceting on the migrating Ni particles was readily observed once migration initiated, indicating no hindrance of movement in our system. at temperatures exceeding 1000°C Particle faceting was only observed after particles ceased moving.

It is posited that enhancement of the surface particle diffusion arises from the available defect content, specifically the extent of reduction of Ni from the spinel. To verify, Mg was substituted for Ni into the model catalyst, as Mg is not selectively reduced and hence the number of defects that may form by extraction of Ni and oxygen ions can be controlled by the Mg content.[62, 64] $NiAl_2O_4$ can inherently accommodate more defects as compared to the Mg substituted analogue under full reduction conditions, which is apparent as more Ni is extracted, for example, 2.0 and 0.4 wt. % Ni for $NiAl_2O_4$ and $Ni_{0.25}Mg_{0.75}Al_2O_4$, respectively.[64] *In-situ* SEM on $NiAl_2O_4$ and $Ni_{0.25}Mg_{0.75}Al_2O_4$ spinel reduced at 800 °C for 24 h revealed migration distances that greatly exceeded the predicted model in Equations (12) and (13). Over a temperature range from 800 to 900 °C, Ni particle migration displays an enhanced migration distances of ≈2-20 times for $Ni_{0.25}Mg_{0.75}Al_2O_4$ and ≈125-350 times for $NiAl_2O_4$ the predicted value depending on temperature (see Figure 26). From 800-850°C, the ratio of observed migration distance to the predicted distance shows a linear trend with temperature for Mg substituted spinel whereas the full Ni spinel is relatively constant. Above 850°C, the ratio deviates from linearity, suggesting a mechanistic change in the transport. From the HTXRD on $NiAl_2O_4$ in air and $N_2$ experiments previously discussed (Figure 15), residual microstrain from the reduction process was significantly reduced at temperatures above 900°C for air and 1000°C for $N_2$. Furthermore, spinel wt. % measured by the Rietveld method (inset Figure 14) began to increase (as well as Ni wt. % decrease) at 900°C during the $N_2$-HTXRD experiment. We interpret these results as bulk structural relaxation, presumably in the form of short-range restoration of the structure, i.e. elimination of point defects via the regeneration process restoring long-range order. The discrepancy in temperature between the HTSEM and HTXRD experiments can be simply explained by considering the bulk vs. surface nature of XRD and SEM respectively, where manifestation of structural relaxation on a bulk scale may be kinetically limited until higher temperatures are reached, whereas the (near) surface relaxation is likely not so kinetically limited.

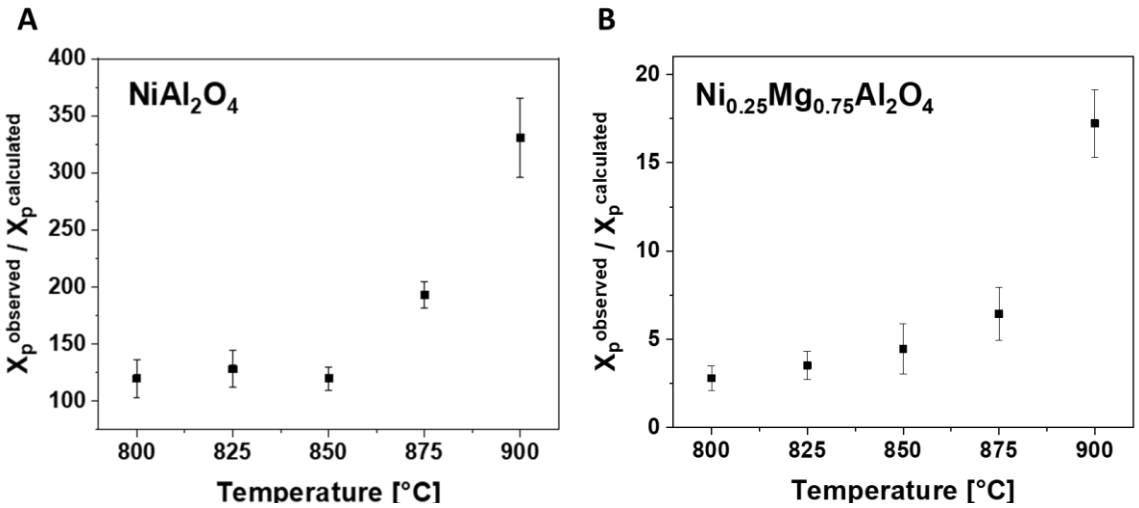


**Figure 26: Normalized particle migration distances for A) $NiAl_2O_4$ and B) $Ni_{0.25}Mg_{0.75}Al_2O_4$ between 800-900°C. Error bars provided are for at least four measurements.**

### c. Thermodynamic Assessment of Particle Oxidation and Regeneration

The regeneration reaction may proceed by oxidation of Ni to NiO (Equation (14), followed by reincorporation to regenerate the starting spinel, or by direct incorporation of Ni without detectable NiO formation. Bulk crystalline NiO was not detected during the HTXRD study under $N_2$ ($p_{O_2}$≈9.5·10$^{-6}$ atm.), and surely no bulk NiO forms as an intermediate in the HTSEM experiment. At $p_{O_2}$≈9.5·10$^{-6}$ atm. in the HTXRD study under $N_2$, NiO is thermodynamically favored to form at temperatures below ≈1500°C as indicated in the Ellingham diagram.[177] Nonetheless, the reaction clearly proceeds to form $NiAl_2O_4$ as the temperature or time increases. If the overall spinel formation reaction in Equation (15) is considered,[73, 185, 186] it becomes clear that spinel formation is in fact more thermodynamically stable than Ni oxidation, as evidenced by the more negative $\Delta G°_{spinel}$ in the Ellingham diagram (Figure 27). Recall that defective spinel resembles the $\gamma$-$Al_2O_3$ structure, and as such we use the known thermodynamic properties of $\gamma$-$Al_2O_3$.

$$2Ni(s) + O_2(g) \rightarrow 2NiO(s), \quad \Delta G°_{Ni-NiO} = -468{,}600 + 170.4 \cdot T \tag{14}$$

$$2Ni(s) + O_2(g) + 2(\gamma\text{-}Al_2O_3)\,(s) \rightarrow 2NiAl_2O_4(s), \quad \Delta G°_{spinel} = -527{,}800 + 181.6 \cdot T \tag{15}$$

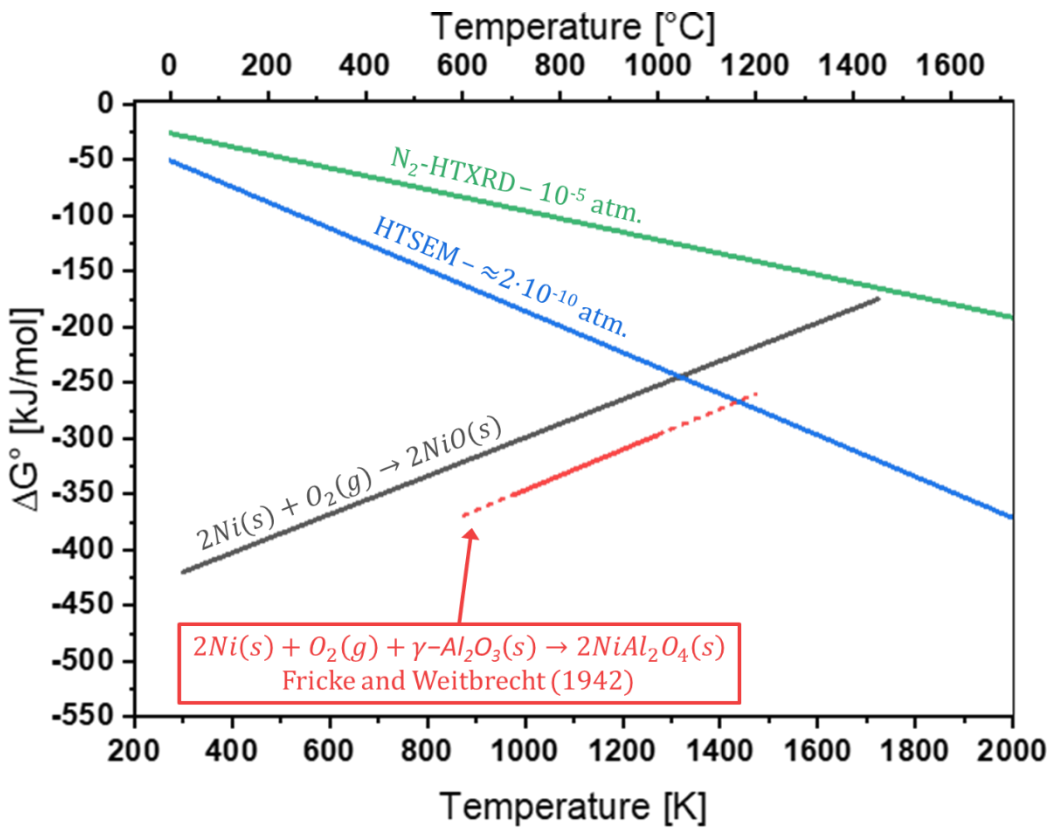


**Figure 27: Ellingham diagram constructed from Equation 4 and 5. HTSEM and N2-HTXRD traces are provided for reference. Dotted lines represent extrapolated data from the literature.**

It could be argued that Ni oxidation, reduction, reoxidation, and reincorporation do not occur, as a much simpler explanation is apparent. As evidenced by the $N_2$-HTXRD experiment at a notably higher $p_{O_2}$ than the HTSEM ($p_{O_2}$≈$10^{-5}$ and $2 \cdot 10^{-10}$ respectively), no NiO formation occurred, even though the reaction is thermodynamically favorable. Rietveld refinements on the *in-situ* data (inset Figure 14) demonstrate the systematic decrease in Ni wt. %, and increase in spinel wt. %, as well as reduction of residual microstrain in the system as the temperature increases, which is indicative of spinel regeneration even though no detectable NiO is present. This realization gives rise to the possibility that NiO is not a requirement for spinel phase regeneration, rather the regeneration pathway changes depending on the system $p_{O_2}$, as demonstrated as a scheme in Figure 28.

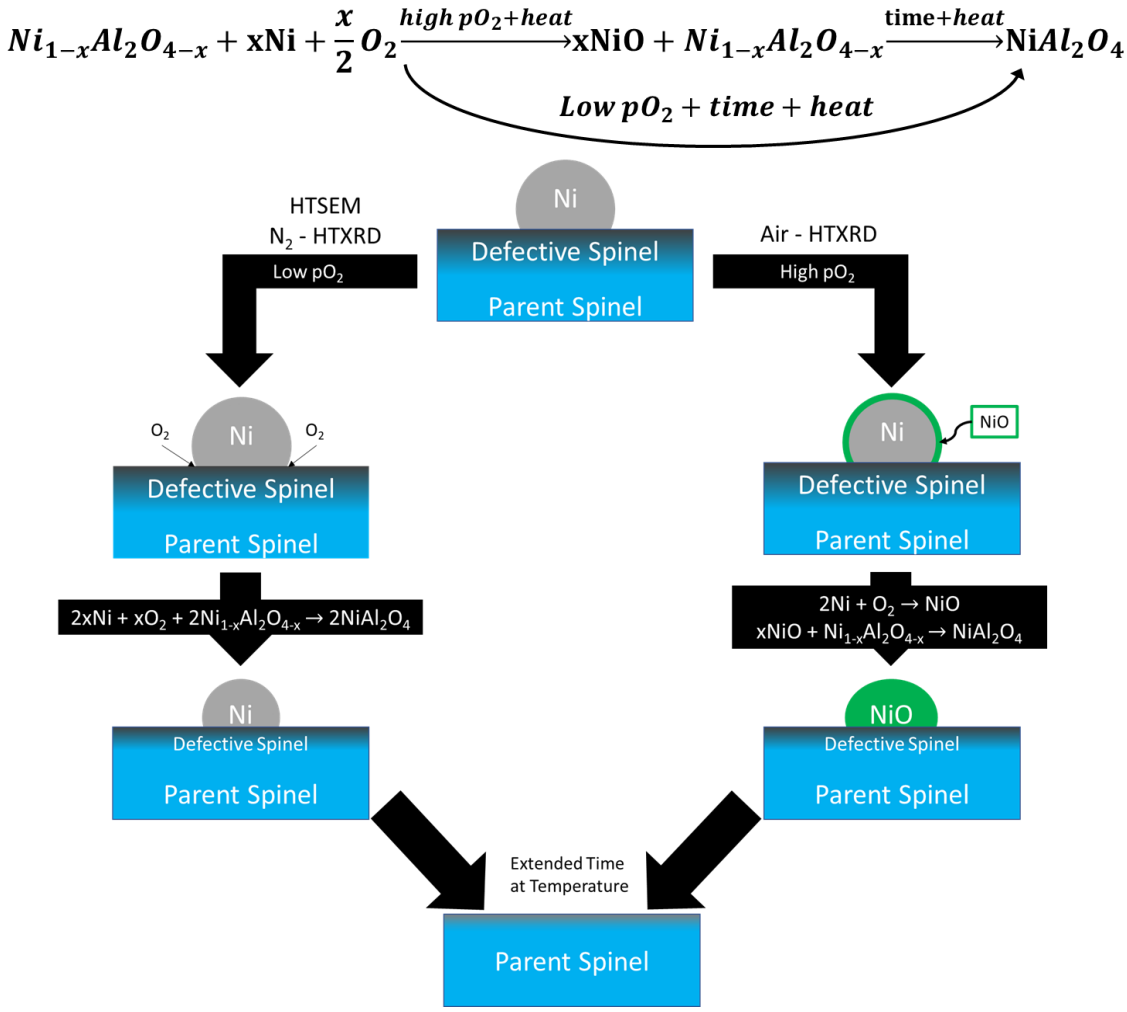


**Figure 28: Scheme representing the $p_{O_2}$ effects on regeneration for reduced $NiAl_2O_4$.**

Some residual Ni is present in the $N_2$-HTXRD data, where the HTSEM experiments show total resorption of the Ni particles, despite the HTXRD having higher $p_{O_2}$ and having extended amounts of time. This can be rationalized by acknowledging that the HTSEM and HTXRD probe inherently different parts of the sample. SEM is extremely surface sensitive within the first 1 nm, whereas XRD is a bulk technique measuring a few microns into the sample. SEM also does not probe the core of the spinel particles, which are known to have needle-like metallic crystallites from reduction.[72, 103, 135]

It is beneficial to acknowledge that simple thermodynamics may not completely account for kinetic and particle size considerations. It has been shown that surface energy effects on nanoscale transition metal oxides greatly alter redox equilibria and phase

stability,[187] whereas the Ellingham diagram is derived solely from the ΔG° of the bulk reaction.[177] Furthermore, conditions of the HTSEM experiments were not conducted under thermodynamic equilibrium conditions and so relying solely on the Ellingham diagram treatment is not appropriate. The metallic particles under examination are an order of magnitude larger than the Navrotsky et al. study, therefore, nano-scale implications may only contribute slightly if at all to the observed behavior. Being near the bulk equilibrium temperature (50 ± 10°C), the rate of the reduction reaction may be so sluggish that the reincorporation reaction on the surface dominates kinetically, as hinted at with the oxidation reaction during the previously discussed $N_2$-HTXRD experiment. Therefore, it is logical to assume that oxidation and reduction are rate-limiting steps, where reincorporation occurs much faster.

### d. Behavior of Parent Oxides in the HTSEM: $NiAl_2O_4$, $Ni_{0.5}Mg_{0.5}Al_2O_4$, $MgAl_2O_4$

During heating, small particles of exsolved Ni decorate the surface of the spinel around 700-750°C, shown in Figure 29, highlighted with dotted ovals. Exsolution of particles is not driven by excess energy provided by the beam; exsolution was observed throughout the heated area (for example, solid oval shown in Figure 29). Exsolved particles are highly mobile on the surface of the spinel, and increase in size by a particle migration and coalescence mechanism, as well as by more exsolution as the temperature is increased.[135] Once 900 °C is reached, particles cease their movement and seem to begin the regeneration process (possibly where regeneration kinetically dominates), with complete regeneration by 1000°C. The resulting surface of the spinel is mottled from the exsolution process, which is known to anchor particles into the support.[14-16] Other Ni bearing compositions exhibit the same phenomena as described above, at different temperatures, due to expedited heating rates as compared to the experiment described above and shown in Figure 29. $MgAl_2O_4$ + 2.5 wt.% $ZrO_2$ with no Ni present was also examined, but did not exhibit any of the aforenoted characteristics, however.

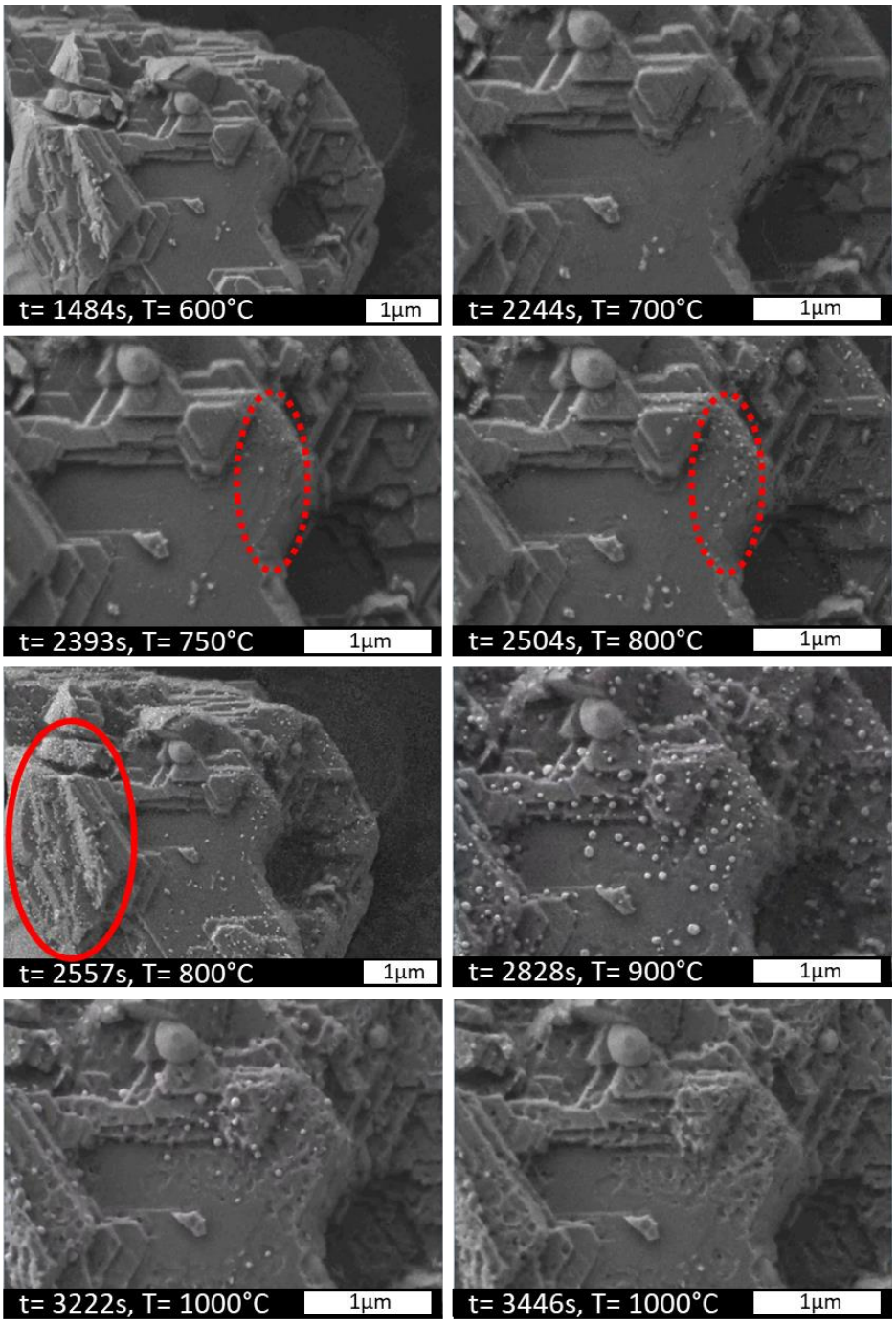


**Figure 29: Time lapse images of as prepared $NiAl_2O_4$ + 2.5 wt.% $ZrO_2$ heat *in-situ* under SEM vacuum ($2 \cdot 10^{-10}$ atm. $p_{O_2}$). Time and temperature are provided in bottom left. Annotations are as described in the text.**

Particle exsolution at seemingly low $p_{O_2}$ and low temperature ($p_{O_2}$≈2·10$^{-10}$ atm., T ≥ 750 °C) is a puzzling phenomenon but an explanation can be provided. Exsolution only occurred during the initial heating of the samples; subsequent heating did not cause any additional exsolution. Clearly, exsolution is not induced by electron beam-specimen interactions as exsolution is observed throughout the area heated by the Protochips stage. TEM observations on Co-doped (Ni, Zn)$Fe_2O_4$ spinel by Harmer et al. reveal that epitaxial Ni particles are reduced from the oxide during ion-milling, as well as *in-situ* at 625°C,[188] which is in relative agreement with our observations on the $NiAl_2O_4$ system at 700-750°C. Exsolved particle sizes by Harmer et al. were ≤50nm, where observed exsolved particles on $NiAl_2O_4$ were of similar size before migration and coalescence. However, the authors did not provide any mechanistic explanation for the phenomenon.

A later study on NiO-MgO solid-solutions showed the hydration state of the surface is responsible for selective reduction of the oxide to metal under electron irradiation, where extensive drying of the sample eliminated reduction.[189] Samples in the current study were mounted on the Protochips stage by using an ethanol-powder slurry which inherently contains trace amounts of water and certainly hydroxyl groups, suggesting that the reduction observed is from hydroxyl groups on the surface. This was confirmed by extensively drying a sample overnight and performing the same temperature profile in the HTSEM, in which no exsolution was observed.

Exsolution in chemistries other than $NiAl_2O_4$ that were not dried occurred at higher temperatures; reduction occurred around 900°C for $Ni_{0.5}Mg_{0.5}Al_2O_4$ and $Ni_{0.375}Co_{0.375}Mg_{0.25}Al_2O_4$ both with 2.5 wt.% $ZrO_2$ modifier. Onset temperature changes between these experiments should not vary drastically with the proposed mechanism; however, the latter experiments were not provided enough time to equilibrate at small temperature increments such as the full Ni spinel sample. All samples began to reduce at temperatures higher than 700°C, and given sufficient time, the other samples can be expected to exhibit the particle exsolution near this temperature.

It is important to note that these reactions are not occurring throughout the bulk, but on the spinel surface in short time durations. Shown by previous neutron diffraction work from our group, spinel reduction proceeds via a nucleation and growth mechanism in

a core-shell like manner, where the core is comprised of stoichiometric spinel and the shell is defective, for 60 minutes of reduction in 4% $H_2$ at 950°C.[65]

## C. Extension to Ni-Co-Mg Catalysts

In this section, attention is given to the structural and morphological changes experienced by a technologically relevant spinel catalyst, via HTXRD and intermittent SEM, modeled after the redox cycling conditions used in our previous catalysis studies: 12 h reduction in flowing 4%$H_2$/$N_2$, and oxidation in flowing dry air for 2 h, at 900 °C for both atmospheres.[65] Reincorporation of the (Ni,Co)O particles under these oxidation conditions is kinetically slow, making the regeneration highly incomplete. Therefore, the oxidation time was extended to a total of 20 hours to observe the surface features of a more complete regeneration cycle. In total, two complete redox cycles were completed, with SEM imaging after each reduction and oxidation segment. HTXRD redox profiles are shown in Figure 30, with SEM insets where samples were extracted after cooling to room temperature. Intermediate room temperature patterns were removed for pattern continuity.

In general, Ni-Co bimetallic additions to catalysts improve coking resistance and oxidative deactivation of fuel reforming catalysts when incorporated in the correct ratio.[190, 191] A synergistic effect is produced: excess Ni slows oxygen production from $CO_2$ and therefore cannot oxidatively remove the deposited carbon from $CH_4$, where excess Co increases the reaction rate and produces too much coke. Ni-Co bimetallic catalysts supported on spinel of similar composition to this study were identified by Zhang et al. to have superior performance based on the metallic particle size and distribution, where the high surface area spinel mediated the metallic particle size and provided good thermal stability via support-metal interactions.[166, 192] Previous work from our group for this particular composition shows marked improvements on oxidative sulfur removal, attributed to the crystal perfection at the elevated sintering temperature and to the addition of Co.[65] Ni and Co additions in tandem with the $ZrO_2$ modifier may, in fact, provide additional oxygen vacancies which facilitate oxygen storage and transfer via variable oxidation states ($Co^{2+}$/$Co^{3+}$ and $Ni^{2+}$/$Ni^{3+}$).

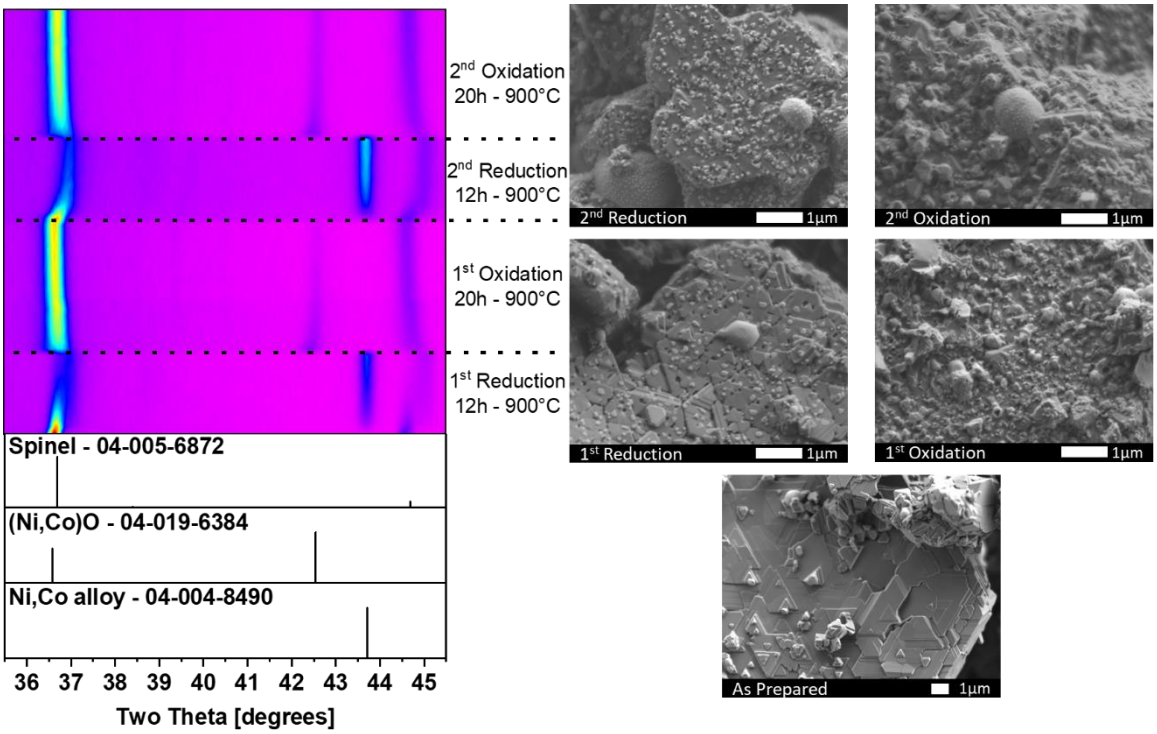


**Figure 30: Heatmap of *in-situ* XRD data showing redox cycling of $Ni_{0.375}Co_{0.375}Mg_{0.25}Al_2O_4$ + 2.5 wt.% $ZrO_2$ with corresponding SEM images. Images correspond to labels in HTXRD heatmap, as indicated by dotted lines.**

The spinel already contains point defects from selective reduction; however, some Ni and Co remain within the support post reduction. These factors may in fact facilitate expedited surface reconstruction, and certainly will affect reforming reaction kinetics. In addition to improved sulfur removal, regeneration of the Ni-Co-Mg spinel catalyst improved catalytic performance attributable to microstructural evolution (or the inability for the spinel surface to repair the surface cracking and pits)[65] allowing for greater particle dispersion.

The as-prepared oxide is structurally and morphologically akin to $NiAl_2O_4$. Phases of pure spinel, with dual phase m- and t-$ZrO_2$ are present. SEM revealed that triangular facets on the as-prepared oxide representative of {111} faces are the prominent surface feature, with shallow step faceting. $ZrO_2$ was rendered as bulbous spheroids in contact with the spinel on the surface, which remained relatively unchanged by the redox process. Subtle bands on the $ZrO_2$ are indicative of monoclinic phase twinning; a result arising from the presence of the tetragonal phase at elevated temperatures.

Upon reduction at 900°C for 12h in flowing 4% $H_2$, spinel reflections are shown to decrease in intensity as the Ni, Co, and O are extracted from the spinel. Alloy reflections cease increasing in intensity between 11 and 12 hours, which is in agreement with previous studies on $Ni_xMg_{1-x}Al_2O_4$.[62] Spinel, metal, and the $ZrO_2$ polymorphs were present at room temperature after the isothermal treatment. From Rietveld refinements, ≈22 wt.% metal is present after the 12-hour reduction at 900°C, which is doubled as compared to the $Ni_{0.75}Mg_{0.25}Al_2O_4$ sample (11.4 wt.% at 900°C for 12h),[72] revealing considerably faster reduction kinetics for this particular composition. The lattice parameter of the spinel decreases by ≈1% (≈3% volume decrease) resulting from Ni/Co and O removal. Surface investigation of the spinel after reduction by SEM showed Ni-Co metal alloy particles with an average diameter of 166 ± 44 nm, with a particle number density of 16.5 ± 3.8 particles/$\mu m^2$. Pits and elongated voids are also present, as visual manifestations of the volume decrease.

From HTXRD, the spinel lattice parameter increases throughout the isothermal oxidation treatment, indicating that regeneration occurs as (Ni,Co)O is integrated into the structure, seemingly reversing the reduction induced 3% volume contraction. However, the pits and cracks do not heal, evidenced in Figure 30. This result can be justified by recalling that XRD probes the bulk, where some vacancies are present causing the lattice to contract, which does not account for vacancies migrated to the surface. It is of note that the XRD derived crystallite size of the spinel increases within the first six hours of heat treatment then remains relatively constant over the remaining 14 hours of treatment. By examining patterns taken before and after heat treatment, an increase in lattice parameter by ≈0.7% was observed over the 20 hours, due to the regeneration process.

A second reduction was performed, resulting in identical phase assemblages to the previously discussed reduction cycle. However, the comparison reveals a higher concentration of metallic phase, as seen by the increased intensity in Figure 30, resulting in a 50% increase in the metal wt.% from the first reduction ($1^{st}$ – 22 wt.%, $2^{nd}$ – 33 wt.%). Metal morphology has noticeably altered from the first reduction; particles are much smaller and highly dispersed (72 ± 29 nm by SEM, 63.8 ± 6.1 particles/$\mu m^2$), residing on both $ZrO_2$ and spinel surfaces. Particles residing on spinel have spherical geometry, dissimilar to the highly geometrical large metal particles from the first reduction.

To complete the redox cycle, oxidation on the sample was conducted, where the spinel underwent regeneration as demonstrated previously. Investigation of the surface revealed mottling as after the first redox cycle; however, to a greater extent.

To summarize, after the first redox cycle, reduced Ni-Co-Mg spinel exhibits 50% more metal exsolution, higher particle number density, and smaller metallic particles as compared to the initial reduction counterpart. Structural variations are minor throughout the redox cycle as exhibited by HTXRD, whereas the morphology is vastly evolving with each cycle. Surface alterations manifest as catalytic performance improvements, resulting in performance (30% increase in $CH_4$ conversion) and stability (15% to <5% $CH_4$ conversion degradation) enhancement over 12 hours on stream in sulfur poisoning conditions.[65]

### D. Modifier Compositional Variations: Case Study of $NiAl_2O_4$ + 2.5 wt.% modifier

This section studies the variation of the modifying oxide composition on the spinel support considering the enhanced mass transport observed in previous sections. The goal was to identify modifier oxides that have similar properties to the $ZrO_2$ modifier oxide, but to test materials with known low oxygen ion conduction vs. those that show some oxygen ion conduction. Compositions, shorthand names, and the corresponding PDF numbers used in subsequent sections are denoted in Table VII.

**Table VII: Target modifying oxide compositions and the corresponding shorthand notation used in subsequent sections. WC- denotes a wash coating procedure followed by the temperature for some compositions.**

| Modifying Oxide | Shorthand Notation | Modifier PDF# |
|---|---|---|
| $ZrO_2$ | Ni1Zr | M – 04-010-6452<br>T – 04-005-4207 |
| $HfO_2$ | Ni1Hf | 04-005-4474 |
| $Nb_2O_5$ | Ni1Nb-WC600 | O – 04-007-0494<br>M – 04-007-0452 |
| $NiNb_2O_6$ | Ni1Nb-WC1000 | 01-072-0481 |
| $CeO_2$ | Ni1Ce-WC600 | 04-015-0471 |
| $TiO_2$ (Rutile) | Ni1Ti | 04-003-0648 |

### 1. X-ray Diffraction

To ensure no major structural changes occurred to the spinel or target modifier composition, XRD was employed to obtain the phase composition of the as-prepared oxide with varying modifier additions. All specimens had spinel reflections in the XRD patterns, with small signals from the modifying oxides (see Table VII for PDF numbers), shown in Figure 31. Rietveld analysis (Table VIII) confirms that the variance of the spinel lattice parameter is measurable, however, insignificant (<0.01% difference) as compared to the undoped sample. It is of note that none of the compositions achieved the target 2.5 wt. %, indicating some loss from the target wt.% modifying oxide during the synthesis or processing. Therefore, it can be concluded that cations from the modifier could be incorporated into the spinel, most likely on a limited basis due to only 2.5 wt. % being present. Rietveld analysis is also only accurate to about 1 wt. %, therefore the data presented is to obtain some semblance of the amount of modifier distributed upon the surface.

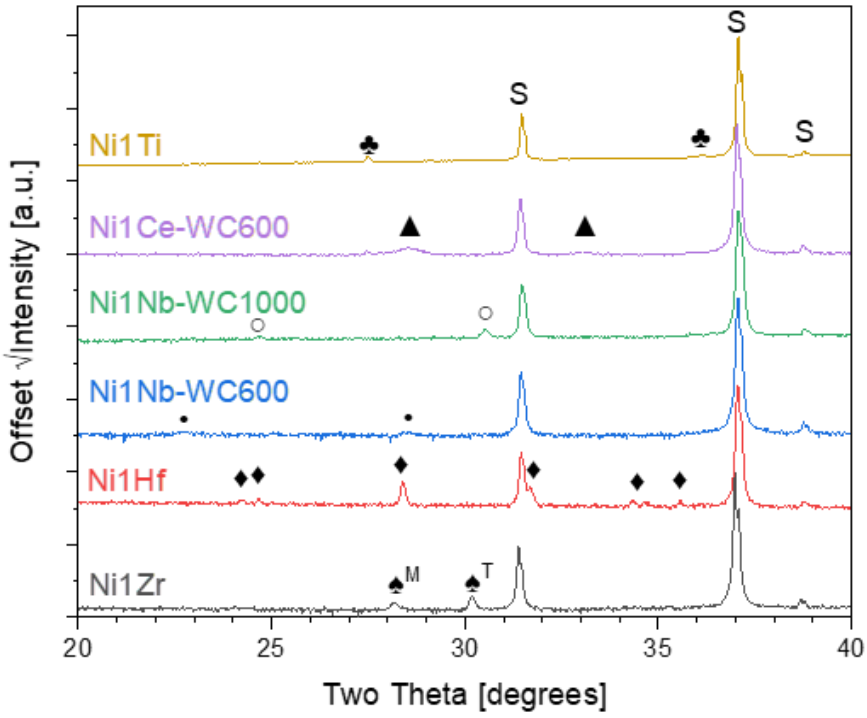


**Figure 31: XRD patterns of the as synthesized $NiAl_2O_4$ with varying the modifying oxide composition. "S" denotes the spinel reflections, whereas each symbol represents the characteristic peaks of the modifying oxide, as outlined in Table VII.**

**Table VIII: Spinel compositions with the corresponding spinel lattice parameter and the wt. % modifier for each composition. $NiAl_2O_4$ is shown for comparison.**

| Spinel Composition | Spinel Lattice Parameter [Å] | Wt.% Modifier |
|---|---|---|
| $NiAl_2O_4$ | 8.04626(7) | 0.0 |
| Ni1Zr | 8.04868(4) | 1.0 |
| Ni1Hf | 8.05048(10) | 2.3 |
| Ni1Nb-WC600 | 8.04481(6) | 0.2 |
| Ni1Nb-WC1000 | 8.04408(6) | 0.7 |
| Ni1Ce-WC600 | 8.04417(6) | 0.9 |
| Ni1Ti | 8.04832(5) | 1.1 |

In the most extreme case of $Nb_2O_5$ and $NiNb_2O_6$ doping where the most modifying cation was lost, incorporation into the spinel structure may be favorable in the octahedral site in small amounts.[116] $Ce^{4+}$ was also found to substitute for $Ni^{2+}$ in spinel with an increasing lattice constant due to the size of the $Ce^{4+}$ ion.[118] Since this is not the observed trend (8.04626 and 8.04417Å for $NiAl_2O_4$ and Ni1Ce-WC600 respectively) $Ce^{4+}$ must not substitute onto the spinel lattice. Ti and Zr have similar spinel lattice parameters, close to the original oxide. Ni1Hf showed the largest deviation from the parent spinel, with an expansion of 0.42 pm. If the size of Hf is considered and Hf is assumed to preferentially substitute the smaller $Al^{3+}$ cation (compared to $Ni^{2+}$), the maximum expansion for 1 wt. % doping is about 0.01% of the lattice parameter. This value would be smaller if the $Ni^{2+}$ was substituted with the $Hf^{4+}$. It is reasonable to assume that some Hf could be either incorporated within the spinel structure or trapped at grain boundaries or other defects within the bulk. Following bulk phase diagrams, $HfO_2$ and $Al_2O_3$ do not form a solid-solution, rather a mixture of phases below 2100K.[193] However, detailed investigations by the Harmer group from Lehigh University using aberration-corrected TEM techniques identified $HfO_2$ solubility in polycrystalline $Al_2O_3$ at 1400°C is between 100 and 200 ppm, where $Hf^{4+}$ was found to fractionally cover the grain boundary.[113, 114] Modifying oxides and concurrent effects on the spinel structure are scarcely investigated within the literature, owing to the use of $\gamma$-$Al_2O_3$ as a support which has a controversial structure due to a high defect content and therefore poorly crystalline nature.[62] Üstündag et al. in two separate manuscripts systematically investigated $ZrO_2$ and other transition metal oxide additions to spinel, in which he and his coworkers elucidated the effects of the modifiers on the

reduction of the spinel, although mostly focused on microstructural effects for use in ceramic metal composites.[46, 103] Regardless, pure spinel phases with the desired modifying oxides were produced in this study, and will be evaluated further for stability under reduction conditions and microstructural continuity with $NiAl_2O_4$ + 2.5 wt. % $ZrO_2$.

### 2. High Temperature X-ray Diffraction – Reduction Stability

Each of the compositions was examined for reduction stability under 4% $H_2/N_2$ by *in-situ* HTXRD following the same experimental setup as the $ZrO_2$ modified parent oxide in the previous section. Patterns obtained at room temperature after reduction are shown in Figure 32. Only one metastable defect spinel, $NiAl_{32}O_{49}$, is provided for clarity, as patterns are only slightly shifted among other metastable spinel compositions. Retention of the CCP oxygen sublattice, indicated by the absence of $\theta$- and $\alpha$-$Al_2O_3$, was checked for each composition. The Ni1Ti composition is different; this particular composition is known to mineralize $\alpha$-$Al_2O_3$[46, 72] and included as a reference for corundum formation.

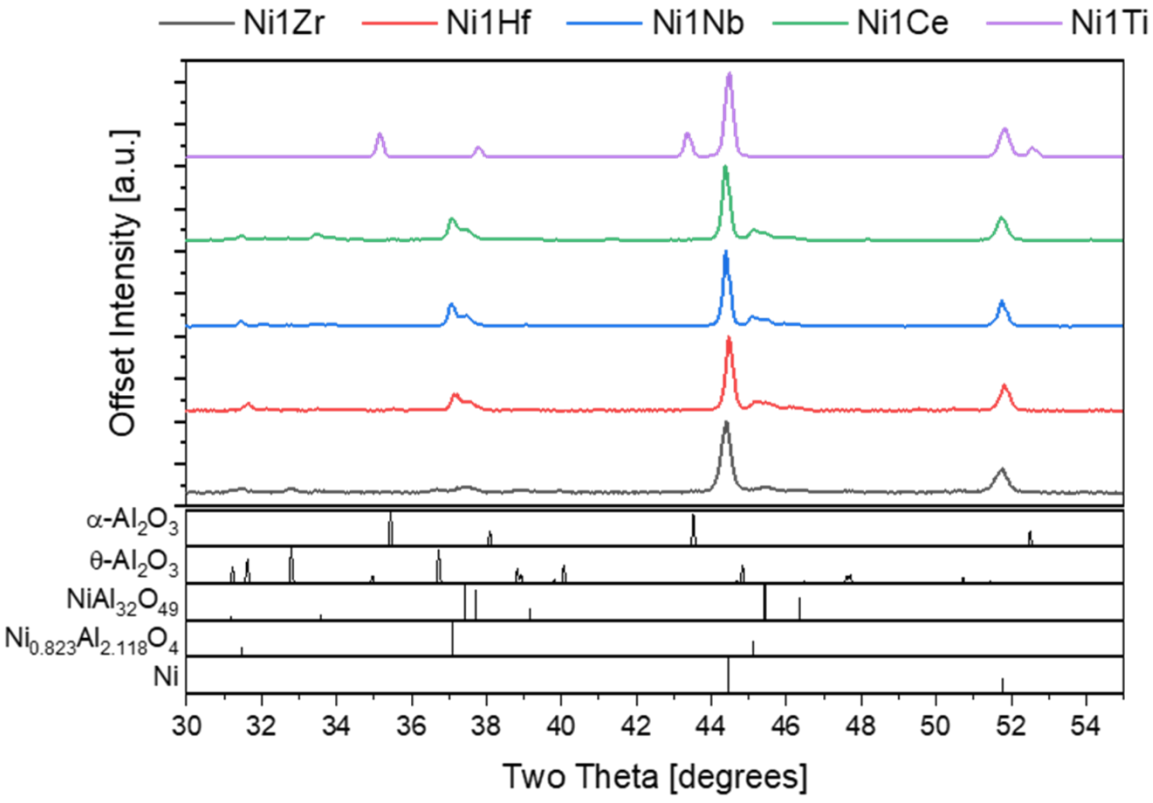


**Figure 32: XRD patterns upon cooling from HTXRD under flowing 4% $H_2$. Stick patterns are provided for reference as mentioned in the text. Nb modified patterns are identical over the provided range, therefore only one is provided for clarity. $NiAl_{32}O_{49}$ is an XRD pattern for a metastable spinel, while $Ni_{0.823}Al_{2.118}O_4$ is for reduced spinel.**

Ni1Hf after reduction exhibits no $\theta$- or $\alpha$-$Al_2O_3$ formation. To the author's knowledge, no data are available on the reduction stability of the Ni1Hf composition, or any other compositions examined below. Notable work directly analogous to spinel via $HfO_2$ doped polycrystalline $\alpha$-$Al_2O_3$ reveals that oxygen transport is reduced by a factor of 8 at 1400°C and is dependent upon the dopant concentration, up to 500ppm.[113, 114] A blocking model originally proposed by Saxton[194] was used to describe the grain boundary coverage of $Hf^{4+}$, which obstructs diffusion pathways along this route. This is comparable to Hf additions slowing oxygen kinetics in NiAl and Fe based superalloys, where the oxidation can be retarded by a factor of 10.[110-112] $HfO_2$ additions delayed the onset of transition alumina, i.e. massive loss of oxygen from the spinel lattice. Oxygen transport from the spinel to the external atmosphere is slowed to such a rate that oxygen loss is not catastrophic, and the CCP nature of the oxygen sublattice is retained, making the Ni1Hf sample a viable candidate to study for enhanced mass transport. At the same temperature, undoped samples lose more oxygen due to normal transport rates, massive oxygen loss occurs, and a phase transition to $\theta$-$Al_2O_3$ occurs which will eventually transition to $\alpha$-$Al_2O_3$ given enough time and temperature.

$CeO_2$ additions to the spinel yielded similar results to the Ni1Hf composition; no detrimental oxygen loss occurred to the spinel resulting in the absence of $\theta$- or $\alpha$-$Al_2O_3$ phases. Ni metal, defective and metastable spinel ($Ni_{0.823}Al_{2.118}O_4$ and $NiAl_{10}O_{16}$, respectively), and a $CeAlO_3$ perovskite are present at the maximum temperature and again at room temperature. Reduction of $Ce^{4+}$ to $Ce^{3+}$ results in the formation of $Ce_2O_3$, which ultimately reacts with the $\gamma$-$Al_2O_3$ to form a perovskite. Available phase diagrams from 1000°C to 2400°C of $Ce_2O_3$ and $Al_2O_3$ in the Ce deficient region show a solid solution of $Al_2O_3$ and $CeAlO_3$ forming,[195] which is observed in the HTXRD data. The advent of perovskite within the phase composition decelerated the formation of $\theta$- or $\alpha$-$Al_2O_3$; however, phase changes involving spinel components are undesirable as the loss of essential constituents may affect the parent spinel regenerability.

Two samples doped with Nb, Ni1Nb-WC600 and NbNi1-WC1000, had similar products post-reduction save the modifier composition. For clarity, only one pattern is provided in Figure 32, as the patterns are identical over the range provided. Ni metal and metastable spinel phases of $Ni_{0.823}Al_{2.118}O_4$, $NiAl_{10}O_{16,}$ and $NiAl_{32}O_{49}$ are present once

reduction commences. Ni1Nb-WC600 has an ending modifier phase of $Nb_2O_5$, whereas Ni1Nb-WC1000 did not have an identifiable Nb phase present. $AlNbO_4$ is a possible phase match; however, major reflections overlap with metastable spinel peaks, and minor peaks could not be identified due to a high signal to noise ratio. $AlNbO_4$ formation is favored in the $Al_2O_3$ rich region of the phase diagram under 1400 K,[196] which is below the operating temperature of the $H_2$ – HTXRD experiment (1100°C = 1373K). Oddly, $Nb_2O_5$ persists throughout the Ni1Nb-WC600 patterns with little change but would be expected to react with the excess $\gamma$-$Al_2O_3$ produced from reduction. Nb has been found to be incorporated into the spinel structure at low doping levels (around 2 mol% Nb), where higher doping (6 and 10 mol%) levels precipitated $NiNb_2O_6$.[116] With Ni extraction to the metallic state, the $Nb_2O_5$ may be forced from the $NiNb_2O_6$ structure into an oxide before $AlNbO_4$ can be formed. $NiNb_2O_6$ has a small phase field (≈±2.5 mol%) centered about 1:1 $Nb_2O_5$ and NiO compositions at 1200°C,[197] indicating that the phase field is much smaller at lower temperatures, eventually becoming a line compound or a solid-solution of the end members. Regardless of the phase composition, Nb doping hindered corundum formation, making the compositions viable candidates for evaluation of enhanced mass transport.

### 3. Scanning Electron Microscopy

Modified spinels that were found to be stable under extensive reduction conditions in the HTXRD were examined in the SEM for microstructural consistency with the $ZrO_2$ modified sample before reduction. Many of the modifier particles are difficult to discern from the spinel matrix, therefore BSE instead of SE signal was used to observe particles. Modifier particle morphology was examined as well as the retention of spinel facets which are integral to the activity and stability of the catalyst. Identical morphology to the $ZrO_2$ samples as previously mentioned is ideal. All samples exhibited prototypical faceting of the spinel oxide, with {111} triangular faces and shallow facets; therefore, modifying particle morphology will be evaluated. Figure 33 shows representative morphologies for all modifying oxides supported on spinel.

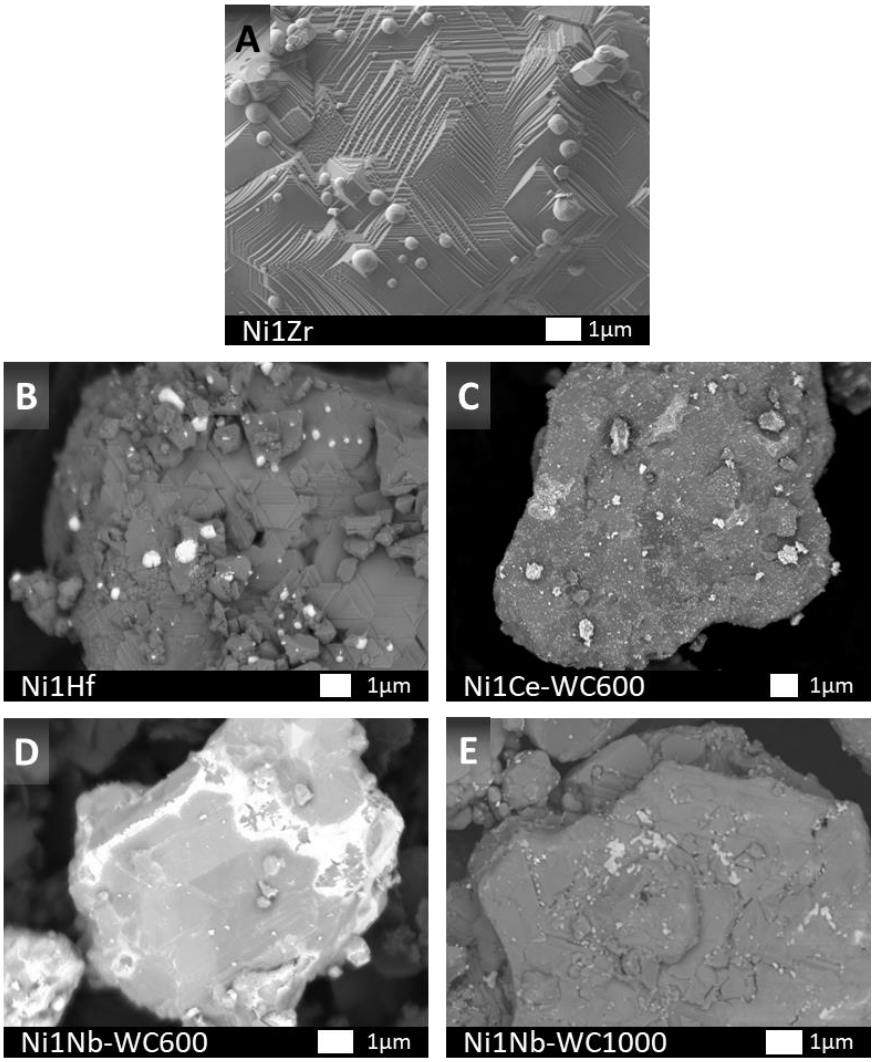


**Figure 33: SEM images (A in SE, B-E in BSE) of as prepared $NiAl_2O_4$ + 2.5 wt.% modifier, where A – $ZrO_2$, B – $HfO_2$, C – $CeO_2$, D – $Nb_2O_5$, and E – $NiNb_2O_6$.**

Spinel modified with 2.5 wt.% $HfO_2$ exhibited the least dissimilar microstructure to the $ZrO_2$ modified sample. Large bulbous $HfO_2$ particles litter the surface randomly, ranging from 100-1000nm in size with subtle modifier faceting. Spinel faceting is not as prominent as the $ZrO_2$ modified case but is still apparent.

$CeO_2$ modified spinel exhibited discrete nanoparticles decorating the entire outer surfaces, with concentrated areas of agglomerated nanoparticles.

$Nb_2O_5$ modified samples (Ni1Nb-WC600) exhibited a crust-like coating around the spinel, concentrated along facet steps and terraces. The synthesis temperature of the wash coating (600°C) was most likely too low for diffusion of Ce, Nb and O to occur on a

reasonable timescale, therefore no large defined particles were observed. $NiNb_2O_6$ modified spinel (Ni1Nb-WC1000) had prototypical spinel faceting with the modifying phase segregated to the facet edges in agglomerates ranging from 100 to 500nm, however, were not of similar morphology to $ZrO_2$ or $HfO_2$, presumably due to the differences in the crystal structure. Because of their dissimilar morphology to Ni1Zr and Ni1Hf, the Ce and Nb modified materials were not pursued further.

## E. Investigation of the Tunneling Phenomenon on Modified Spinel

As introduced in Section A and shown in the previous sections, spinel has been shown to exhibit extraordinary surface and mass transport properties at relevant service temperatures and pressures, via HTSEM and HTXRD. A novel modifier tunneling phenomenon which is thought to be driven by transport at the spinel-modifier interface has been discovered and has not been previously reported. The tunneling culminates visually as the modifying oxide seemingly burrows into the spinel support, shown in Figure 34. In the previous sections, systematic evaluation of the support and modifier chemistry identified compositional candidates.

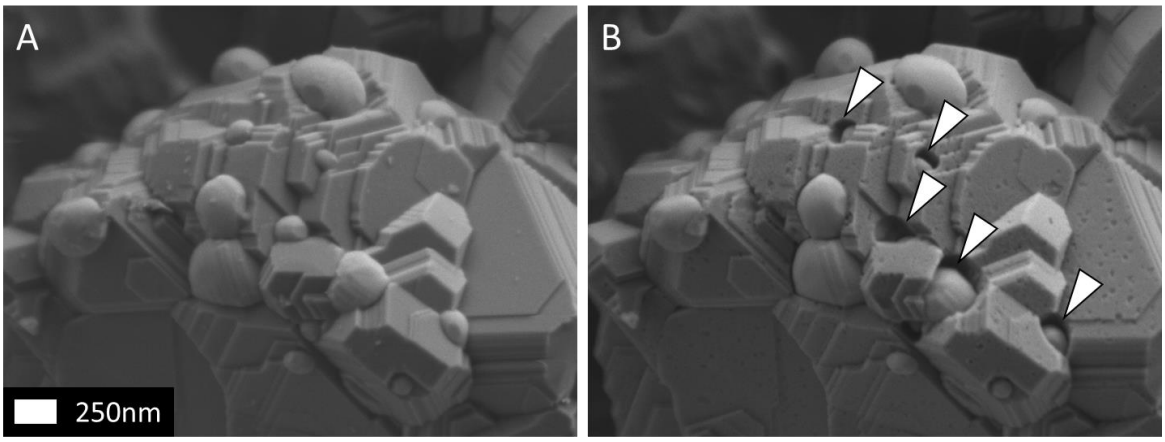


**Figure 34: $NiAl_2O_4$ + 2.5 wt.% $ZrO_2$ before (A) and after (B) tunneling observed *in-situ* at a maximum temperature of 1150°C, $p_{O_2} \approx 2 \cdot 10^{-10}$ atm. Arrows in (B) indicate tunneled $ZrO_2$.**

The following sections will address:

1. Evaluation of diffusional mass transport required to accommodate tunneling at various temperatures to obtain phenomenological tunneling rates and activation energies ($E_a$).
2. Comparison of calculated $E_a$ and tunneling rates to the literature values for bulk, grain boundary, and surface diffusion in spinel.

Model catalyst $NiAl_2O_4$ + 2.5 wt.% $ZrO_2$ and other $ZrO_2$ modified compositions of $Ni_{0.5}Mg_{0.5}Al_2O_4$, $Ni_{0.375}Co_{0.375}Mg_{0.25}Al_2O_4$, $MgAl_2O_4$ as well as $NiAl_2O_4$ + 2.5 wt.% $HfO_2$ were identified as candidates to examine via HTSEM for the tunneling phenomenon.

### 1. High Temperature Scanning Electron Microscopy and Empirical Evaluation of Diffusion and Activation Energy

Tunneling occurs on all tested Ni bearing samples, regardless of support or modifier composition, while $MgAl_2O_4$ does not exhibit the phenomenon at temperatures up to 1200°C. The bulbous modifier particle readily tunnels into the supporting oxide at temperatures ≥1000°C, shown in Figure 35 for $Ni_{0.375}Co_{0.375}Mg_{0.25}Al_2O_4$ + 2.5 wt.% $ZrO_2$. Tunneling occurs in the same fashion on all Ni bearing samples. All compositions with Ni exhibit similar features; however, the onset temperature varies with both support and modifier composition, summarized in Table IX. All rates were observed under electron beam irradiation unless noted otherwise. When the whole beam is placed on the modifying particle, tunneling rates increase as compared to lower magnifications, indicating a beam/thermal interaction is present, i.e. tunneling is not just heat induced by the temperature of the hot stage. Tunneling also occurs without electron irradiation, evidenced by the Ni1Zr sample (Appendix A – pg.152). As temperature increases, tunnels seem to form more readily and at expedited rates, indicating that the mechanism is thermally activated. The tunneling phenomenon does not appear to be affected by gravity as the particles move toward the center of the support regardless of orientation. As the modifier particle moves inward, no apparent surface manifestations of mass diffusion develop, e.g. crater-like edge buildup. The surrounding facets and overall microstructure of the modifying particle remain unchanged by the tunneling process.

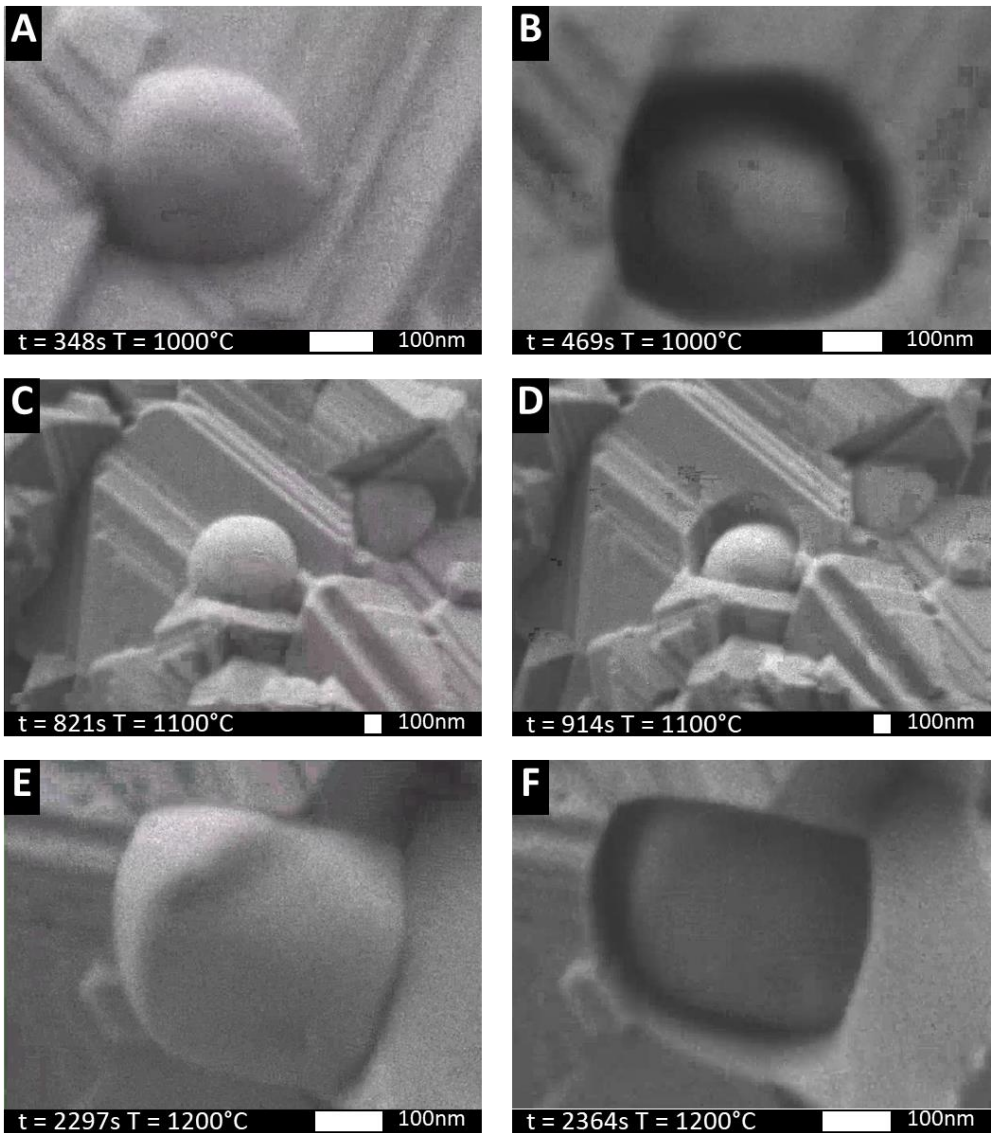


**Figure 35: Still images from HTSEM video on $Ni_{0.375}Co_{0.375}Mg_{0.25}Al_2O_4$ + 2.5 wt.% $ZrO_2$ at 1000°C (A – Before, B – After), 1100°C (C – Before, D – After) and 1200°C (E – Before, F – After) exhibiting $ZrO_2$ tunneling.**

**Table IX: Summary of compositions exhibiting tunneling, with onset temperature and reducible content.**

| Composition | Exhibits Tunneling | Onset Temperature [°C] | Reducible content per formula unit |
|---|---|---|---|
| $NiAl_2O_4$ + 2.5 wt. % $ZrO_2$ | Yes | 1000 | 1.00 |
| $Ni_{0.375}Co_{0.375}Mg_{0.25}Al_2O_4$ + 2.5 wt. % $ZrO_2$ | Yes | 1000 | 0.75 |
| $Ni_{0.5}Mg_{0.5}Al_2O_4$ + 2.5 wt. % $ZrO_2$ | Yes | 1100 | 0.5 |
| $MgAl_2O_4$ + 2.5 wt. % $ZrO_2$ | No | – | 0.0 |
| $NiAl_2O_4$ + 2.5 wt. % $HfO_2$ | Yes | 1200 | 1.00 |

Considered below are four possible mechanistic explanations for the tunneling phenomenon:

1. The modifying particle is shrinking, and the drilled tunnel is from the removed volume, where components are incorporated into the spinel (O can be lost to the vacuum as well).

2. Spinel is breaking down and components are being incorporated into the modifying oxide.

3. Spinel in contact with the modifier is breaking down, and all components are being lost to vacuum.

4. Spinel underneath modifier is diffusing away, where components diffuse along the modifier-spinel interface, up the tunnel wall, then along the reduction induced highly defective surface.

Visually, the modifying oxide does not change shape in the HTSEM experiments, as was further confirmed by focused ion beam milling (see pg. 105). In support of this observation, $Hf^{4+}$ and $Zr^{4+}$ dissolution into spinel is a possible mechanism for the tunneling, as both are of similar size in their respective configurations in comparison to $Ni^{2+}$ and $Al^{3+}$ as shown in Table X. It is understood that NiO and $Al_2O_3$ solubility in $ZrO_2$ is only a few

percent,[104, 139] whereas the solubility of $ZrO_2$ into transition alumina is much higher, ≈17 mol % in $\gamma$-$Al_2O_3$.[108] Since the solubility of NiO and $Al_2O_3$ is low in $ZrO_2$, dissolution of the spinel into the $ZrO_2$ is unlikely. $ZrO_2$ dissolution into the spinel is still possible, although as previously stated, Rietveld refinements were used to obtain m:t phase ratios of the $ZrO_2$ modifier at various dopant levels, where the spinel lattice parameter was invariant to the change in $ZrO_2$. Invariant spinel lattice parameter with increasing $ZrO_2$ content suggests that little to no substitution of $Zr^{4+}$ into the spinel lattice occurs during synthesis at 1500°C, and certainly not at 1200°C. If $Zr^{4+}$ substitution into the spinel was the case, increasing the total $Zr^{4+}$ content should have systematic increases in the lattice parameter (up to the solubility limit). Furthermore, defects in the form of metal vacancies must charge compensate for the $Zr^{4+}$ substitution onto metal sites for charge neutrality.

**Table X: Shannon's effective ionic radii of elements in $NiAl_2O_4$ + 2.5 wt.% modifier.[198] Ionic radii with a (*) denote typical coordination of inverse spinel.**

| Atom | Coordination | Ionic Radius [pm] |
|---|---|---|
| $Al^{3+}$ | Tetrahedral | **53*** |
| | Octahedral | **67.5*** |
| $Ni^{2+}$ | Tetrahedral | 69 |
| | Octahedral | **83*** |
| $Zr^{4+}$ | Tetrahedral | 73 |
| | Octahedral | 86 |
| $Hf^{4+}$ | Tetrahedral | 72 |
| | Octahedral | 85 |

All spinel used in this study has been synthesized at 1500°C which is well above the maximum HTSEM temperature of 1200°C. According to the Ellingham diagram for $NiAl_2O_4$ and the HTSEM $p_{O_2}$ of ≈$2 \cdot 10^{-10}$ atm. (Figure 27), the spinel is stable until ≈1175°C, at which point the spinel will start to break down into Ni metal, $O_2$(g), and $\gamma$-$Al_2O_3$, ruling out mass loss arguments at the onset temperature of tunneling. Mg additions to the spinel shift the free energy in a negative direction as Mg-MgO has a much larger $\Delta H_f$ than Ni-NiO, making Mg substitution more thermodynamically stable. Therefore, only at the maximum temperature of 1200°C should $NiAl_2O_4$ breakdown, where all other spinel compositions would be stable. $ZrO_2$ is used for refractory applications as it is stable at high temperatures over a range of pressures, also debunking $ZrO_2$ mass loss. Also, a phase transition from monoclinic to tetragonal occurs between 1050 and 1200°C, depending upon

$p_{O_2}$; lower $p_{O_2}$ (from $10^{-2}$ to $10^{-3}$) requires higher temperatures for transformation.[199-202] With the HTSEM $p_{O_2}$ at $2 \cdot 10^{-10}$ atm, a phase transition is unlikely to be the cause of tunneling at temperatures near 1000°C. It becomes clear from the previous arguments that $ZrO_2$ is not being incorporated into the spinel in any appreciable way, nor are $ZrO_2$ components being lost to vacuum.

Diffusion and not reactions must be considered to explain tunneling of $ZrO_2$ into the spinel. Bulk oxygen diffusion is extremely sluggish in stoichiometric spinel ($5 \cdot 10^{-18}$ $m^2s^{-1}$ at 1650 °C) due to the cubic close-packed oxygen sublattice and is 1-2 orders of magnitude faster for alumina rich defective spinel depending on composition.[33, 178, 179, 203] Cation and anion radionuclides bulk diffusion in spinel is much faster,[144, 145, 204, 205] with alumina rich defect spinel requiring lower diffusional activation energy.[30] Surface and grain boundary diffusion data is limited for the aluminate spinel family, but a few studies have investigated diffusion via radioactive isotopes and grain size measurements in these systems,[145, 205-208] showing that $D_{lattice} < D_{dislocation} < D_{GB} < D_{surface}$.

To relate the tunneling phenomenon to the literature diffusion data, the rate at which the modifier tunnels into the support must be quantified. A schematic (Figure 36) was constructed with physical measurements from the HTSEM experiments from before and after tunneling. Tunneling depths can easily be estimated via SEM with the correct orientation. It is assumed that the modifying oxide particles are spherical, with the largest cross-sectional area exposed (i.e. it is not akin to an iceberg in the ocean). With these assumptions, the radius of the particle can be estimated via SEM and the resulting modifier surface area in contact with the spinel can be calculated. Implied in the previous assumption, it is also postulated that the $ZrO_2$ is embedded within the spinel, where 50% of the total spherical surface area is in contact with the substrate. Knowing how much time it requires for the particle to sink can be extracted feasibly from the HTSEM videos, and a volumetric or a surface area rate can be calculated. Volumetric rates account for the volume of material being diffused away from the spinel-modifier interface per unit time, based on opening radius and tunnel depth. Surface area rates account for material at the spinel-modifier interface being diffused away per unit time. Both calculations give values reminiscent of diffusion coefficients, as the amount of mass being diffused over the spinel-

modifier interface every second can be calculated per unit area. Both methods were used in the following discussion.

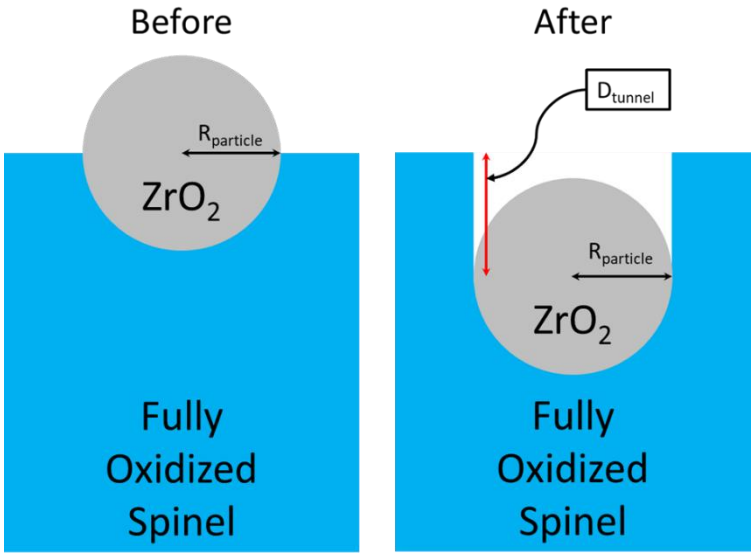


**Figure 36: Schematic of the tunneling phenomenon used to construct the model for rate calculations.**

Akin to diffusion, the temperature dependence of this tunneling phenomenon suggests that the mechanism is thermally activated, and evaluation at multiple temperatures can give information such as the activation energy. Equation (16) displays the Arrhenius-type equation,

$$A = A_o \cdot exp\left(\frac{E_a}{RT}\right) \tag{16}$$

where A represents the rate, $E_a$ is the activation energy, R is the gas constant, and T is temperature. $A_o$ is the relatively temperature independent pre-exponential factor, related to the jump distance, jump frequency, and entropy of migration.

It must be acknowledged that rates calculated are not classical diffusional rates, as the diffusing mass cannot be tracked accurately. The rates presented below are phenomenological by nature and are being compared to known diffusional rates in analogous systems based on the previous arguments.

Tunneling rates based on volume and surface areas were calculated for each composition according to the model as a function of temperature over the range of 1000-1200°C. Due to similar rates, only surface area derived values for this work are shown in

Figure 37. Diffusion values from the literature (Table XI) for spinel components are provided for context in Figure 37 as solid lines. Extrapolated values are represented with dashed lines. As mentioned previously, $D_{lattice} < D_{dislocation} < D_{GB} < D_{surface}$ and oxygen diffuses much more slowly than the cations, as evidenced by the literature data. The tunneling rates are expected to be similar to grain boundary diffusion or bulk diffusion in defective spinel, as both an interface and non-stoichiometry are present. We do not discount the influence of surface diffusion; however, the process is most likely dominated by either grain boundary or defective bulk diffusion.

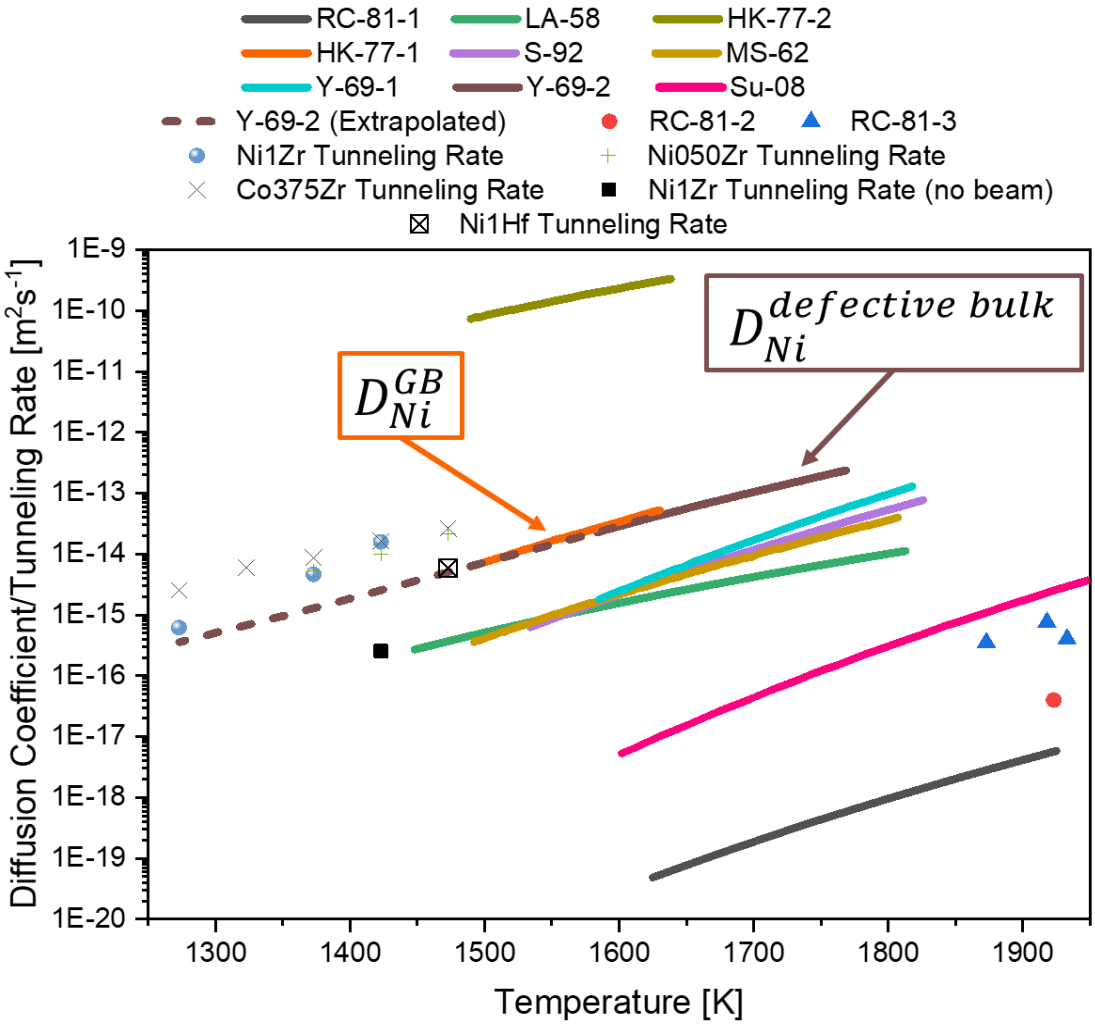


**Figure 37: Literature values for diffusion coefficients of $NiAl_2O_4$ components with calculated tunneling rates from this study. Diffusion specifics can be found in Table XI.**

**Table XI: Literature referenced for diffusional data. Abbreviations used in Figure 37 are provided. * - denotes data collected at non-ambient pressures.**

| Species | Type | System | Reference | Ref | Abbreviation |
|---|---|---|---|---|---|
| Oxygen | Bulk | $MgO{\cdot}Al_2O_3$ | Reddy and Cooper, 1981 | 33 | RC-81-1 |
| Oxygen | Bulk | $MgO{\cdot}1.8Al_2O_3$ | Reddy and Cooper, 1981 | 33 | RC-81-2 |
| Oxygen | Bulk | $MgO{\cdot}3.6Al_2O_3$ | Reddy and Cooper, 1981 | 33 | RC-81-3 |
| Ni | Bulk | $NiO{\cdot}Al_2O_3$ | Lindner and Åkerström, 1958 | 204 | LA-58 |
| Mg | Bulk | $MgO{\cdot}Al_2O_3$ | Sheng et al., 1992 | 209 | S-92 |
| Co | Bulk | $CoO{\cdot}Al_2O_3$ | Morkel and Schmalzried, 1962 | 210 | MS-62 |
| Cr-Al | Bulk | Natural $MgAl_2O_4$-$(Mg,Fe)(Cr,Al)_2O_4$ | Suzuki et al., 2008 | 211* | Su-08 |
| Ni | Bulk | $MgO{\cdot}Al_2O_3$ | Yamaguchi et al, 1969 | 30 | Y-69-1 |
| Ni | Bulk | $MgO{\cdot}1.5Al_2O_3$ | Yamaguchi et al, 1969 | 30 | Y-69-2 |
| Ni | GB | $NiO{\cdot}Al_2O_3$ | Hirota and Komatsu, 1977 | 145 | HK-77-1 |
| Ni | Surface | $NiO{\cdot}Al_2O_3$ | Hirota and Komatsu, 1977 | 145 | HK-77-2 |

For all compositions, tunneling rates are within one order of magnitude of extrapolated Ni diffusion in highly defective alumina rich $MgAl_2O_4$ and for Ni grain boundary diffusion in $NiO$-$Al_2O_3$ diffusion couples, as expected. Since all samples undergo some reduction, by either *ex-situ* or *in-situ* routes, some residual defect content is assumed to be present upon regeneration at low temperatures. Since defects govern transport properties, it is logical to assume that the tunneling rate should be comparable to the diffusion observed in defective systems. Albeit, tunneling rates are consistently higher than the extrapolated bulk diffusion in defective spinel, indicating other contributions to the transport, such as diffusion along grain boundaries, dislocations, or surfaces. It is of note that all diffusion studies discussed from the literature do not have modifying oxides present. Interestingly, the rate calculated without the beam for the Ni1Zr composition

resembles typical cation diffusion in stoichiometric spinel thus supporting the idea that a rather traditional diffusional process is the mechanism of transport.

Plotting ln(A) vs. 1/T (Figure 38), $E_a$ values for each composition can be extracted by multiplying the slope by the gas constant. Tunneling onset temperatures are sensitive to both spinel and modifier composition, as demonstrated by tunneling occurring on each variation at differing temperatures. Variance in the onset temperature highlights the complex interplay between the support's ability to accommodate defects, structural changes with Mg additions, and the modifier composition. Mg additions to the spinel as well as the substitution of $HfO_2$ for $ZrO_2$ shift the tunneling onset to higher temperatures. An exception arises when considering the $Ni_{0.375}Co_{0.375}Mg_{0.25}Al_2O_4$ spinel, where the onset temperature is identical to $NiAl_2O_4$. This result is not unexpected, as analogous $Ni_{0.75}Mg_{0.25}Al_2O_4$ showed expedited reduction kinetics in previous studies.[72, 212] $E_a$ and tunneling onset temperatures are provided in Table XII, along with selected $E_a$ from the literature. All measured $R^2$ values for this work are 0.99. Although volumetric and surface area rate calculations are inherently different, the produced activation energies are nearly identical. $Ni_{0.375}Co_{0.375}Mg_{0.25}Al_2O_4$ spinel has the fastest rates as well as the lowest activation energy consistently of all compositions.

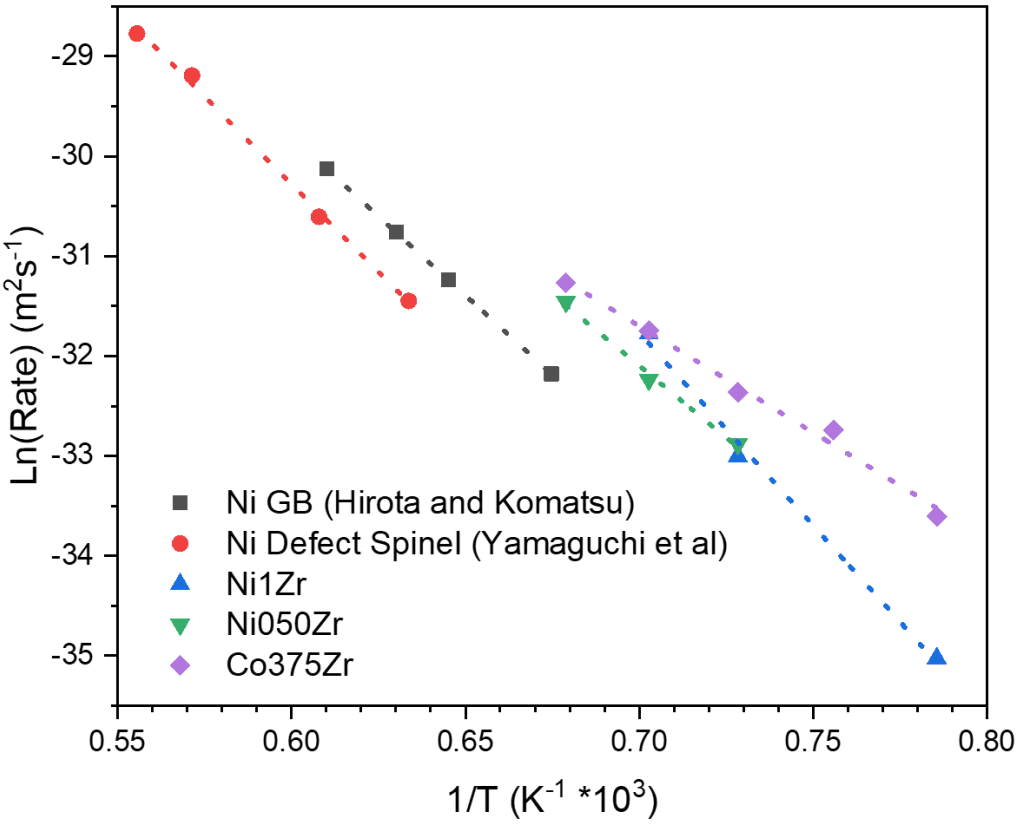


**Figure 38: Arrhenius plots of observed tunneling rates and literature diffusion coefficients. Dotted lines represent the linear fits for the respective data. All $R^2$ values from measured data are 0.99.**

**Table XII: Selected $E_a$ values from diffusion literature references and $E_a$ derived from tunneling rates. Onset temperature values are only provided for the current work.**

| Sample | Reference | $E_a$ [kJ·mol$^{-1}$] | $E_a$ [eV] | Onset Temperature [°C] |
|---|---|---|---|---|
| $Ni_{bulk} – MgAl_2O_4$ | [30] | 444 | 4.60 | - |
| $O_{Bulk} – MgAl_2O_4$ | [33] | 415 | 4.55 | - |
| $Co_{bulk} – CoAl_2O_4$ | [210] | 356 | 3.69 | - |
| $Mg_{bulk} – MgAl_2O_4$ | [209] | 343 | 3.56 | - |
| Ni1Zr | This work | 321 | 3.33 | 1000 |
| $Ni_{Bulk} – MgO·1.1Al_2O_3$ | [30] | 314 | 3.26 | - |
| $Ni_{GB}$ - $NiO·Al_2O_3$ | [145] | 264 | 2.74 | - |
| Ni050Zr | This work | 239 | 2.48 | 1100 |
| Co375Zr | This work | 177 | 1.83 | 1000 |
| Ni1Hf | This work | - | - | 1200 |

Rates and activation energies calculated for the tunneling mechanism closely resemble those of Ni bulk diffusion in defect spinel as observed by Yamaguchi et al.[30] and of Ni grain boundary diffusion in $NiO$-$Al_2O_3$ diffusion couples,[145] where the former has systematically investigated the diffusion of Ni in increasingly defective spinel. By considering the non-linear dependence of $D_{Fe\text{-}Mg}$ with oxygen content in $MgAl_2O_4$ and the change from a vacancy to an interstitial mechanism, Vogt et al. were able to reproduce all diffusion datasets with a point defect thermodynamic model, demonstrating $p_{O_2}$ considerations must be taken into account when comparing diffusion data in spinel.[213] Observed tunneling rates match this treatment well, given the base pressure of the SEM and operation temperature. Defects are known to increase diffusional rates and lower activation energy by providing vacant sites that do not need to be formed during heating.[30, 178] Yamaguchi et al. found that by introducing defects on the cation sites (0.75-3 cation site

%) the activation energy for diffusion could be lowered by 130 to 165 kJ/mol and was relatively constant with increasing defect content. This suggests that non-stoichiometry induced defects greatly affect mass transport. It is assumed that the regenerated $NiAl_2O_4$ spinel in this work has some finite number of defects, and the activation energies found by Yamaguchi et al. match remarkably well with the measured $E_a$ for tunneling (314 and 321 kJ/mol, respectively).[30]

As Mg is added to the spinel up to 50% on the A-site, the activation energy decreases up to ≈45% for the tunneling processes, which is unexpected as larger Ni content allows the structure to accommodate more defects. Therefore, Mg additions must to some extent alter the mechanism associated with tunneling. As noted by the geological community, small additions of impurities (i.e. 1 at% $Fe^{2+}$ in $MgAl_2O_4$) account for shifts in diffusional activation energy.[204, 209, 213, 214] $ZrO_2$ tunneling into $Ni_{0.5}Mg_{0.5}Al_2O_4$ has an $E_a$ close (difference of 0.04 eV) to that for $Mg'_{Al}$-$V_{\ddot{M}g}$ diffusion while $Ni_{0.375}Co_{0.375}Mg_{0.25}Al_2O_4$ exhibits an activation identical to $E_a$ for $V_{Al}$ migration.[215] Cation vacancies have been found via DFT simulations to be predominant in the alumina rich defect spinel.[216] However, through *in-situ* neutron diffraction, our group found that the oxygen-sublattice expels oxygen vacancies to the surface upon reduction, while $Al^{3+}$ ions are redistributed to form the non-stoichiometric spinel that is similar to the $\gamma$-$Al_2O_3$ structure.[65] Recall that reduction occurred in all tunneling experiments to some extent, which most likely resulted in a defective spinel shell. This redistribution of $Al^{3+}$ ions near the surface may provide sufficient defective sites for the cations to diffuse via open sites within the lattice, as suggested by simulations previously discussed.

Tunnel walls and the exposed spinel surface are free surfaces, therefore rate-limiting diffusion will most likely occur in the form of bulk diffusion, in agreement with the similarities in rates for defective spinel as measured by Yamaguchi et al.[30] Grain boundaries are known to enhance oxygen diffusion, as evidenced by Oishi and Ando's work on single and polycrystalline $MgAl_2O_4$.[179] Even though the samples used in Yamaguchi's work were polycrystalline, negligible change in the diffusion coefficient was observed for both perfect and defective spinel. In the case of the samples used in this work, grain boundaries as well as reduction induced cracking may provide pathways for

expedited diffusion, however, bulk diffusion in defect spinel is expected to be rate-determining.

A scarce amount of literature is present for $ZrO_2$ modified spinel, let alone diffusion along the spinel-$ZrO_2$ interface. $ZrO_2$, depending on the phase, can anisotropically strain the spinel matrix causing tensional and compressive strain by t-$ZrO_2$ and m-$ZrO_2$ respectively.[102] Chang et al. studying the NiO-$Al_2O_3$-$ZrO_2$ system found that enhanced diffusional grain growth occurred in alumina rich $NiAl_2O_4$–$ZrO_2$ compacts.[101] Highly dense samples prepared at modest temperatures by Üstündag et al. also suggested enhanced diffusion during sintering.[103] These reports provide little to no mechanistic explanation of the enhanced diffusional effects. Recently, dilatational lattice perturbations have been shown in perovskites to promote oxygen surface exchange and accelerated oxygen diffusion by modeling,[217] and experimentally in thin films[218] as well as bulk materials[219] for use as SOFC cathodes. If tensional perturbations are present in the spinel lattice from t-$ZrO_2$, the enhanced diffusion may be explained via the lowering of diffusional barriers of oxygen.

While convenient, a comparison of literature diffusion rates and activation energies to those for the effective diffusion calculated during tunneling can only draw qualitative conclusions. To better understand the phenomenon, more extensive characterization is needed, specifically at the spinel surface as well as the spinel-modifier interface. We therefore focus on the model case of $NiAl_2O_4$ + 2.5 wt.% $ZrO_2$ and employ focused ion beam milling to cross-section specimens for study of the ZrO2-spinel interface after tunneling.

## 2. Focused Ion Beam Milling & Direct Evidence of Diffusion Beneath $ZrO_2$ Particles

Investigation of the spinel-modifier interface is inherently difficult as the region of interest is beneath the $ZrO_2$ particle that tunnels into the bulk spinel grain, which is on the sub-micron scale. The only technique capable of milling on such a small scale is a dual-beam FIB. Since samples of the tunneling phenomenon are limited to a few spinel particles on a single high temperature SEM sample stage with varying orientation, only one or two spinel particles meet the geometrical requirements for FIB, resulting in an extremely restricted number of samples, and challenges in making the samples in the HTSEM,

moving them to the FIB and then again to the TEM. Meticulous sample preparation procedures must be used to ensure the sample is preserved well enough for analysis. Furthermore, sample milling is an arduous task, as $ZrO_2$ particles are smaller than 1µm. Due to these experimental constraints, only two samples of $NiAl_2O_4$ + 2.5wt.% $ZrO_2$ were analyzed.

A typical FIB cross-section of spinel is shown in Figure 39. To ensure stability during the milling process, a Pt coating was used to anchor the particle and preserve the surface (and near-surface) features. A through-the-lens BSE detector (TLD-BSE) was utilized to reduce image noise and enhance the contrast between the Pt coating and the $ZrO_2$ particle to image in the FIB. The $ZrO_2$ particle has tunneled into the support, as most if not all the modifier is sub-surface. Interestingly, features have formed beneath the modifier which seem to be voids, denoted by the dotted oval. Faint vertical lines underneath these features are attributed to gradients in the milling rate, which arise from changes in the sample hardness.

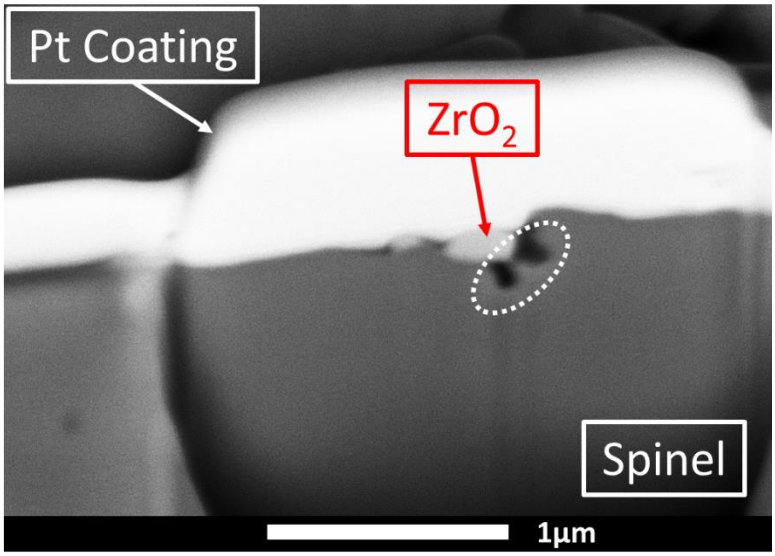


**Figure 39: TLD-BSE detector image of FIB cross-section of $NiAl_2O_4$ with tunneled $ZrO_2$ particle. Annotations are discussed in text.**

Features thought to be voids beneath the $ZrO_2$ are unexpected, as the reduced or regenerated spinel is expected to have no internal pores, as noted earlier from imaging cross sections of parent, reduced, and reoxidized spinel particles.[135] To further understand these

features, the reverse side of the particle also underwent FIB milling to expose the opposite side of the $ZrO_2$ particle. From initial SEM measurements, the modifying particle diameter was determined to be 230(11) nm orthogonal to the milling plane. Therefore, the milled thin foil must be less than the particle diameter to ensure the same particle is being analyzed. Figure 40A shows the vertical view of the foil, with B and C being the front and rear views, respectively. Foil thickness was measured to be 210(10) nm with the central feature being the $ZrO_2$ particle. Void-like features are below the particle on both front and reverse sides in differing locales, indicating that the feature is not uniform underneath the modifying particle. Figure 40C has been mirrored horizontally to highlight the varying position of the sub-modifier voids.

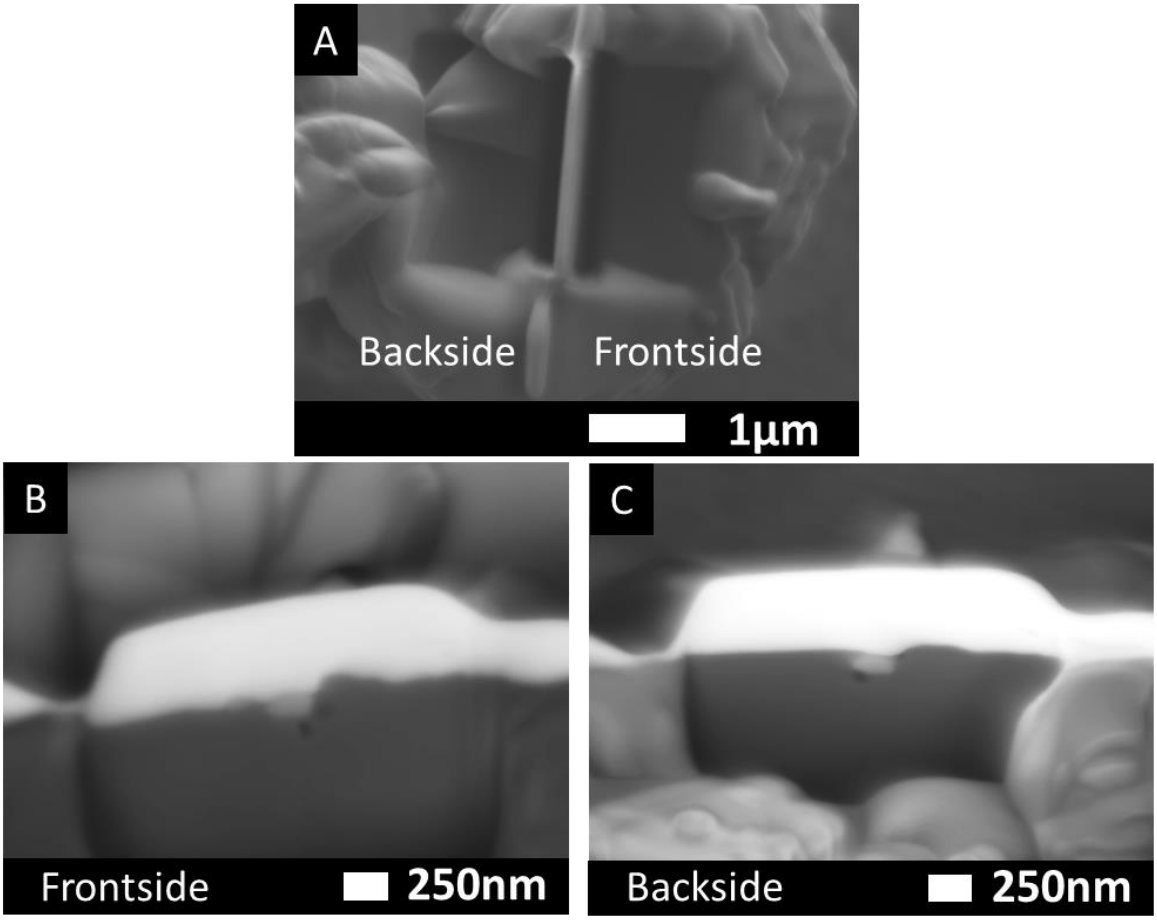


**Figure 40: BSE images of FIB thin foil of $NiAl_2O_4$ with a tunneled $ZrO_2$ particle from A – top view, B – Frontside view, and C – Backside view (image has been mirrored horizontally).**

EDS line scans on both front and reverse sides were used to determine if any compositional gradients were present, either across the voids or in the near-interface region. Figure 41 andFigure **42** show the line scan results for the front and back sides, respectively. Si and C are artifacts arising from the milling of the Protochips support, which are all constant and have been excluded from the line scans. Even though a milling artifact, Ga has been included as it may provide insight into voids and topological features induced by the milling process. No quantitative treatment of the data was utilized, as EDS is a semi-quantitative technique at best. Intensity is consistent between lines, indicating no concentration gradients are present within the error of EDS, as well as uniformity of the milled thin foil. Major features in the line scans occur on the leading side of the $ZrO_2$ particle, where an intensity increase is observed. The trailing side of the $ZrO_2$ also experiences slight intensity increases, but to a much less noticeable extent. Scans over the void like features exhibit the same intensity increase as interfaces with the $ZrO_2$.

Intensity variations observed around the supposed voids as well as the $ZrO_2$ are typical artifacts of interfacial intensity enhancement. X-ray emissions are increased as the interaction volume intersects with the interface, allowing for more characteristic X-rays to escape the sample. This phenomenon is akin to the effect of tilt in EDS. A dual-purpose Monte Carlo simulation program[220-224] was applied to reinforce the observation of enhanced signal, using physical parameters from the SEM. A schematic model and Al Kα X-ray interaction volumes are shown in Figure 43. Emission models verified that enhanced signal would be produced from the modifier-spinel interface as evidenced by the Al Kα (Figure 43D) observed in EDS line scans (Figure 41 and Figure **42**). Interestingly, for the accelerating potential of 5kV, simulated X-ray interaction volume depths for the embedded particle and pure spinel models are ≈200 nm, which is about the thickness of the thin foil from SEM measurements. For the void-spinel model, the interaction volume is larger than the lamella thickness (assuming a void of 100nm depth), which may account for the increased intensity observed in Figure 41 – 3, 4 as the line scan progresses over the void. The shallow void results in a larger overall interaction volume, as material is above and below where the incident beam meets the surface. It can be concluded that since the foil thickness and the simulated interaction volume depth are within 10s of nm or larger than the lamella, the signal is coming from the complete thickness of the foil.

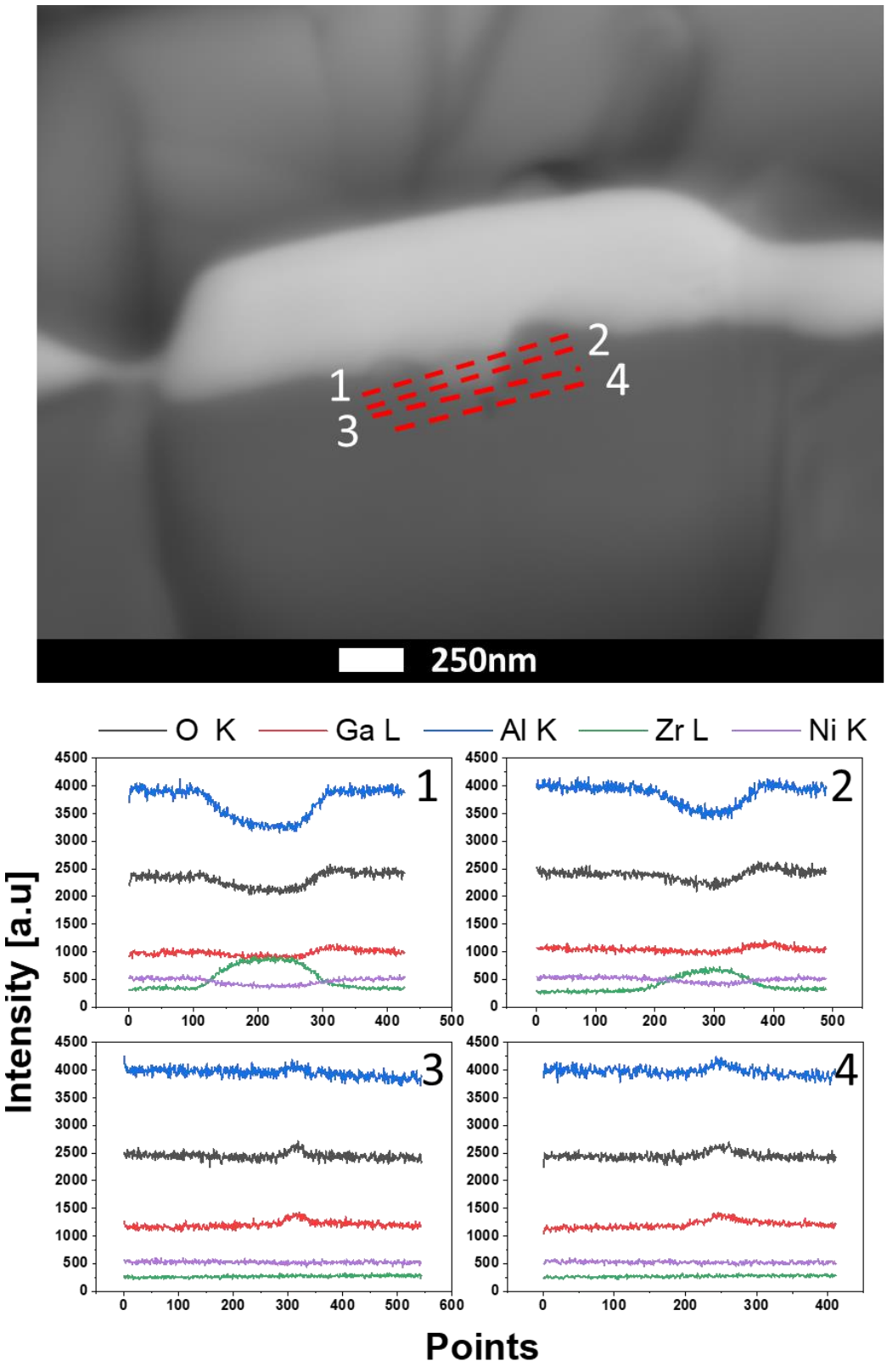


**Figure 41: SEM image of the frontside of FIB thin foil with EDS lines labeled 1-4, corresponding to the intensity plots derived from the EDS line scans.**

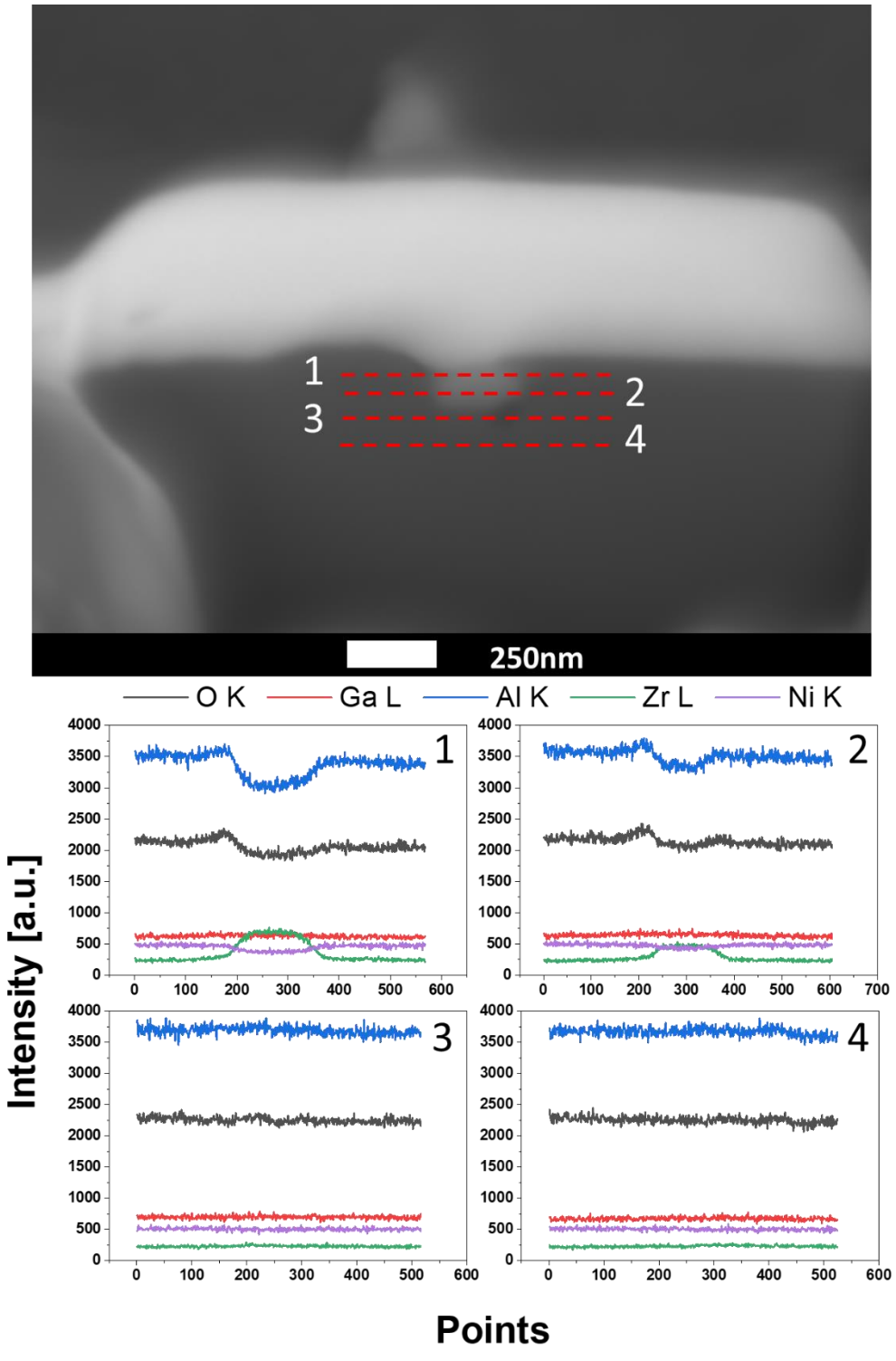


**Figure 42: SEM image of the backside of FIB thin foil (not mirrored) with EDS lines labeled 1-4, corresponding to the intensity plots derived from the EDS line scans.**

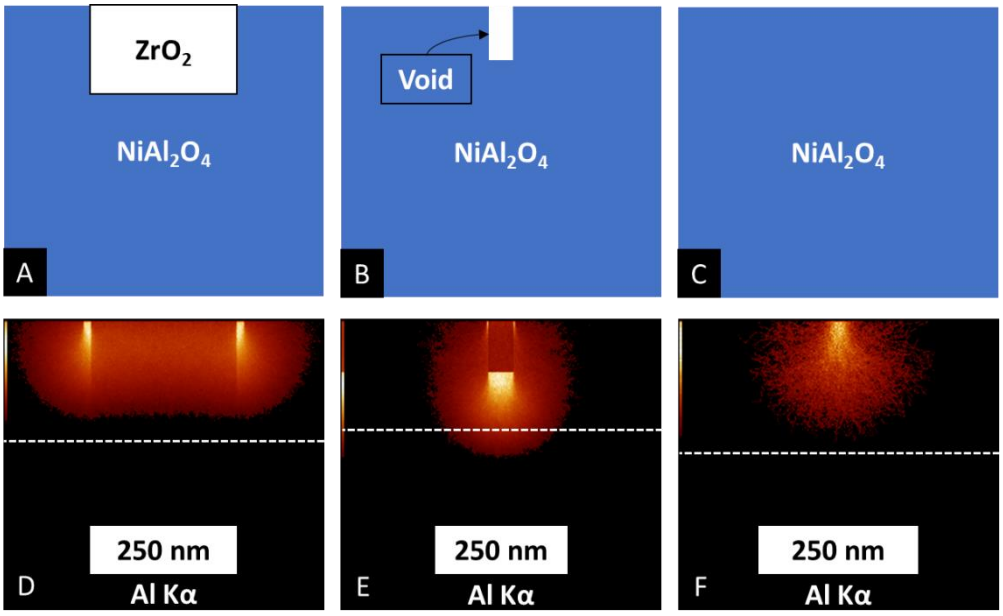


**Figure 43: Monte Carlo simulated interaction volumes for A – an embedded $ZrO_2$ particle in spinel, B – a void in spinel, and C – spinel, with the corresponding Al K$\alpha$ interaction volumes, D – F respectively. The dotted horizontal line represents the thickness of the FIB lamella.**

Bearing these results in mind, a sizable void either in width or depth would result in a decrease of the overall X-ray intensity. Probe size and lateral dimensions of the interaction volume as well as step size must also be considered, as a large interaction volume or step size may mask the feature, especially if small. This in fact may be the case for the line scans presented, as no intensity loss was measured over the void-like features as shown in Figure 42 – 3, 4. Small increases in Al and Ga signal are found for the trailing-edge of larger voids (Figure 41 – 3, 4), similar to the interfacial enhancement of the intensity as described before, however, no leading-edge increase is observed. Increased X-ray emissions on the trailing edge suggest based on the EDS detector geometry that the features are in fact voids, which the trailing edge is exposed to the detector as compared to the leading edge.

Ga deposited from the ion milling process tends to be implanted in the sample at constant concentrations due to the uniformity of the milling process. A caveat is that the sample is assumed to be compositionally uniform, where inhomogeneities tend to have either Ga deposited based upon material properties or lack thereof (i.e. a void). Some interfaces show slight uptakes in the Ga signal (for example, Figure 41 – 1 through 4)

which suggests that material near the void-like features has different mechanical and bonding properties than the surrounding area. Increases in oxygen and aluminum were also found at these interfaces; however, Ni was shown to remain constant. Interpretation of this leads to two possible explanations: milled Al and O atoms are redepositing at free surfaces, or there is indeed a concentration gradient. With the constant Ni intensity along the line, it is a more plausible assumption that the redeposition of lighter Al and O is occurring, which indicates that the structures are voids with free surfaces. These voids are not uniform around the $ZrO_2$, however may be continuous in 3D.

### 3. Scanning Transmission Electron Microscopy and Electron Energy Loss Spectroscopy

To investigate the spinel-zirconia interface on a more localized scale, STEM and EELS were conducted on a second FIB lamella. The sample is split into 3 distinct regions, the $ZrO_2$, an interfacial region, and the spinel as labeled in Figure 44. $ZrO_2$ exhibits well-ordered lattice fringes near the interfacial region, as denoted by the oval in Figure 44, whereas the spinel has no discernable order. The interface region (denoted as the area between the dotted lines) is large, ≈50nm, which the interface was not observed on the previous sample. However, the region is masked by bright particle-like features, which are concentrated at the interface but also appear on both spinel and $ZrO_2$. The appearance of these particles can be attributed to milling artifacts, most likely Pt or sample redeposition (recall that Pt is used as a protective layer in the FIB milling process). Point analysis for the Zr *L*-edge shows no diffusion of Zr into the bulk of the spinel.

EELS spectra shown in Figure 45 and Figure **46** are for the O *K*-edge and Ni *L*-edge, respectively. Locations of each measurement are marked as boxes in Figure 44, where each spectrum displayed is an average of 4 measurements, arranged in a 2x2 array. It is of note that most of the spectra within the literature are from samples which do not exactly match the processing parameters used in this study, where inversion, reduction, etc. may affect the local bonding as observed by EELS. All energies discussed have an error of ±0.5eV from the collection parameters.

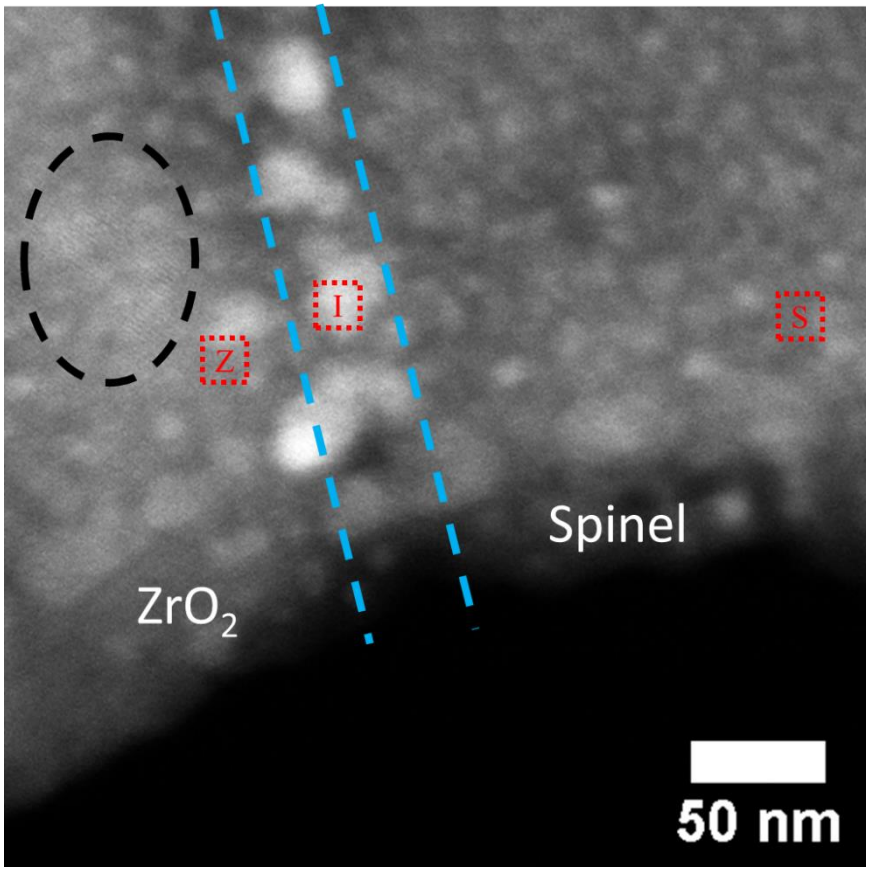


**Figure 44: STEM image of the region showing the $ZrO_2$-spinel interface. Regions and annotations are discussed in the text. Points are labeled as: S – $NiAl_2O_4$, I – Interface, and Z – $ZrO_2$ for EELS spectra (see following images).**

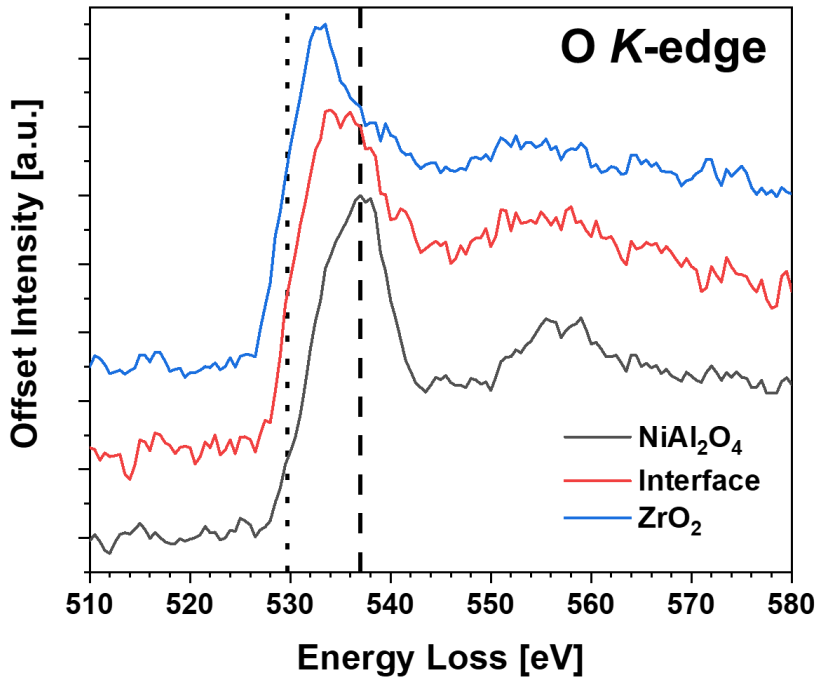


**Figure 45: EELS O *K*-edge spectra from points defined in Figure 44. Dotted lines are for reference.**

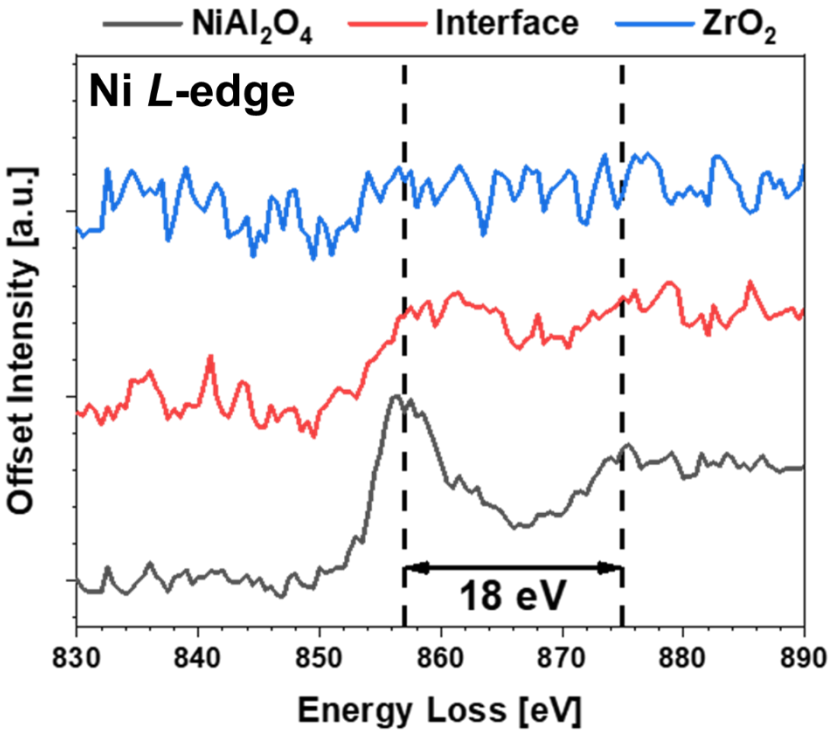


**Figure 46: EELS Ni *L*-edge spectra from points defined in Figure 44. Dotted lines are for reference.**

The onset and near-edge features of the O *K*-edge are sensitive to local bonding of the oxygen, which was used as a diagnostic to determine between the spinel and $ZrO_2$, as well as any oxygen deficiencies near the interface. The Ni *L*-edge is helpful to qualitatively determine if Ni concentration gradients are present in the spinel, as well as the transition to $ZrO_2$. As previously mentioned, Zr edges were not collected due to exceedingly long count times, which were not feasible during mapping due to sample drift and potential beam damage.

### a. Bulk Spinel Region

The general shape of the O *K*-edge spectrum of the spinel is in good agreement with the literature on $MgAl_2O_4$ and $NiAl_2O_4$.[225-228] The spectrum exhibits a main peak at an energy around 537eV (dashed line in Figure 45) preceded by two low energy shoulders at 534 and 530eV, and followed by near edge structure features. The minor shoulder around 530eV (dotted line in Figure 45) has been shown to be sensitive to spinel inversion,[225, 229] and in some cases has been shown to become a pre-edge peak. Shoulders observed at 534eV are indicative of hybridization of the O *2p* and Ni *3d* states.[230] The Ni $L_{2,3}$-edge spectrum measured in the spinel is typical for Ni containing spinel and Ni – $\alpha$-$Al_2O_3$ interfaces, with an 18eV separation of the $L_3$ and $L_2$ peaks.[228, 231]

### b. Bulk $ZrO_2$ Region

The spectrum taken on the $ZrO_2$ shows no Ni *L*-edge, as expected. The overall profile of the O K-edge resembles that of m- or t-$ZrO_2$. Distinction between m- and t-$ZrO_2$ relies on near-edge peak shape and intensity, which are broadened. The main peaks following the edge appear near 533eV and as a shoulder at 538eV, matching well with the literature separation values of 3.5-5eV which are dependent upon crystal structure.[232, 233] Broadening observed in the second peak has been observed with increasing stabilizer concentration, which can be attributed to inhomogeneities in the Zr and Y cation (and consequently, the point defect) distribution in YSZ via comparison of EELS and XANES measurements.[233] It can be concluded that the near interface region of the $ZrO_2$ has a modified cation distribution with no detectible Ni, which is most likely some defective analogue of the bulk $ZrO_2$.

### c. Interfacial Region

The interfacial region O *K*- and Ni *L*-edge spectra differ noticeably from the bulk spinel and $ZrO_2$ as described above. Ni intensity decreases noticeably and is barely discernable above the background, as only the absorption edge is clearly observed, matching previous work reporting Ni deficiency close to the $ZrO_2$-spinel interface.[103] The low energy shoulders (530 and 534eV) of the bulk spinel O *K*-edge spectrum grow in while the main peak in the spinel original position loses intensity, changing the overall peak positions and profile. Local inversion changes from Ni loss at the near-interface region may be drastically different from the bulk due to diffusional or modifying $ZrO_2$ effects, manifesting in the growth of the low energy shoulder and the loss of Ni signal. Near-edge and extended structural features broaden, indicative of nearest and next nearest neighbor coherence loss, i.e. reduction of the local oxygen site symmetry, agreeing with the loss of Ni intensity and possible inversion change at the interface. Interfacial O *K*-edge spectrum shape resembles previous EELS work on interfaces with corundum,[226, 227, 231] but, the asymmetric peak shape does not resemble the fairly symmetric $\alpha$-$Al_2O_3$ O *K*-edge.

Alternatively, if the EELS O *K*-edge spectrum of $\gamma$-$Al_2O_3$ is considered,[234-237] much better agreement is reached between the literature and our observed profile. It is of note that spectra from the literature are on commercial $\gamma$-$Al_2O_3$, whereas the present spectra are from a reduced sample with a structure akin to $\gamma$-$Al_2O_3$ which has been reoxidized in vacuum, where it is expected to retain point defects from the reduction process (see Raman Section pg. 55). Therefore, inversion changes brought on by Ni reduction during HTSEM observation may not be reversible, and a small amount of transition or higher alumina structure is retained, with an increasing concentration of point defects that shift the O *K*-edge spectra to lower energies. Regardless, it becomes clear from the data that the interface region has a reduced concentration of Ni and consequently local structure around the oxygen that resembles $\gamma$-$Al_2O_3$, which can be effectively be described as a defective spinel.

## F. Proposed Models for the Tunneling Phenomenon

It is worth at this point to recall all the evidence presented for the tunneling phenomenon, and any literature evidence to lead toward a possible mechanism, which is summarized as follows:

- ***Tunneling occurs with both $ZrO_2$ as well as $HfO_2$, with about the same rates. Similar rates are observed with changes in support chemistry, as long as some reducible content is present.***
- ***The interface between the $ZrO_2$ and spinel is Ni deficient, with oxygen bonding that resembles a defective spinel structure.***
- ***Non-homogeneously dispersed voids are observed beneath the tunneled $ZrO_2$.***
- ***Tunneling occurs without the electron beam and its rate is the same order of magnitude as bulk cation diffusion in spinel.***
- ***Tunneling rates with electron beam irradiation are expedited and are within an order of magnitude of $Ni^{2+}$ diffusion in defective $MgO{\cdot}xAl_2O_3$, or Ni grain boundary diffusion in $NiO$-$Al_2O_3$ diffusion couples.***
- ***$MgAl_2O_4$ does not exhibit tunneling, so the mechanism is clearly related to the defect structure that arises from selective removal of Ni and oxygen ions.***

Evidence of tunnels being formed within the literature are concentrated in the development of SiC technology, which have been referred to by a variety of synonyms such as micropipes, microtubing, microcapillaries, nanotubes, macrodefects etc. These types of features range from 20-250 nm in depth and vary from 10-20 nm in diameter. Many early investigations focused on giant screw dislocation theory, which is based on plate-like crystal growth,[238-241] while more recent work focuses on crystal length,[242] concentration gradients[243, 244] or kinetics at the surface.[245]

We now consider concentration gradients as well as surface kinetics in the following discussion. Surface diffusion along tunnel walls has been observed at defective sites in chemical vapor deposited $\beta$-SiC/Si interfaces during the carbonization process.[243, 244] From meticulous TEM investigations, Scholz and coworkers discerned that tunnels form into the surface by Si diffusion from the bottom of the tunnel, along the wall, to the top to react with the carbonizing atmosphere. Discontinuous Au decorated Si also exhibited ≈10nm diameter tunnel formation after brief exposure to a $H_2O$ + HF solution, where the tunnel wall was passivated with a diffused Au monolayer.[246] Both studies give credence to diffusion of atoms along the tunnel wall, which is analogous to surface diffusion.

Investigation of concentration gradients, diffusional kinetics, and their connection to voids inevitably leads to the Kirkendall Effect. Classically, the Kirkendall Effect as

observed in metallurgy is essentially where vacancy migration compensates for unequal diffusion of two or more constituents across an interface, moving the interface.[247-249] If this concept is applied to nanoscale systems where small constrained volumes and high surface areas are present, diffusion via pore surfaces is likely to be so fast that vacancy supersaturation can occur, resulting in void formation. Voids can then agglomerate together due to the confined space, effectively creating porous or even hollow nanostructures. This process, aptly dubbed the "Nanoscale Kirkendall Effect" (NKE),[250] has been harnessed to form nanostructures in many different alloy, chalcogenide, nitride, carbide, and oxide systems (see reviews [251, 252]). Hollow nanowires of spinel with the chemistry of $MgAl_2O_4$ and $ZnAl_2O_4$ have been formed by this process.[253, 254]

The overall principle of the NKE is described in detail elsewhere;[251, 255] here, a brief overview will be provided. A simple schematic is shown in Figure 47, where the flux is denoted as J for materials A and AB. It is assumed that $J_A > J_B$ and vacancies compensate the diffusion by precipitating voids near the interface, i.e. $J_A = J_B + J_V$. Furthermore, these small voids act as sinks for the inward flux of vacancies, and thus increase in volume. Once these voids grow to a considerable size, coalescence can occur, breaking the connection for bulk diffusion from material A, but also creating considerable surface for fast transport to occur, which lowers the activation energy as compared to bulk diffusion. The A material can then redistribute itself via fast diffusion along any surface or interface, where the process for B continues generating a continual vacancy flux toward A, growing the voids.

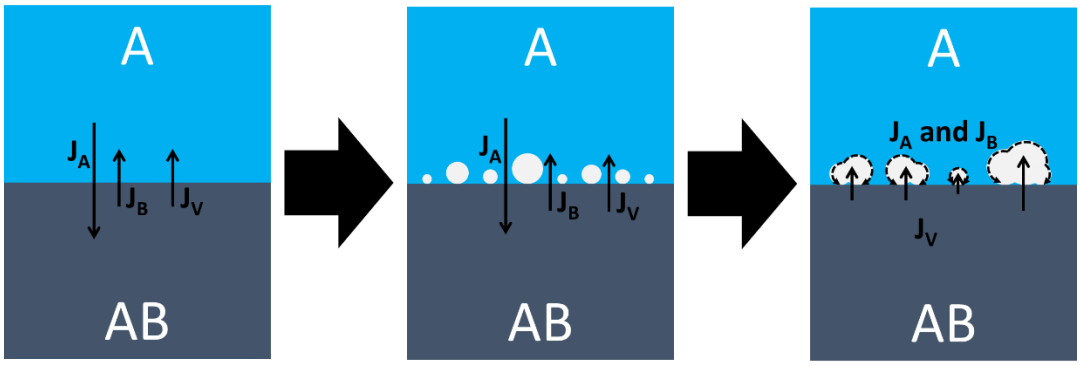


**Figure 47: General schematic of the Nanoscale Kirkendall Effect.**

The NKE explanation requires that both materials have at least one shared component, but in the spinel/$ZrO_2$ system, this is not the case. Due to the cubic close packed

oxygen sublattice of the spinel, bulk diffusion of oxygen occurs too slowly to be of importance. If oxygen diffusion was the cause, voids would be forming in/on the $ZrO_2$ according to the previous arguments, which is obviously not the case. Therefore, we consider cation diffusion in the spinel, as well as surface oxygen diffusion, specifically between the bulk, the (near) interface region, and along surfaces.

### 1. Potential Mechanistic Causes for the Tunneling Phenomenon

The hypothetical mechanisms by which the $ZrO_2$ modifier can tunnel into the spinel support *only* when it is defective (i.e. the effect is not observed on $MgAl_2O_4$) have been reduced to two, with only one general explanation being plausible based upon the evidence presented thus far. These two hypotheses are presented below in separate sections, with the former being the most likely explanation for the tunneling phenomenon.

#### a. Model Based on Enhanced Interfacial Diffusion Arguements

A model was conceived based on the notion that an interface is created between the modifier and the spinel, which can act as a short-circuit diffusion pathway from the bulk to the surface. An overall schematic of the likely process is shown in Figure 48.

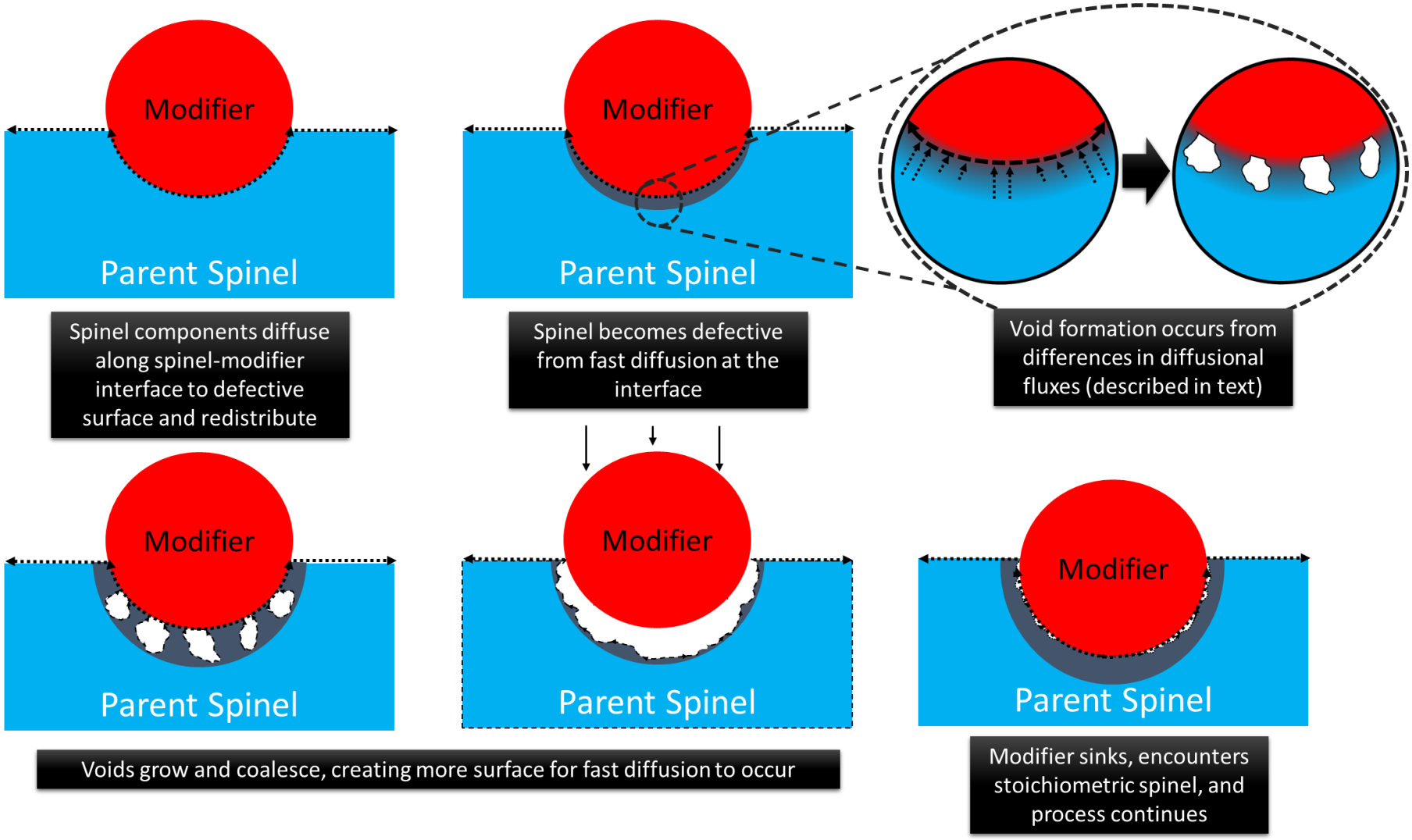


**Figure 48: Schematic of the tunneling process from enhanced interfacial diffusion.**

First it must be acknowledged that the interface is relatively discrete between the $ZrO_2$ and spinel, as evidenced by STEM, EELS, phase diagrams and solubility arguments discussed previously. Furthermore, diffusion along an interface is faster than typical bulk diffusion, as demonstrated by Hirota and Komatsu for NiO-$Al_2O_3$ diffusion couples.[145] It is then logical to assume that the spinel components beneath the modifier utilize this short-circuit diffusion pathway to reach the defective surface and redistribute to form a less defective spinel, which was shown in section B.3 from Raman spectroscopy for vacuum oxidized samples. As the diffusion of spinel components proceeds via the short-circuit interface pathway, the spinel in contact the modifier may become non-stoichiometric, which can facilitate diffusion of spinel components. Recall that formation of defective spinel at the interface was the conclusion of the STEM/EELS section discussed previously (Section E.3). Defective interfaces between $SrTiO_3$ and YSZ have been observed within the literature via STEM and EELS, showing an increased oxygen vacancy concentration by obvious changes in the O *K*-edge fine structure,[256] similar to this work.

It is pragmatic to consider a rational explanation for void formation in the spinel and beneath the modifier, in the confines of the enhanced interfacial diffusional model. Voids are likely to form from non-uniform diffusion from beneath the modifier, most probably in the form of faster diffusion in local areas beneath the modifier to the spinel-modifier interface. In the case of $ZrO_2$, the following must be considered for local changes in the diffusion coefficient of spinel components along the interface:

- The $ZrO_2$ is composed of dual monoclinic and tetragonal phases;
- The $ZrO_2$ is generally not spherical, and variations in surface texture in contact with the spinel may facilitate void formation;
- Directional diffusion of the underlying spinel grain, as it is expected to be a single crystal directly beneath the modifier (not an agglomeration of nanoscale grains), which will have some determination of the diffusional rate of spinel components.

All three effects may play some role, but to what extent is unknown. It can, however, be rationalized that the latter two points are more plausible than the dual phase argument. The introduction of the tetragonal phase of $ZrO_2$ has enhanced oxygen transport effects,[202] but its presence is speculated from room temperature XRD and SEM data. Furthermore, it is unknown, if both phases are present within the same particle, what is

their spatial arrangement, or if both phases are in contact with the underlying spinel under observation conditions.

Alternatively, modifying particle morphology is observed to remain constant throughout the HTSEM experiments, retaining the irregular bulbous morphology and slight faceting as described in Section B.4.a. The maximum experimental temperature of 1200°C is much below the roughening temperature for $ZrO_2$ ($¾ \cdot T_{Melt} = T_R = 2036°C$); therefore, little to no reconstruction is expected, leaving the initial microstructure of the modifier intact. The retained surface texture may have local influences on the diffusion to the spinel surface.

Akin to the interface texture of the $ZrO_2$ particle, the underlying spinel in the immediate vicinity of the modifier is most likely of a single crystal orientation (at maximum a few orientations), and not comprised of many nanoscale grains. Large grains are evidenced by the sharp Bragg reflections in the parent oxide (Figure 7), which have been previously measured to be about 450nm via the Rietveld method,[72] as compared to the relatively smaller size of the $ZrO_2$ particles. Therefore, it is expected that any grain boundary diffusion is negligible, and that bulk diffusion is the more likely cause for tunneling. The growth direction of the single crystal is also of importance. For example, the {111} planes in spinel are the oxygen close packed planes, in which oxygen diffusion is slowed significantly. It can be envisioned that pores are nucleated at locations where the fast cation diffusion directions for the spinel and $ZrO_2$ match, which the mass transport is faster than other mismatched areas beneath the modifier.

Whatever the actual mechanism, void formation occurs beneath the modifier. These voids are posited to grow and coalesce, allowing the modifier to incrementally burrow into the support as the space becomes available via enhanced interface diffusion to the defective spinel surface. Once the modifier and spinel are in contact again, the process can continue with fast interfacial diffusion, essentially perpetuating the tunneling process as observed in the HTSEM experiments.

### b. Model Based on Interfacial Lattice Strain Arguments

In general, tensile strain can be visualized as a stretching of the sample on a macro scale, or as the directional deformation of bonds on an atomic scale, assuming that the structural coherence is maintained (i.e. bonds do not break). As bonds are stretched, more space becomes available within the unit cells, as well as decreases in bond strength, allowing species to diffuse at reduced energies. It can be envisioned from these arguments that a stretched lattice would facilitate diffusion.

In alignment with the arguments presented in the previous paragraph, compressive and dilatational strain of a few percent on perovskite derived materials have been shown by simulations[257, 258] as well as experimentally[217-219, 256, 259] to modify bulk and surface oxygen transport. Tensile stressed $La_{1-x}Sr_xCoO_{3-\delta}$ model thin films fabricated by pulsed laser deposition were found by Kubicek et al. to have 10 times the oxygen diffusion as compared to compressed films.[218] Furthermore, they conclude that the acquired results on the effect of strain are consistent with stoichiometry changes, with higher diffusional values as the oxygen vacancy concentration (and consequently the amount of Sr) is increased. The previous results of tensile strain effects on perovskite materials can be extended to heterostructures, which present some lattice mismatch, as in our spinel-$ZrO_2$ system. Chang, Chen and Shen, as well as Üstündag et al., found using electron diffraction that stoichiometric and $Al_2O_3$-rich non-stoichiometric spinel in contact with both m- and t-$ZrO_2$ created compressional and dilatational lattice distortions near the interface, respectively.[100-103] The samples examined in the Üstündag et al. study were around the same size as the particles observed in this work, with nearly identical processing parameters.

It is worthwhile to discuss how localized areas of dilatational and compressional stresses may affect the tunneling phenomenon, in the confines of this model. Recall that the overall phase composition of the $ZrO_2$ on the spinel support is approximately equal parts of monoclinic and tetragonal phases. Figure 49 shows a $ZrO_2$ particle, comprised of mosaic-like vertical bands which are known to be twinning of the monoclinic phase, where twins arise from the presence of the tetragonal phase at high temperature.[105] If this case applies for all $ZrO_2$-spinel interfaces, then the underlying spinel may be in contact with both monoclinic and tetragonal $ZrO_2$ polymorphs at high temperature, and the lattice is locally under compression and tension, respectively.

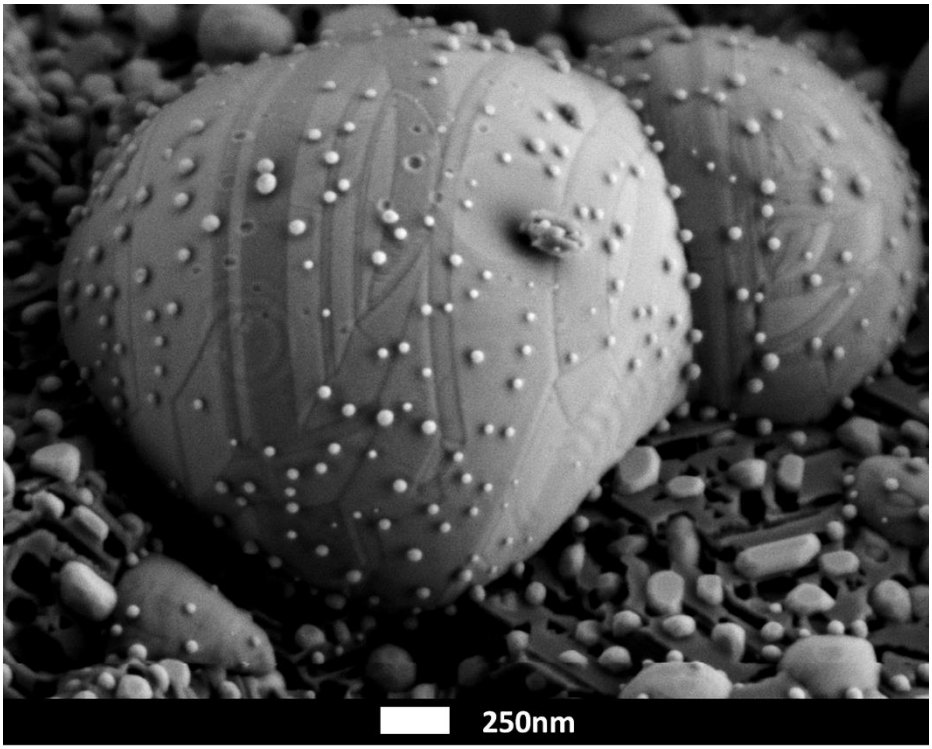


**Figure 49: SEM image of $ZrO_2$ particles on $NiAl_2O_4$ reduced at 1100°C in flowing 4% $H_2/N_2$ exhibiting vertical mosaic-like twinning bands.**

From the previous observations and arguments, a schematic shown in Figure 50 was constructed to demonstrate the progression of the Nanoscale Kirkendall process in this system if local stresses are the dominant driving force for tunneling. $ZrO_2$ is shown with bicolored bands to represent the monoclinic and tetragonal phases at high temperature. Dark regions underneath the $ZrO_2$ represent the dilatational strained spinel brought on by the t-$ZrO_2$ phase. First, the dilatational region exhibits enhanced diffusion from the lattice tension in the near t-$ZrO_2$ region of the spinel. Small void formation occurs in the second step, due to $D_{spinel}^{compressed} < D_{spinel}^{tension}$ (where, D α J), in which vacancy migration must account for the difference in fluxes. Vacancies are introduced by the slight reduction that the spinel undergoes in the microscope, evidenced by Ni particle exsolution during heating. Voids continue to grow and coalesce in the third step, creating more surface for expedited diffusion. In the fourth step, mobile cation constituents diffuse first from the compressed spinel due to their relatively fast diffusion coefficients (see Figure 37), while slowly diffusing atoms are left behind. Mobile cations can diffuse along the $ZrO_2$ surface or diffuse

to the void-spinel interface resulting in a defective spinel layer. Eventually, slowly diffusing atoms can move along the void surface and recombine with the non-stoichiometric spinel on the void wall, or diffuse along the $ZrO_2$ interface, up the tunnel wall, and finally redistribute at under coordinated features at the surface. Some of the newly grown spinel is still in contact with the t-$ZrO_2$, which most likely turns the spinel lattice into tension again, continuing the process.

If the assumption is made that void formation is a continuous process, voids may be posited to incrementally grow with extended time and temperature. Once these voids sufficiently widen and coalesce, the $ZrO_2$ can tunnel into the spinel as observed in the HTSEM videos, and shown schematically in Figure 51.

Naturally, the previous effects should occur on all spinel in contact with t-$ZrO_2$, even on the sides. The vertical alignment of the bands decreases the probability that the spinel-$ZrO_2$ interface is of mixed polymorphs, i.e. spinel is in contact with only the monoclinic or only the tetragonal polymorph on the sides. Additionally, the side of the $ZrO_2$ is continuously moving downward so is in contact with a new section of spinel, not imposing localized lattice compression or tension, unlike the bottom of the $ZrO_2$ which is continuously in contact with spinel. As mass must be diffusing from the bottom of the modifier for tunneling to occur, spinel components must be redistributed along tunnel walls or to the defective surface. One would expect that the structure resembles a defective spinel. This is supported by the EELS point analysis at the $ZrO_2$-spinel interface, where interfacial O *K*-edge spectra resembled that of $\gamma$-$Al_2O_3$, with a noticeable decrease in the Ni *L*-edge intensity as compared to the bulk spinel.

The literature provides a large body of work that identifies tensile strain to have a large impact on anion diffusion in oxide systems, specifically near interfaces. In our spinel-$ZrO_2$ system, the amount of $ZrO_2$ is small (only a few wt.%); however, mass transport around the $ZrO_2$ is amplified when heated, and certainly when heated and under electron irradiation. It is unclear if local stress perturbations have large or small effects on the tunneling phenomenon, as mass is diffused away from the interface, leaving underlying (and unperturbed) spinel in contact with the modifier. $ZrO_2$ would have to influence the underlying spinel into tension and compression after tunneling has initiated and mass has diffused away, which is unlikely. Therefore, lattice perturbations may play a role in the

initial stages of tunneling and may account for changes in the activation energy observed; however, it is unclear how the effect is perpetuated with the tunneling phenomenon.

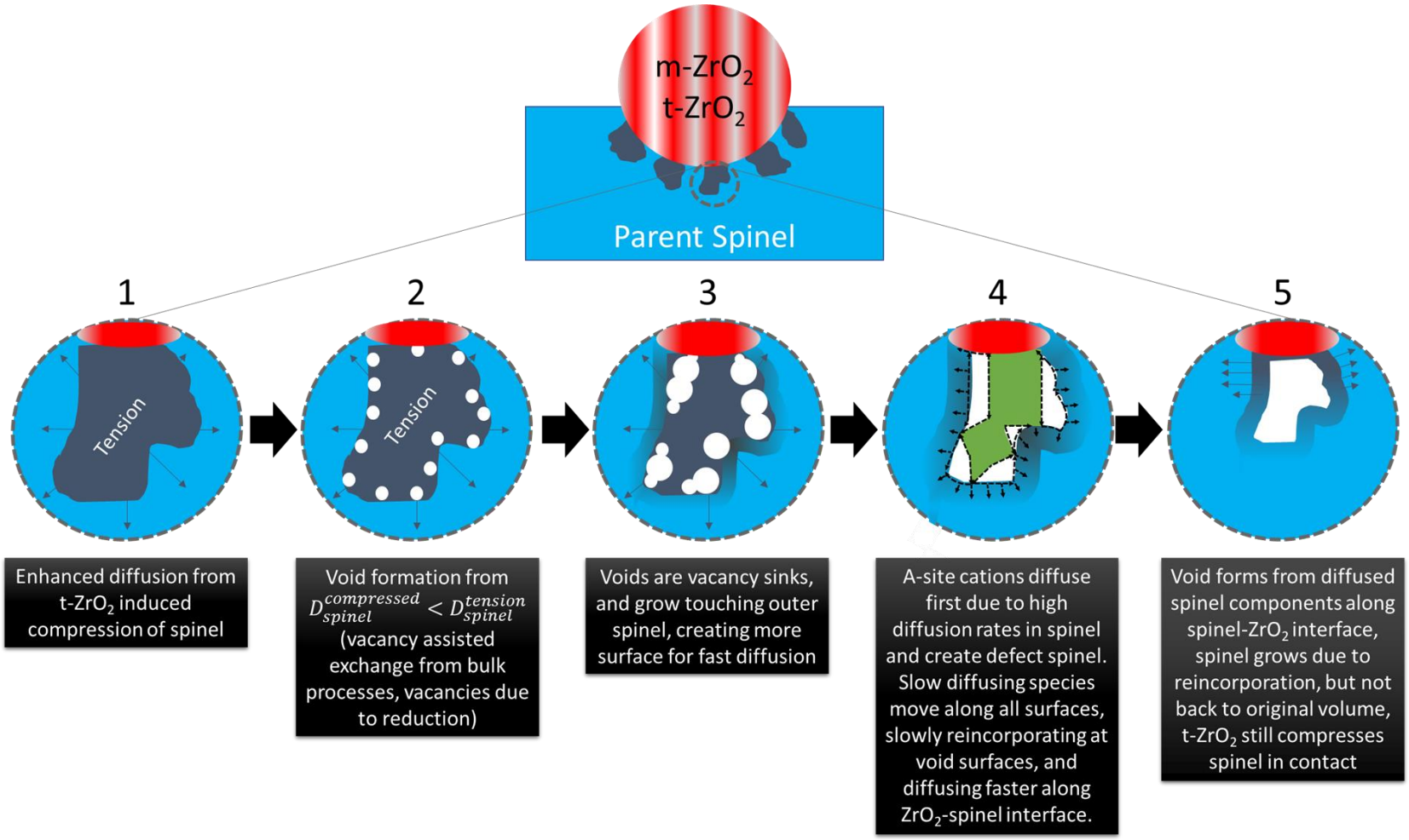


**Figure 50: Schematic of the Nanoscale Kirkendall Process and progression steps to void formation.**

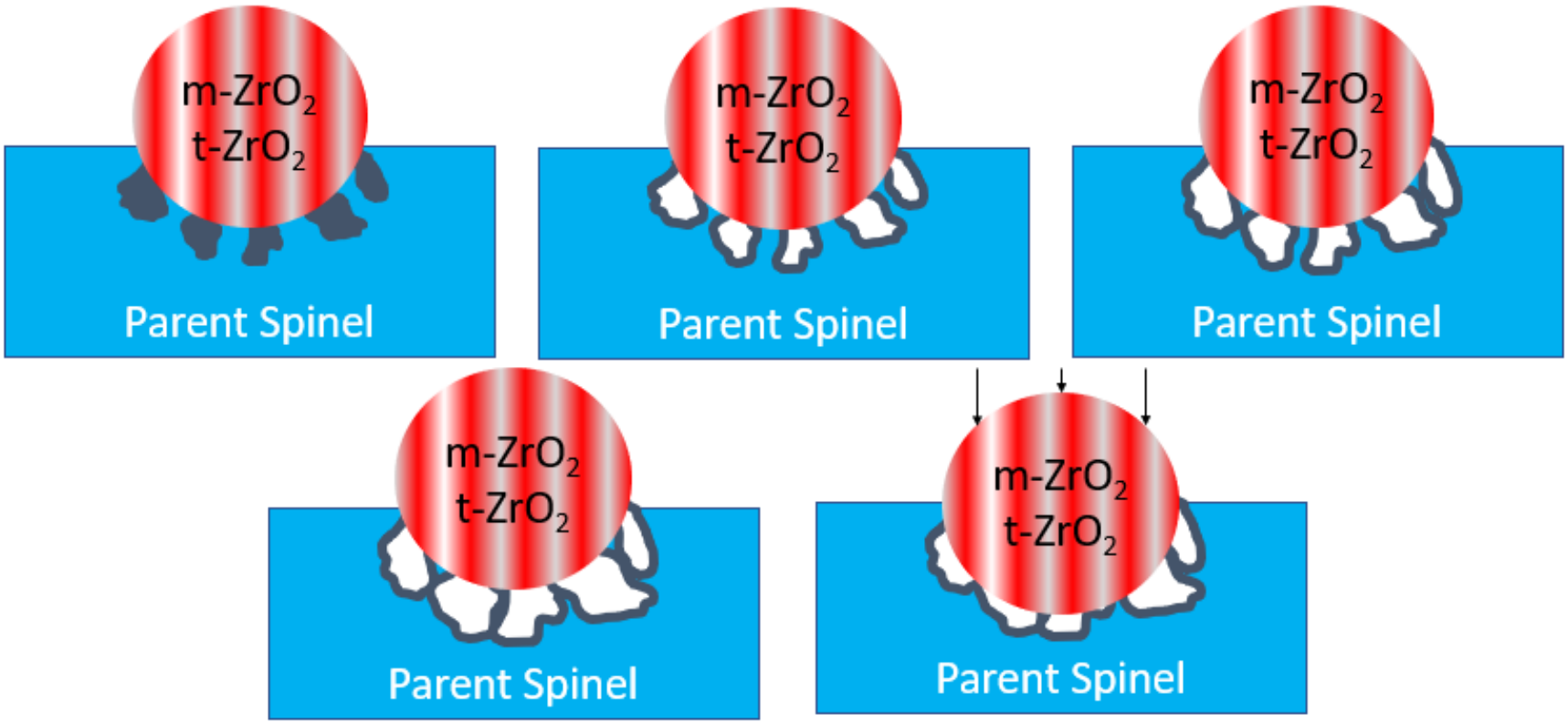


**Figure 51: Schematic showing the recurring void formation of the Nanoscale Kirkendall Effect.**

## 2. Application of the Enhanced Interfacial Diffusion Model to the Tunneling Phenomenon

A model solely based on the local stress fields underneath the $ZrO_2$ lacks a plausible explanation for the perpetuation of the tunneling phenomenon. In other words, localized compression and tension areas may be present initially, but it is unclear if/how these perturbations would be maintained as the tunneling proceeds. Lattice strain effects should not be completely dismissed as the mechanism may still play a role; however, the contribution to the tunneling phenomenon is unclear. Below, the enhanced interfacial diffusion model is used to address the evidence for the tunneling phenomenon.

***Tunneling occurs with both $ZrO_2$ as well as $HfO_2$, with about the same rates. Similar rates are observed with changes in support chemistry, as long as some reducible content is present.***

Both $ZrO_2$ and $HfO_2$ modified spinel exhibit the tunneling phenomenon at similar rates, which agrees with the model as an interface that facilitates expedited diffusion is needed to activate and perpetuate the process. Changes in the tunneling onset temperature may arise from the differences in modifier crystal structure, local modifier particle texture at the interface, or crystallographic orientation of the spinel beneath the modifier. Any of these features may bring fundamental differences in diffusion; for example, the monoclinic to tetragonal phase transition in $ZrO_2$ increases oxygen diffusion by 4-5 orders of magnitude.[202] Changes in spinel composition should not affect the tunneling phenomenon significantly if the individual rates of the constituents are considered. Most of the chemistry changes are on the A-site cation, which has relatively the same diffusion coefficient at any given temperature, as shown in Figure 37.

***The interface between the $ZrO_2$ and spinel is Ni deficient, with oxygen bonding resembling a defect spinel structure.***

A consequence of the interfacial diffusion enhancement model is the redistribution of atoms (Mg, Al, Co, Ni, O) to either another surface or defects, which leaves a newly created defective spinel layer. In the simplest case of $NiAl_2O_4$, a Ni deficient $Al_2O_3$-like layer was identified between the $ZrO_2$ and bulk spinel. Ni deficiency indirectly hints that the cations have either diffused out of the surrounding spinel or are diffusing through the defective layer to the surface. Either case is plausible, as evidenced by bulk structural

relaxation at low $p_{O_2}$ in the $N_2$-HTXRD experiment, by thermodynamic arguments for phase regeneration, and by Raman spectroscopy showing the vacuum oxidized surface has some residual disorder, but to a lesser extent than the fully reduced sample. Regardless of pathway, Ni deficiency promotes the idea of the interfacial diffusion enhancement model, as cations can be redistributed via surface diffusion or react with defective spinel in some fashion.

***Non-homogeneously dispersed voids are observed beneath the tunneled $ZrO_2$.***

Voids are a hallmark feature of the Kirkendall process, as they are the result of diffusional flux mismatches between two regions. The non-homogeneous dispersion of these voids may be attributed to the local inhomogeneities of texture in the $ZrO_2$ modifier and/or the crystallographic direction of the spinel at the interface. Neither pathway can be confirmed; however, voids most likely form from the mismatch in diffusion, akin to the Kirkendall mechanism as discussed previously.

***Tunneling occurs without the beam and its rate is the same order of magnitude as bulk cation diffusion in spinel. Tunneling rates with the beam are expedited, which are within a few orders of magnitude for $Ni^{2+}$ diffusion in defective $MgO{\cdot}xAl_2O_3$, or Ni grain boundary diffusion in $NiO\text{-}Al_2O_3$ diffusion couples.***

The enhanced interfacial diffusion effects occur independently of electron irradiation in vacuum, but the rate at which the effect occurs is hastened by the electron beam. The model does not explain this observation, except to the extent that increased local temperature will increase diffusion rates for all species. Without electron irradiation, the tunneling rate matches that of Ni bulk diffusion in spinel. Enhanced rates as observed by electron irradiation may be due to the creation of additional defects in combination with elevated temperatures, in which voids can form faster, expediting the overall process. This is supported by rates close to those of Ni diffusion in $MgO{\cdot}xAl_2O_3$ and Ni grain boundary diffusion in $NiO\text{-}Al_2O_3$ diffusion couples.

***$MgAl_2O_4$ does not exhibit tunneling, so the mechanism is clearly related to the defect structure that arises from selective removal of Ni and oxygen ions.***

$MgAl_2O_4$ has no reducible content, i.e. no Ni or Co. This indicates that an initial defect concentration to some extent is required for tunneling to occur. The process of selective reduction leaves metal vacancies as well as vacancies on the oxygen sublattice.[62]

Both of these factors contribute to expedited diffusion in spinel of both cations[30] and anions,[33, 178, 260] in which then modifier tunneling can occur.

# IV. SUMMARY AND CONCLUSIONS

Enhanced transport has been identified and systematically investigated on a model $NiAl_2O_4$ + 2.5 wt.% $ZrO_2$ catalyst under relevant service $p_{O_2}$ conditions. Novel low voltage *in-situ* HTSEM teamed with complementary characterization techniques provided a unique picture in elucidating the mechanisms behind morphological and structural changes upon redox cycling, which culminate in improved catalytic properties. All mass transport was found to be ultimately governed by the stoichiometry of the supporting spinel, with additional effects attributable to the modifying oxide.

Structural relaxation on a bulk scale has been demonstrated via HTXRD in pre-reduced spinel reoxidized in air and in vacuum. Regeneration was $p_{O_2}$ dependent: at high $p_{O_2}$ NiO formation was favored. At low $p_{O_2}$, no evidence of NiO formation is present, indicating regenerative oxidation of Ni occured either at the triple phase boundary or by the formation of a core-shell structure which immediately reacts with the underlying defective spinel. HTXRD reveals residual spinel microstrain of both air and vacuum oxidized samples, which is decreased notably above 900°C, and can be attributed to structural relaxation by the reduction of point defects on the bulk scale. The vacuum reoxidized samples contain residual surface defects as compared to the air reoxidized samples as evidenced from Raman spectroscopy.

Surface Ni particles previously reduced from the parent oxide migrate and coalesce over large distances at elevated temperatures, reaching up to 350x the predicted migration distances. Surface transport enhancement can be attributed to surface defects induced by the reduction process, as evidenced from Raman spectroscopy, as well as undercoordinated surface features. Surface texturing in the form of pits and crevasses were revealed after migration and coalescence because the selectively reduced Ni particles were embedded into the spinel surface. Surface texturing could not be healed by reheating in oxidizing environments at T ≤ 1100°C; however, microstructural features such as facet edges and pore walls sharpened by heat treatment at 1100°C - which indicates some structural rearrangement occurred. In an extension to technologically relevant Ni-Co-Mg spinel catalysts, HTXRD revealed reversible phase changes whereas the morphology changed noticeably with each redox cycle. Microstructural maturation of this nature increased the

particle number density and wt. % of exsolved metal while reducing the average particle size, which explains the enhanced catalytic activity upon redox cycling for this composition.[65]

Tunneling of the $ZrO_2$ and $HfO_2$ into the spinel surface was found to be relatively insensitive to both the spinel and modifier composition, as rates did not significantly vary. The tunneling phenomenon was found to be thermally activated; it is apparent that some reducible metal content is required to observe the tunneling effect, as no tunneling was found for $MgAl_2O_4$. In other words, a defective spinel surface is required. Activation energy of the $NiAl_2O_4$ + 2.5 wt.% $ZrO_2$ composition resembled that of Ni diffusion in defective $MgO{\cdot}xAl_2O_3$.[30] Voids were also found to form under the $ZrO_2$ particles, and the spinel-$ZrO_2$ interface was shown to be Ni deficient, resembling the defect spinel, $\gamma$-$Al_2O_3$. $HfO_2$ was also identified as an ideal candidate due to the similarity in morphology, particle distribution, and phase to the $ZrO_2$ modifier. $ZrO_2$ modified spinel exhibited tunneling at temperatures starting at 1000°C, where the $HfO_2$ modified spinel only exhibited tunneling at the maximum temperature studied of 1200°C. All evidence gained suggests a model based on enhanced diffusion along the spinel-modifier interface, thus enabling rapid mass transport from the bulk to the surface via this short-circuit diffusion pathway.

Overall, significant progress has been made in understanding the dynamics of redox cycling of oxide supported metal catalysts, including intermediate steps to deactivation, explanation of enhanced properties upon regeneration, and elucidation of enhanced mass transport properties. Subsequent studies can use the results and techniques to design more efficient catalysts, prolong catalyst lifetime, or for new fabrication routes of nanostructured porous oxides via microstructural maturation and the observed tunneling phenomenon.

# V. FUTURE WORK

Now that enhanced surface and mass transport has been firmly established on $Ni_xMg_{1-x}Al_2O_4$, a more extensive investigation of the solid solution series is needed to fully understand the nature of transport. Particle migration distances can be measured on specifically the x = 0.75 and 0.50 compositions, after which conclusions can be drawn about the support Ni content (and consequently the qualitative number of defects) on the surface particle migration. Furthermore, if the defect content could be quantified, it may be related to the migration distance quantitatively rather than qualitatively. Atomic resolution TEM investigations may prove fruitful in identifying coordination in the defect spinel, hinting at the defect content.

Modifier tunneling can also be studied further, by expanding the number of support compositions that exhibit the phenomenon, i.e. the x = 0.75 and x = 0.25 support compositions of the $Ni_xMg_{1-x}Al_2O_4$ series. Varying the Ni, and inherently the allowable defect content, may provide a more complete picture of the tunneling mechanism. More critically, a study of this nature will allow for a systematic investigation to identify a minimum Ni concentration for the tunneling phenomenon to occur, which in turn fixes the defect content. As mentioned before, if the defect content could be somehow quantified, a realm of possibilities is opened for better understanding the tunneling phenomenon and transport on spinel in general.

As demonstrated by this study, $HfO_2$ showed similar properties to $ZrO_2$ in terms of tunneling on the spinel. Changes in tunneling onset temperature were posited to possibly be attributed to differences in phase compositions, modifier texture at the interface, or the spinel crystallographic orientation beneath the particle. To address the changes in modifier phase, synthesis could be conducted at higher temperatures for the modifying oxides, where $HfO_2$ exhibits both tetragonal and monoclinic polymorphs (at temperatures above 1750°C), making the $HfO_2$ modification akin to the $ZrO_2$. Tunneling onset temperature could then be evaluated for both modifier compositions with the same modifier phase assemblages, providing more information toward the proposed model. Evaluating the modifier texture at the interface and the spinel crystallographic orientation is time and labor

intensive, requiring multiple FIB and TEM samples, which are difficult to produce because of the geometrical requirements for sample preparation.

Additionally, $HfO_2$ tunneling on other compositions could be further explored, although such investigations may not prove fruitful, as the $NiAl_2O_4$ + 2.5wt.% $ZrO_2$ composition exhibited tunneling at 1000°C and as the Ni content decreased, the onset temperature increased. With $NiAl_2O_4$ + 2.5wt.% $HfO_2$ composition exhibiting tunneling at 1200°C which is the maximum temperature of the Protochips stage, tunneling may not be observed as Mg is substituted into the spinel.

Obviously, due to external instrumental constraints, the FIB, TEM, and EELS investigations were limited in this study. With the arrival of these instruments to Alfred University, a more extensive evaluation could be conducted in future work on all compositions that exhibit tunneling, providing additional insight into the legitimacy of the proposed diffusional model.

In a final note, the extension to other reducible oxide systems such as perovskites and pyrochlores could offer acuity on the role of defects on transport in these systems. For example, Neagu et al. have demonstrated that particle stability can be enhanced in Ni exsolved perovskites by intentional A-site deficiencies to reestablish stoichiometry in the reduced composite, effectively creating a socketed Ni particle supported on a stoichiometric oxide.[14] These catalysts showed enhanced particle sintering and decreased coking during reforming, which they attribute to the socketing of the Ni into the support. This particular strategy is not applicable to $NiAl_2O_4$, as excess NiO spinel is not possible, however, it may be utilized in Mg substituted versions.

# VI. REFERENCES


1. DOE Quadrennial Technology Review 2015 | Department of Energy. https://www.energy.gov/quadrennial-technology-review-2015 (accessed January 11, 2019).
2. Administration, E. I. International - U.S. Energy Information Administration (EIA). https://www.eia.gov/beta/international (accessed January 9, 2019).
3. Robertson, A. J. B., The Early History of Catalysis. *Platinum Met. Rev.* **1975,** *19* (2), 64-69.
4. Hunt, B. L., The Ammonia Oxidation Process for Nitric Acid Manufacture: Early Developments with Platinum Catalysts. *Platinum Met. Rev.* **1958,** *2* (4), 129-134.
5. Auprêtre, F.; Descorme, C.; Duprez, D., Bio-ethanol catalytic steam reforming over supported metal catalysts. *Catal. Commun.* **2002,** *3* (6), 263-267.
6. Tomishige, K.; Miyazawa, T.; Asadullah, M.; Ito, S.-i.; Kunimori, K., Catalyst performance in reforming of tar derived from biomass over noble metal catalysts. *Green Chem.* **2003,** *5* (4), 399-403.
7. Tsyganok, A. I.; Inaba, M.; Tsunoda, T.; Hamakawa, S.; Suzuki, K.; Hayakawa, T., Dry reforming of methane over supported noble metals: a novel approach to preparing catalysts. *Catal. Commun.* **2003,** *4* (9), 493-498.
8. Zhang, B.; Tang, X.; Li, Y.; Cai, W.; Xu, Y.; Shen, W., Steam reforming of bio-ethanol for the production of hydrogen over ceria-supported Co, Ir and Ni catalysts. *Catal. Commun.* **2006,** *7* (6), 367-372.
9. Matsuoka, K.; Shimbori, T.; Kuramoto, K.; Hatano, H.; Suzuki, Y., Steam Reforming of Woody Biomass in a Fluidized Bed of Iron Oxide-Impregnated Porous Alumina. *Energy & Fuels* **2006,** *20* (6), 2727-2731.
10. Yung, M. M.; Jablonski, W. S.; Magrini-Bair, K. A., Review of Catalytic Conditioning of Biomass-Derived Syngas. *Energy & Fuels* **2009,** *23* (4), 1874-1887.
11. Irvine, J. T. S.; Neagu, D.; Verbraeken, M. C.; Chatzichristodoulou, C.; Graves, C.; Mogensen, M. B., Evolution of the electrochemical interface in high-temperature fuel cells and electrolysers. *Nat. Energy* **2016,** *1* (1), 15014.
12. Neagu, D.; Irvine, J. T. S., Enhancing Electronic Conductivity in Strontium Titanates through Correlated A and B-Site Doping. *Chem. Mater.* **2011,** *23* (6), 1607--1617.
13. Neagu, D.; Irvine, J. T. S., Structure and Properties of $La_{0.4}Sr_{0.4}TiO_3$ Ceramics for Use as Anode Materials in Solid Oxide Fuel Cells. *Chem. Mater.* **2010,** *22* (17), 5042--5053.
14. Neagu, D.; Oh, T.-S.; Miller, D. N.; Ménard, H.; Bukhari, S. M.; Gamble, S. R.; Gorte, R. J.; Vohs, J. M.; Irvine, J. T. S., Nano-socketed nickel particles with enhanced coking resistance grown in situ by redox exsolution. *Nat. Commun.* **2015,** *6*, 8120.
15. Neagu, D.; Papaioannou, E. I.; Ramli, W. K. W.; Miller, D. N.; Murdoch, B. J.; Ménard, H.; Umar, A.; Barlow, A. J.; Cumpson, P. J.; Irvine, J. T. S.; Metcalfe,

I. S., Demonstration of chemistry at a point through restructuring and catalytic activation at anchored nanoparticles. *Nat. Commun.* **2017,** *8* (1), 1855.
16. Neagu, D.; Tsekouras, G.; Miller, D. N.; Ménard, H.; Irvine, J. T. S., In situ growth of nanoparticles through control of non-stoichiometry. *Nat. Chem.* **2013,** *5* (11), 916.
17. Oh, T.-S.; Rahani, E. K.; Neagu, D.; Irvine, J. T. S.; Shenoy, V. B.; Gorte, R. J.; Vohs, J. M., Evidence and Model for Strain-Driven Release of Metal Nanocatalysts from Perovskites during Exsolution. *J. Phys. Chem. Lett.* **2015,** *6* (24), 5106--5110.
18. Sun, Y.; Li, J.; Zeng, Y.; Amirkhiz, B. S.; Wang, M.; Behnamian, Y.; Luo, J., A-site deficient perovskite: the parent for in situ exsolution of highly active, regenerable nano-particles as SOFC anodes. *J. Mater. Chem. A* **2015,** *3* (20), 11048--11056.
19. Miyatani, K.; Wada, Y.; Okamoto, F., Magnetic Properties of Single Crystal Chalcogenide Spinels; $CuCr_2X_3Y$ (X=S, Se and Te, Y=C1, Br and I) System. *J. Phys. Soc. Jpn.* **1968,** *25* (2), 369-372.
20. Sickafus, K. E.; Wills, J. M.; Grimes, N. W., Structure of Spinel. *J. Am. Ceram. Soc.* **1999,** *82* (12), 3279-3292.
21. Grimes, N. W., The spinels: versatile materials. *Phys. Technol.* **1975,** *6* (1), 22.
22. Mocala, K.; Navrotsky, A., Structural and Thermodynamic Variation in Nickel Aluminate Spinel. *J. Am. Ceram. Soc.* **1989,** *72* (5), 826-832.
23. Porta, P.; Stone, F. S.; Turner, R. G., The distribution of nickel ions among octahedral and tetrahedral sites in $NiAl_2O_4$-$MgAl_2O_4$ solid solutions. *J. Solid State Chem.* **1974,** *11* (2), 135-147.
24. Hill, R. J.; Craig, J. R.; Gibbs, G. V., Systematics of the spinel structure type. *Phys. Chem. Miner.* **1979,** *4* (4), 317-339.
25. Ball, J. A.; Murphy, S. T.; Grimes, R. W.; Bacorisen, D.; Smith, R.; Uberuaga, B. P.; Sickafus, K. E., Defect processes in $MgAl_2O_4$ spinel. *Solid State Sci.* **2008,** *10* (6), 717-724.
26. Halevy, I.; Dragoi, D.; Üstündag, E.; Yue, A. F.; Arredondo, E. H.; Hu, J.; Somayazulu, M. S., The effect of pressure on the structure of $NiAl_2O_4$. *J. Phys.: Condens. Matter* **2002,** *14* (44), 10511.
27. O'Neill, H. S. C.; Navrotsky, A., Simple spinels; crystallographic parameters, cation radii, lattice energies, and cation distribution. *Am. Mineral.* **1983,** *68* (1-2), 181-194.
28. Yong Sheng, H.; Jian Bao, L.; Xiao Shan, N.; Bo, C.; Johnson, D., Temperature Dependence of the Cation Distribution in Nickel Aluminate Spinel from Thermodynamics and X-Rays. *J. Am. Ceram. Soc.* **2005,** *88* (12), 3455-3457.
29. O'Quinn, E. C.; Shamblin, J.; Perlov, B.; Ewing, R. C.; Neuefeind, J.; Feygenson, M.; Gussev, I.; Lang, M., Inversion in $Mg_{1-x}Ni_xAl_2O_4$ Spinel: New Insight into Local Structure. *J. Am. Chem. Soc.* **2017,** *139* (30), 10395-10402.
30. Yamaguchi, G.; Nakano, M.; Tosaki, M., Effects of Cation Vacancies of the Diffusion of Nickel Ions in Defective Spinels. *Bull. Chem. Soc. Jpn.* **1969,** *42* (10), 2801-2807.
31. Sheldon, R. I.; Hartmann, T.; Sickafus, K. E.; Ibarra, A.; Scott, B. L.; Argyriou, D. N.; Larson, A. C.; Von Dreele, R. B., Cation Disorder and Vacancy

Distribution in Nonstoichiometric Magnesium Aluminate Spinel, $MgO \cdot xAl_2O_3$. *J. Am. Ceram. Soc.* **1999,** *82* (12), 3293-3298.
32. Okuyama, Y.; Kurita, N.; Fukatsu, N., Defect structure of alumina-rich nonstoichiometric magnesium aluminate spinel. *Solid State Ionics* **2006,** *177* (1–2), 59-64.
33. Reddy, K. P. R.; Cooper, A. R., Oxygen Diffusion in Magnesium Aluminate Spinel. *J. Am. Ceram. Soc.* **1981,** *64* (6), 368-371.
34. Miller, J. A.; Reimanis, I. E.; Miao, W.; Sutorik, A. C., Diffusion limited precipitation of alumina in magnesium aluminate spinel. *J. Am. Ceram. Soc.* **2017,** *100* (3), 894-900.
35. Schmalzried, H., Röntgenographische Untersuchung der Kationenverteilung in Spinellphasen. *Z. Phys. Chem.* **1961,** *28* (3_4), 203-219.
36. Rotan, M.; Tolchard, J.; Rytter, E.; Einarsrud, M.-A.; Grande, T., On the solid solution of the spinel phase in the system $NiO–Al_2O_3$. *J. Solid State Chem.* **2009,** *182* (12), 3412-3415.
37. Roy, D. M.; Roy, R.; Osborn, E. F., The system $MgO\text{-}Al_2O_3\text{-}H_2O$ and influence of carbonate and nitrate ions on the phase equilibria. *Am. J. Sci.* **1953,** *251* (5), 337-361.
38. Mazzoni, A. D.; Sainz, M. A.; Caballero, A.; Aglietti, E. F., Formation and sintering of spinels ($MgAl_2O_4$) in reducing atmospheres. *Mater. Chem. Phys.* **2003,** *78* (1), 30-37.
39. Ting, C.-J.; Lu, H.-Y., Defect Reactions and the Controlling Mechanism in the Sintering of Magnesium Aluminate Spinel. *J. Am. Ceram. Soc.* **1999,** *82* (4), 841-848.
40. Lejus, A.-M., Sur la formation à haute température de spinelles non stoechiométriques et de phases dérivées dans plusieurs systèmes d'oxydes à base d'alumine et dans le système alumine-nitrure d'aluminium. *Rev. Hautes Temp. Refractaires* **1964**.
41. Colin, F.; Thery, J., Sur La Structure Et Les Properietes Des Composes Formes Par Lalumine Avec Les Oxydes Des Elements Du Groupe 2B. *Comptes Rendus Hebdomadaires Des Seances De L'Academie Des Sciences Serie C* **1966,** *263* (20), 1220-&.
42. Colin, F., Contribution to the Study of Phases Formed During the Reduction of Certain Mixed Oxides in $Al_2O_3$ MO. *Rev. Int. Hautes Temp. Refract.* **1968,** *5* (4), 267-83.
43. Bassoul, P.; Lefebvre, A.; Gilles, J. C., Phases ε obtenues par decomposition des spinelles non-stoechiometriques dans les systemes $Ga_2O_3$-MgO, $Al_2O_3$-NiO, $Al_2O_3$-AlN et $Al_2O_3\text{-}Li_2O$. *Mater. Res. Bull.* **1976,** *11* (1), 11-14.
44. Bassoul, P.; Gilles, J. C., Structure and microstructure of the metastable B phase ($NiAl_{10}O_{16}$): I. Preparation and structural study by X-ray diffraction. *J. Solid State Chem.* **1985,** *58* (3), 383-388.
45. Bassoul, P.; Gilles, J. C., Structure and microstructure of the metastable B phase ($NiAl_{10}O_{16}$): II. An electron microscopic investigation of the microstructure. *J. Solid State Chem.* **1985,** *58* (3), 389-397.
46. Zhang, Z.; Üstündag, E.; Sass, S. L., Partial Reduction of $NiAl_2O_4$ - Mechanism and the Influence of Doping. *Mater. Res. Soc. Symp. Proc.* **1995,** *398*, 489.

47. Wang, Y.; Cormack, A. N., Distribution of alkaline earth ions in β″-alumina: a computer simulation study. *Solid State Ionics* **1998,** *111* (3), 333-344.
48. Wefers, K.; Misra, C., *Oxides and hydroxides of aluminum*. Alcoa Laboratories Pittsburgh: 1987; Vol. 19.
49. Levin, I.; Brandon, D., Metastable alumina polymorphs : Crystal structures and transition sequences. *J. Am. Ceram. Soc.* **1998,** *81* (8), 1995-2012.
50. Zhou, R.-S.; Snyder, R. L., Structures and transformation mechanisms of the η, γ and θ transition aluminas. *Acta Crystallogr. Sect. B: Struct. Sci.* **1991,** *47* (5), 617-630.
51. Burtin, P.; Brunelle, J. P.; Pijolat, M.; Soustelle, M., Influence of surface area and additives on the thermal stability of transition alumina catalyst supports. I: Kinetic data. *Appl. Catal.* **1987,** *34*, 225-238.
52. Chary, K. V. R.; Ramana Rao, P. V.; Venkat Rao, V., Catalytic functionalities of nickel supported on different polymorphs of alumina. *Catal. Commun.* **2008,** *9* (5), 886-893.
53. Lippens, B.; De Boer, J., Study of phase transformations during calcination of aluminum hydroxides by selected area electron diffraction. *Acta Crystallogr.* **1964,** *17* (10), 1312-1321.
54. John, C. S.; Alma, N. C. M.; Hays, G. R., Characterization of transitional alumina by solid-state magic angle spinning aluminium NMR. *Appl. Catal.* **1983,** *6* (3), 341-346.
55. Shirasuka, K.; Yanagida, H.; Yamaguchi, G.; Kyokaishi, Y., The preparation of eta alumina and its structure. *J. Ceram. Soc. Jpn.* **1976,** *84*, 610-613.
56. Wolverton, C.; Hass, K. C., Phase stability and structure of spinel-based transition aluminas. *Phys. Rev. B: Condens. Matter* **2000,** *63* (2), 024102.
57. Samain, L.; Jaworski, A.; Edén, M.; Ladd, D. M.; Seo, D.-K.; Javier Garcia-Garcia, F.; Häussermann, U., Structural analysis of highly porous γ-$Al_2O_3$. *J. Solid State Chem.* **2014,** *217*, 1-8.
58. Paglia, G.; Božin, E. S.; Billinge, S. J. L., Fine-Scale Nanostructure in γ-$Al_2O_3$. *Chem. Mater.* **2006,** *18* (14), 3242-3248.
59. Shamblin, J.; Feygenson, M.; Neuefeind, J.; Tracy, C. L.; Zhang, F.; Finkeldei, S.; Bosbach, D.; Zhou, H.; Ewing, R. C.; Lang, M., Probing disorder in isometric pyrochlore and related complex oxides. *Nat. Mater.* **2016,** *15* (5), 507-511.
60. Laguna-Bercero, M. A.; Sanjuán, M. L.; Merino, R. I., Raman spectroscopic study of cation disorder in poly- and single crystals of the nickel aluminate spinel. *J. Phys.: Condens. Matter* **2007,** *19* (18), 186217.
61. Ivanov, V. G.; Abrashev, M. V.; Iliev, M. N.; Gospodinov, M. M.; Meen, J.; Aroyo, M. I., Short-range B-site ordering in the inverse spinel ferrite $NiFe_2O_4$. *Phys. Rev. B: Condens. Matter* **2010,** *82* (2), 024104.
62. Miller, M. E.; Misture, S. T., Idealizing γ-$Al_2O_3$: In Situ Determination of Nonstoichiometric Spinel Defect Structure. *J. Phys. Chem. C* **2010,** *114* (30), 13039-13046.
63. Benrabaa, R.; Barama, A.; Boukhlouf, H.; Guerrero-Caballero, J.; Rubbens, A.; Bordes-Richard, E.; Löfberg, A.; Vannier, R.-N., Physico-chemical properties and syngas production via dry reforming of methane over $NiAl_2O_4$ catalyst. *Int. J. Hydrogen Energy* **2017,** *42* (18), 12989-12996.

64. Hill, B. E.; Misture, S. T., Atomic Scale Mechanisms of the Reduction of Nickel-Magnesium Aluminate Spinels. *J. Am. Ceram. Soc.* **2013,** *96* (11), 3603-3608.
65. Misture, S. T.; McDevitt, K. M.; Glass, K. C.; Edwards, D. D.; Howe, J. Y.; Rector, K. D.; He, H.; Vogel, S. C., Sulfur-resistant and regenerable Ni/Co spinel-based catalysts for methane dry reforming. *Catal. Sci. Technol.* **2015,** *5* (9), 4565-4574.
66. Kikuchi, R.; Yokoyama, M.; Tada, S.; Takagaki, A.; Sugawara, T.; Oyama, S. T., Novel Nickel Catalysts Based on Spinel-Type Mixed Oxides for Methane and Propane Steam Reforming. *J. Chem. Eng. Jpn.* **2014,** *47* (7), 530-535.
67. Achouri, I. E.; Abatzoglou, N.; Fauteux-Lefebvre, C.; Braidy, N., Diesel steam reforming: Comparison of two nickel aluminate catalysts prepared by wet-impregnation and co-precipitation. *Catal. Today* **2013,** *207*, 13-20.
68. de Sousa, F. F.; de Sousa, H. S. A.; Oliveira, A. C.; Junior, M. C. C.; Ayala, A. P.; Barros, E. B.; Viana, B. C.; Filho, J. M.; Oliveira, A. C., Nanostructured Ni-containing spinel oxides for the dry reforming of methane: Effect of the presence of cobalt and nickel on the deactivation behaviour of catalysts. *Int. J. Hydrogen Energy* **2012,** *37* (4), 3201-3212.
69. Pinheiro, A. L.; Pinheiro, A. N.; Valentini, A.; Filho, J. M.; Sousa, F. F. d.; Sousa, J. R. d.; Rocha, M. d. G. C.; Bargiela, P.; Oliveira, A. C., Analysis of coke deposition and study of the structural features of $MAl_2O_4$ catalysts for the dry reforming of methane. *Catal. Commun.* **2009,** *11* (1), 11-14.
70. Quénard, O.; Laurent, C.; Brieu, M.; Rousset, A., Synthesis, microstructure and oxidation of Co-$MgAl_2O_4$ and Ni-$MgAl_2O_4$ nanocomposite powders. *Nanostruct. Mater.* **1996,** *7* (5), 497-507.
71. Hyun-Seog, R.; Kee Young, K.; Jin Hyeok, J.; Yu Taek, S.; Dong Joo, S.; Yong-Seog, S.; Wang Lai, Y.; Park, S. B., Combined reforming of methane over supported Ni catalysts. *Catal. Lett.* **2007,** *117* (1/2), 85-90.
72. Hill, B. Characterizing the Reduction of $Ni_xMg_{1-x}Al_2O_4$. Ph.D. Thesis, Alfred University, Alfred, NY, 2012.
73. Elrefaie, F. A.; Smeltzer, W. W., Thermodynamics of Nickel-Aluminum-Oxygen System Between 900 and 1400 K. *J. Electrochem. Soc.* **1981,** *128* (10), 2237-2242.
74. Taylor, J. R.; Dinsdale, A. T., A thermodynamic assessment of the Ni-O, Cr-O and Cr-Ni-O systems using the ionic liquid and compound energy models. *Zeitschrift für Metallkunde* **1990,** *81* (5), 354-366.
75. Mermelstein, J.; Brandon, N.; Millan, M., Impact of Steam on the Interaction between Biomass Gasification Tars and Nickel-Based Solid Oxide Fuel Cell Anode Materials. *Energy & Fuels* **2009,** *23* (10), 5042-5048.
76. Sehested, J.; Gelten, J. A. P.; Helveg, S., Sintering of nickel catalysts: Effects of time, atmosphere, temperature, nickel-carrier interactions, and dopants. *Appl. Catal., A* **2006,** *309* (2), 237-246.
77. Pompeo, F.; Nichio, N. N.; Souza, M. M. V. M.; Cesar, D. V.; Ferretti, O. A.; Schmal, M., Study of Ni and Pt catalysts supported on $\alpha$-$Al_2O_3$ and $ZrO_2$ applied in methane reforming with $CO_2$. *Appl. Catal., A* **2007,** *316* (2), 175-183.
78. Argyle, M.; Bartholomew, C., Heterogeneous Catalyst Deactivation and Regeneration: A Review. *Catalysts* **2015,** *5* (1), 145-269.

79. Bartholomew, C. H., Mechanisms of catalyst deactivation. *Appl. Catal., A* **2001,** *212* (1–2), 17-60.
80. Challa, S. R.; Delariva, A. T.; Hansen, T. W.; Helveg, S.; Sehested, J.; Hansen, P. L.; Garzon, F.; Datye, A. K., Relating Rates of Catalyst Sintering to the Disappearance of Individual Nanoparticles during Ostwald Ripening. *J. Am. Chem. Soc.* **2011,** *133* (51), 20672-20675.
81. Sehested, J., Sintering of nickel steam-reforming catalysts. *J. Catal.* **2003,** *217* (2), 417-426.
82. Sehested, J.; Carlsson, A.; Janssens, T. V. W.; Hansen, P. L.; Datye, A. K., Sintering of Nickel Steam-Reforming Catalysts on $MgAl_2O_4$ Spinel Supports. *J. Catal.* **2001,** *197* (1), 200-209.
83. Crozier, P. A.; Hansen, T. W., In situ and operando transmission electron microscopy of catalytic materials. *MRS Bull.* **2015,** *40* (01), 38-45.
84. DeLaRiva, A. T.; Hansen, T. W.; Challa, S. R.; Datye, A. K., In situ Transmission Electron Microscopy of catalyst sintering. *J. Catal.* **2013,** *308*, 291-305.
85. Hansen, T. W.; DeLaRiva, A. T.; Challa, S. R.; Datye, A. K., Sintering of Catalytic Nanoparticles: Particle Migration or Ostwald Ripening? *Acc. Chem. Res.* **2013,** *46* (8), 1720-1730.
86. Hansen, T. W.; Wagner, J. B., Catalysts under Controlled Atmospheres in the Transmission Electron Microscope. *ACS Catal.* **2014,** *4* (6), 1673-1685.
87. Chenna, S.; Crozier, P. A., In situ environmental transmission electron microscopy to determine transformation pathways in supported Ni nanoparticles. *Micron* **2012,** *43* (11), 1188-1194.
88. Pannell, R. B.; Chung, K. S.; Bartholomew, C. H., The stoichiometry and poisoning by sulfur of hydrogen, oxygen and carbon monoxide chemisorption on unsupported nickel. *J. Catal.* **1977,** *46* (3), 340-347.
89. Shen, W. M.; Dumesic, J. A.; Hill, C. G., Criteria for stable Ni particle size under methanation reaction conditions: Nickel transport and particle size growth via nickel carbonyl. *J. Catal.* **1981,** *68* (1), 152-165.
90. Guo, Y.; Zhou, L.; Kameyama, H., Steam reforming reactions over a metal-monolithic anodic alumina-supported Ni catalyst with trace amounts of noble metal. *Int. J. Hydrogen Energy* **2011,** *36* (9), 5321-5333.
91. Rostrup-Nielsen, J. R., Some principles relating to the regeneration of sulfur-poisoned nickel catalyst. *J. Catal.* **1971,** *21* (2), 171-178.
92. Tanaka, H.; Uenishi, M.; Taniguchi, M.; Tan, I.; Narita, K.; Kimura, M.; Kaneko, K.; Nishihata, Y.; Mizuki, J. i., The intelligent catalyst having the self-regenerative function of Pd, Rh and Pt for automotive emissions control. *Catal. Today* **2006,** *117* (1–3), 321-328.
93. Felix, L. G.; Choi, C. W.; Rue, D. M.; Weast, L. E.; Seward, T. P., Robust glass-ceramics catalysts for biomass gasification. *Environ. Prog. Sustainable Energy* **2009,** *28* (3), 336-346.
94. Felix, L. G.; Rue, D. M.; Iii, T. P. S.; Weast, L. E. "Method for producing catalytically active glass-ceramic materials, and glass-ceramics produced thereby". U.S. Pat. 20090011925 A1, 2009/01/08/, 2009.

95. Remiro, A.; Arandia, A.; Oar-Arteta, L.; Bilbao, J.; Gayubo, A. G., Regeneration of $NiAl_2O_4$ spinel type catalysts used in the reforming of raw bio-oil. *Appl. Catal., B* **2018,** *237*, 353-365.
96. Hashhemnjad, S. M.; Parvari, M., Deactivation and Regeneration of Nickel-Based Catalysts for Steam-Methane Reforming. *Chin. J. Catal.* **2011,** *32* (1–2), 273-279.
97. Appari, S.; Janardhanan, V. M.; Bauri, R.; Jayanti, S., Deactivation and regeneration of Ni catalyst during steam reforming of model biogas: An experimental investigation. *Int. J. Hydrogen Energy* **2014,** *39* (1), 297-304.
98. Dega, F. B.; Abatzoglou, N., H2S Poisoning and Regeneration of a Nickel Spinellized Catalyst Prepared from Waste Metallurgical Residues, During Dry Autothermal Methane Reforming. *Catal. Lett.* **2019,** *149* (6), 1730-1742.
99. Du, J.; Gao, J.; Gu, F.; Zhuang, J.; Lu, B.; Jia, L.; Xu, G.; Liu, Q.; Su, F., A strategy to regenerate coked and sintered $Ni/Al_2O_3$ catalyst for methanation reaction. *Int. J. Hydrogen Energy* **2018,** *43* (45), 20661-20670.
100. Chang, W. S.; Chen, S.; Shen, P., Phase equilibria of zirconia-dispersed ceramic in $NiO{\cdot}Al_2O_3{\cdot}ZrO_2$ system. *Mater. Sci. Eng., A* **1991,** *145* (1), 113-118.
101. Chang, W. S.; Shen, P.; Chen, S., Microstructural development of zirconia-dispersed ceramic in the $NiO{\cdot}Al_2O_3{\cdot}ZrO_2$ system. *Mater. Sci. Eng., A* **1991,** *148* (1), 145-153.
102. Shen, P.; Chen, S.; Chang, W. S., Confined $ZrO_2$ particles in $NiO{\cdot}nAl_2O_3$ spinel. *Mater. Sci. Eng., A* **1994,** *184* (1), L5-L9.
103. Üstündag, E.; Ret, P.; Subramanian, R.; Dieckmann, R.; Sass, S. L., In situ metal-ceramic microstructures by partial reduction reactions in the Ni-Al-O system and the role of $ZrO_2$. *Mater. Sci. Eng., A* **1995,** *195*, 39-50.
104. Heuer, A. H.; Claussen, N.; Kriven, W. M.; Rühle, M., Stability of Tetragonal $ZrO_2$ Particles in Ceramic Matrices. *J. Am. Ceram. Soc.* **1982,** *65* (12), 642-650.
105. Bischoff, E.; Rühle, M., Twin Boundaries in Monoclinic $ZrO_2$ Particles Confined in a Mullite Matrix. *J. Am. Ceram. Soc.* **1983,** *66* (2), 123-127.
106. Han, S. J.; Bang, Y.; Seo, J. G.; Yoo, J.; Song, I. K., Hydrogen production by steam reforming of ethanol over mesoporous $Ni–Al_2O_3–ZrO_2$ xerogel catalysts: Effect of Zr/Al molar ratio. *Int. J. Hydrogen Energy* **2013,** *38* (3), 1376-1383.
107. Zhan, Y.; Wang, Y.; Gu, D.; Chen, C.; Jiang, L.; Takehira, K., $Ni/Al_2O_3$-$ZrO_2$ catalyst for $CO_2$ methanation: The role of $\gamma$-$(Al, Zr)_2O_3$ formation. *Appl. Surf. Sci.* **2018,** *459*, 74-79.
108. Jayaram, V.; Levi, C. G.; Whitney, T.; Mehrabian, R., Characterization of $Al_2O_3{\cdot}ZrO_2$ powders produced by electrohydrodynamic atomization. *Mater. Sci. Eng., A* **1990,** *124* (1), 65-81.
109. Djuricic, B.; Pickering, S.; Glaude, P.; Mcgarry, D.; Tambuyser, P., Thermal stability of transition phases in zirconia-doped alumina. *J. Mater. Sci.* **1997,** *32* (3), 589--601.
110. Pint, B. A.; More, K. L.; Tortorelli, P. F.; Porter, W. D.; Wright, I. G., Optimizing the Imperfect Oxidation Performance of Iron Aluminides. *Mater. Sci. Forum* **2001,** *369-372*, 411-418.
111. Pint, B. A.; More, K. L.; Wright, I. G., Effect of Quaternary Additions on the Oxidation Behavior of Hf-Doped NiAl. *Oxid. Met.* **2003,** *59* (3), 257-283.

112. Hou, P. Y., Impurity Effects on Alumina Scale Growth. *J. Am. Ceram. Soc.* **2003,** *86* (4), 660-68.
113. Wu, Q.; Chan, H. M.; Rickman, J. M.; Harmer, M. P., Effect of $Hf^{4+}$ Concentration on Oxygen Grain-Boundary Diffusion in Alumina. *J. Am. Ceram. Soc.* **2015,** *98* (10), 3346-3351.
114. Yu, Z.; Wu, Q.; Rickman, J. M.; Chan, H. M.; Harmer, M. P., Atomic-resolution observation of Hf-doped alumina grain boundaries. *Scripta Mater.* **2013,** *68* (9), 703-706.
115. Behera, S. K.; Cantwell, P. R.; Harmer, M. P., A grain boundary mobility discontinuity in reactive element Zr-doped $Al_2O_3$. *Scripta Mater.* **2014,** *90-91*, 33-36.
116. Farahani, M. D.; Dasireddy, V. D. B. C.; Friedrich, H. B., Oxidative Dehydrogenation of n-Octane over Niobium-Doped $NiAl_2O_4$: An Example of Beneficial Coking in Catalysis over Spinel. *ChemCatChem* **2018,** *10* (9), 2059-2069.
117. Roh, H.-S.; Jun, K.-W.; Baek, S.-C.; Park, S.-E., A Highly Active and Stable Catalyst for Carbon Dioxide Reforming of Methane: Ni/Ce–$ZrO_2$/θ-$Al_2O_3$. *Catal. Lett.* **2002,** *81* (3), 147-151.
118. Augustin, C. O.; Hema, K.; Berchmans, L. J.; Kalai Selvan, R.; Saraswathi, R., Effect of $Ce^{4+}$ substitution on the structural, electrical and dielectric properties of $NiAl_2O_4$ spinel. *Phys. Status Solidi A* **2005,** *202* (6), 1017-1024.
119. Cai, X.; Cai, Y.; Lin, W., Autothermal reforming of methane over Ni catalysts supported over $ZrO_2$-$CeO_2$-$Al_2O_3$. *J. Nat. Gas Chem.* **2008,** *17* (2), 201-207.
120. Li, H.; Xu, H.; Wang, J., Methane reforming with $CO_2$ to syngas over $CeO_2$-promoted Ni/$Al_2O_3$-$ZrO_2$ catalysts prepared via a direct sol-gel process. *J. Nat. Gas Chem.* **2011,** *20* (1), 1-8.
121. Wolfbeisser, A.; Sophiphun, O.; Bernardi, J.; Wittayakun, J.; Föttinger, K.; Rupprechter, G., Methane dry reforming over ceria-zirconia supported Ni catalysts. *Catal. Today* **2016,** *277*, 234-245.
122. Charisiou, N. D.; Iordanidis, A.; Polychronopoulou, K.; Yentekakis, I. V.; Goula, M. A., Studying the stability of Ni supported on modified with $CeO_2$ alumina catalysts for the biogas dry reforming reaction. *Mater. Today: Proc.* **2018,** *5* (14, Part 1), 27607-27616.
123. Zhang, G.; Wang, Y.; Li, X.; Bai, Y.; Zheng, L.; Wu, L.; Han, X., Effect of Gd Promoter on the Structure and Catalytic Performance of Mesoporous Ni/$Al_2O_3$–$CeO_2$ in Dry Reforming of Methane. *Ind. Eng. Chem. Res.* **2018,** *57* (50), 17076-17085.
124. AbdelDayem, H. M.; Faiz, M.; Abdel-Samad, H. S.; Hassan, S. A., Rare earth oxides doped NiO/γ-$Al_2O_3$ catalyst for oxidative dehydrogenation of cyclohexane. *J. Rare Earths* **2015,** *33* (6), 611-618.
125. Kuznetsov, V. M.; Kadyrov, R. I.; Rudenskii, G. E., Calculation of Surface Energy of Metals and Alloys by the Electron Density Functional Method. *Journal of Material Science and Technology (Shenyang, China)* **1998,** *14*, 320-322.
126. Wen, Y.-N.; Zhang, J.-M., Surface energy calculation of the fcc metals by using the MAEAM. *Solid State Commun.* **2007,** *144* (3–4), 163-167.

127. Meltzman, H.; Chatain, D.; Avizemer, D.; Besmann, T. M.; Kaplan, W. D., The equilibrium crystal shape of nickel. *Acta Mater.* **2011,** *59* (9), 3473-3483.
128. Boudart, M., Turnover Rates in Heterogeneous Catalysis. *Chem. Rev.* **1995,** *95* (3), 661-666.
129. Fang, C. M.; Parker, S. C.; de With, G., Atomistic Simulation of the Surface Energy of Spinel $MgAl_2O_4$. *J. Am. Ceram. Soc.* **2000,** *83* (8), 2082--2084.
130. Chenna, S.; Banerjee, R.; Crozier, P. A., Atomic-scale observation of the Ni activation process for partial oxidation of methane using in situ environmental TEM. *ChemCatChem* **2011,** *3* (6), 1051-1059.
131. Yuan, W.; Zhang, D.; Ou, Y.; Fang, K.; Zhu, B.; Yang, H.; Hansen, T. W.; Wagner, J. B.; Zhang, Z.; Gao, Y.; Wang, Y., Direct In Situ TEM Visualization and Insight into the Facet-Dependent Sintering Behaviors of Gold on $TiO_2$. *Angew. Chem. Int. Ed.* **2018,** *57* (51), 16827-16831.
132. Honkanen, M.; Hansen, T. W.; Jiang, H.; Kärkkäinen, M.; Huuhtanen, M.; Heikkinen, O.; Kallinen, K.; Lahtinen, J.; Keiski, R. L.; Wagner, J. B.; Vippola, M., Electron microscopic studies of natural gas oxidation catalyst – Effects of thermally accelerated aging on catalyst microstructure. *J. Catal.* **2017,** *349*, 19-29.
133. Misture, S. T., Large-volume atmosphere-controlled high-temperature x-ray diffraction furnace. *Meas. Sci. Technol.* **2003,** *14* (7), 1091-1098.
134. Wojdyr, M., Fityk: a general-purpose peak fitting program. *J. Appl. Crystallogr.* **2010,** *43* (5-1), 1126-1128.
135. Ladonis, A. C. Deactivation and Spinel Phase Regeneration of Reduced Nickel Aluminate. Alfred University, Alfred, NY, 2016.
136. Choudhary, V. R.; Uphade, B. S.; Pataskar, S. G.; Keshavaraja, A., Low-Temperature Complete Combustion of Methane over Mn-, Co-, and Fe-Stabilized $ZrO_2$. *Angew. Chem., Int. Ed. Engl.* **1996,** *35* (20), 2393-2395.
137. Choudhary, V. R.; Banerjee, S.; Pataskar, S. G., Combustion of dilute propane over transition metal-doped $ZrO_2$ (cubic) catalysts. *Appl. Catal., A* **2003,** *253* (1), 65-74.
138. Yamasaki, M.; Habazaki, H.; Yoshida, T.; Akiyama, E.; Kawashima, A.; Asami, K.; Hashimoto, K.; Komori, M.; Shimamura, K., Compositional dependence of the $CO_2$ methanation activity of Ni/ZrO2 catalysts prepared from amorphous NiZr alloy precursors. *Appl. Catal., A* **1997,** *163* (1), 187-197.
139. Chang, W. S.; Chen, S.; Shen, P., Phase equilibria of zirconia-dispersed ceramic in $NiO$-$Al_2O_3$-$ZrO_2$ system. *Materials Science and Engineering: A* **1991,** *145* (1), 113-118.
140. Wang, J. Effects of transition metal oxide addition on sintering, creep, and fracture properties in alumina. Cornell University, Ithaca, NY, 1991.
141. Wang, J.; Raj, R., Interface effects in superplastic deformation of alumina containing zirconia, titania or hafnia as a second phase. *Acta Metall. Mater.* **1991,** *39* (11), 2909-2919.
142. Jacob, K. T.; Alcock, C. B., Activities and their relation to cation distribution in $NiAl_2O_4$-$MgAl_2O_4$ spinel solid solutions. *J. Solid State Chem.* **1977,** *20* (1), 79-88.
143. Ghule, A. V.; Ghule, K.; Punde, T.; Liu, J.-Y.; Tzing, S.-H.; Chang, J.-Y.; Chang, H.; Ling, Y.-C., In situ monitoring of $NiO–Al_2O_3$ nanoparticles synthesis by thermo-Raman spectroscopy. *Mater. Chem. Phys.* **2010,** *119* (1), 86-92.

144. Pettit, F. S.; Randklev, E. H.; Felten, E. J., Formation of $NiAl_2O_4$ by Solid State Reaction. *J. Am. Ceram. Soc.* **1966,** *49* (4), 199-203.
145. Hirota, K.; Komatsu, W., Concurrent Measurement of Volume, Grain-Boundary, and Surface Diffusion Coefficients in the System NiO-$Al_2O_3$. *J. Am. Ceram. Soc.* **1977,** *60* (3-4), 105-107.
146. Cynn, H.; Sharma, S. K.; Cooney, T. F.; Nicol, M., High-temperature Raman investigation of order-disorder behavior in the $MgAl_2O_4$ spinel. *Phys. Rev. B: Condens. Matter* **1992,** *45* (1), 500-502.
147. Slotznick, S. P.; Shim, S.-H., In situ Raman spectroscopy measurements of $MgAl_2O_4$ spinel up to 1400 °C. *Am. Mineral.* **2008,** *93* (2-3), 470-476.
148. White, W. B.; DeAngelis, B. A., Interpretation of the vibrational spectra of spinels. *Spectrochim. Acta, Part A* **1967,** *23* (4), 985-995.
149. Gupta, H. C.; Parashar, A.; Gupta, V. B.; Tripathi, B. B., Lattice Vibrations in Spinel-Type Compounds $CdCr_2S_4$ and $CdCr_2Se_4$. *Phys. Status Solidi B* **1990,** *160* (1), K19-K24.
150. Preudhomme, J.; Tarte, P., Infrared studies of spinels—I: A critical discussion of the actual interpretations. *Spectrochim. Acta, Part A* **1971,** *27* (7), 961-968.
151. Preudhomme, J.; Tarte, P., Infrared studies of spinels—IV: Normal spinels with a high-valency tetrahedral cation. *Spectrochim. Acta, Part A* **1972,** *28* (1), 69-79.
152. Preudhomme, J.; Tarte, P., Infrared studies of spinels—III: The normal II–III spinels. *Spectrochim. Acta, Part A* **1971,** *27* (9), 1817-1835.
153. Cynn, H.; Anderson, O. L.; Nicol, M., Effects of cation disordering in a natural $MgAl_2O_4$ spinel observed by rectangular parallelepiped ultrasonic resonance and Raman measurements. *Pure Appl. Geophys.* **1993,** *141* (2), 415-444.
154. Baronskiy, M.; Rastorguev, A.; Zhuzhgov, A.; Kostyukov, A.; Krivoruchko, O.; Snytnikov, V., Photoluminescence and Raman spectroscopy studies of low-temperature γ-$Al_2O_3$ phases synthesized from different precursors. *Opt. Mater.* **2016,** *53*, 87-93.
155. Dyer, C.; Hendra, P. J.; Forsling, W.; Ranheimer, M., Surface hydration of aqueous γ-$Al_2O_3$ studied by Fourier transform Raman and infrared spectroscopy—I. Initial results. *Spectrochim. Acta, Part A* **1993,** *49* (5), 691-705.
156. Vuurman, M. A.; Wachs, I. E., In situ Raman spectroscopy of alumina-supported metal oxide catalysts. *J. Phys. Chem.* **1992,** *96* (12), 5008-5016.
157. Laha, T.; Balani, K.; Agarwal, A.; Patil, S.; Seal, S., Synthesis of nanostructured spherical aluminum oxide powders by plasma engineering. *Metall. Mater. Trans. A* **2005,** *36* (2), 301-309.
158. Kim, H.; Kosuda, K. M.; Van Duyne, R. P.; Stair, P. C., Resonance Raman and surface- and tip-enhanced Raman spectroscopy methods to study solid catalysts and heterogeneous catalytic reactions. *Chem. Soc. Rev.* **2010,** *39* (12), 4820-4844.
159. Liu, Y.; Cheng, B.; Wang, K.-K.; Ling, G.-P.; Cai, J.; Song, C.-L.; Han, G.-R., Study of Raman spectra for γ-$Al_2O_3$ models by using first-principles method. *Solid State Commun.* **2014,** *178*, 16-22.
160. Gil-Calvo, M.; Jiménez-González, C.; de Rivas, B.; Gutiérrez-Ortiz, J. I.; López-Fonseca, R., Effect of Ni/Al molar ratio on the performance of substoichiometric $NiAl_2O_4$ spinel-based catalysts for partial oxidation of methane. *Appl. Catal., B* **2017,** *209*, 128-138.

161. Wang, S. R.; Shen, P., On the Spinel Precipitation in Al-Doped $Ni_{1-x}O$. *J. Solid State Chem.* **1998,** *140* (1), 38-45.
162. Davies, M. J.; Parker, S. C.; Watson, G. W., Atomistic simulation of the surface structure of spinel. *J. Mater. Chem.* **1994,** *4* (6), 813-816.
163. Hasan, M. M.; Dholabhai, P. P.; Castro, R. H. R.; Uberuaga, B. P., Stabilization of $MgAl_2O_4$ spinel surfaces via doping. *Surf. Sci.* **2016,** *649*, 138-145.
164. Phillips, B.; Hutta, J. J.; Warshaw, I., Phase Equilibria in the System NiO–$Al_2O_3$–$SiO_2$. *J. Am. Ceram. Soc.* **1963,** *46* (12), 579-583.
165. Alper, A.; McNally, R.; Ribbe, P.; Doman, R., The system MgO–$MgAl_2O_4$. *J. Am. Ceram. Soc.* **1962,** *45* (6), 263-268.
166. Zhang, J.; Wang, H.; Dalai, A. K., Effects of metal content on activity and stability of Ni-Co bimetallic catalysts for $CO_2$ reforming of $CH_4$. *Appl. Catal., A* **2008,** *339* (2), 121-129.
167. Davis, M. E.; Davis, R. J., *Fundamentals of chemical reaction engineering*. Courier Corporation: 2012.
168. Gilman, J. J., Dislocation Sources in Crystals. *J. Appl. Phys.* **1959,** *30* (10), 1584-1594.
169. Morita, K.; Hiraga, K.; Kim, B.-N.; Suzuki, T. S.; Sakka, Y., Strain Softening and Hardening during Superplastic-Like Flow in a Fine-Grained $MgAl_2O_4$ Spinel Polycrystal. *J. Am. Ceram. Soc.* **2004,** *87* (6), 1102-1109.
170. Shintani, T.; Murata, Y., Evaluation of the dislocation density and dislocation character in cold rolled Type 304 steel determined by profile analysis of X-ray diffraction. *Acta Mater.* **2011,** *59* (11), 4314-4322.
171. Berecz, T.; Jenei, P.; Csóré, A.; Lábár, J.; Gubicza, J.; Szabó, P. J., Determination of dislocation density by electron backscatter diffraction and X-ray line profile analysis in ferrous lath martensite. *Mater. Charact.* **2016,** *113*, 117-124.
172. Ameri, A. A. H.; Elewa, N. N.; Ashraf, M.; Escobedo-Diaz, J. P., General methodology to estimate the dislocation density from microhardness measurements. *Mater. Charact.* **2017,** *131*, 324-330.
173. Ikuhara, Y., Oxide Ceramics with High Density Dislocations and Their Properties. *Mater. Trans., JIM* **2009,** *50* (7), 1626-1632.
174. Donlon, W. T.; Mitchell, T. E.; Heuer, A. H., Work softening in stoichiometric spinel ($MgAl_2O_4$). *Philos. Mag. A* **1982,** *45* (6), 1013-1036.
175. Rogers, K. A.; Trumble, K. P., Effect of reduction temperature on internal reduction microstructures. *Scripta Mater.* **1998,** *39* (1), 103-108.
176. Li, L.; Howard, C.; King, D. L.; Gerber, M.; Dagle, R.; Stevens, D., Regeneration of Sulfur Deactivated Ni-Based Biomass Syngas Cleaning Catalysts. *Ind. Eng. Chem. Res.* **2010,** *49* (20), 10144-10148.
177. Gaskell, D. R.; Laughlin, D. E., *Introduction to the Thermodynamics of Materials*. CRC Press: 2017.
178. Ando, K.; Oishi, Y., Self-diffusion coefficients of oxygen ion in single crystals of $MgO{\cdot}nAl_2O_3$ spinels. *J. Chem. Phys.* **1974,** *61* (2), 625-629.
179. Oishi, Y.; Ando, K., Self-diffusion of oxygen in polycrystalline $MgAl_2O_4$. *J. Chem. Phys.* **1975,** *63* (1), 376-378.

180. Murphy, S. T.; Uberuaga, B. P.; Ball, J. B.; Cleave, A. R.; Sickafus, K. E.; Smith, R.; Grimes, R. W., Cation diffusion in magnesium aluminate spinel. *Solid State Ionics* **2009,** *180* (1), 1-8.
181. Richardson, J. T.; Crump, J. G., Crystallite size distributions of sintered nickel catalysts. *J. Catal.* **1979,** *57* (3), 417-425.
182. DeLaRiva, A. The sintering and stability of catalytic nano-particles. University of New Mexico, Albuquerque, New Mexico, 2010.
183. Gruber, E. E., Calculated Size Distributions for Gas Bubble Migration and Coalescence in Solids. *J. Appl. Phys.* **1967,** *38* (1), 243-250.
184. Wynblatt, P.; Gjostein, N. A., Supported metal crystallites. *Prog. Solid State Chem.* **1975,** *9*, 21-58.
185. Trumble, K. P.; Rühle, M., The thermodynamics of spinel interphase formation at diffusion-bonded Ni/$Al_2O_3$ interfaces. *Acta Metall. Mater.* **1991,** *39* (8), 1915-1924.
186. Fricke, R.; Weitbrecht, G., Die Gleichgewichte $CO_2$/CO gegen Ni/NiO, bzw. Ni + $\gamma$-$Al_2O_3$/$NiAl_2O_4$ und ihre Beeinflussung durch den physikalischen Zustand der festen Reaktionsteilnehmer. *Zeitschrift für Elektrochemie und angewandte physikalische Chemie* **1942,** *48* (2), 87-106.
187. Navrotsky, A.; Ma, C.; Lilova, K.; Birkner, N., Nanophase Transition Metal Oxides Show Large Thermodynamically Driven Shifts in Oxidation-Reduction Equilibria. *Science* **2010,** *330* (6001), 199.
188. Harmer, M. P.; Mishra, R. K.; Thomas, G., Electron Microscopy of Annealed (Ni, Zn, Co)$Fe_2O_4$. *J. Am. Ceram. Soc.* **1983,** *66* (3), C-44-C-45.
189. Davies, P. K.; Mackinnon, I. D., Oxide Reduction in NiO-Containing Solid-Solution Systems During Transmission Electron Microscopy. *J. Am. Ceram. Soc.* **1986,** *69* (6), C-124-C-125.
190. Nagaoka, K.; Takanabe, K.; Aika, K.-i., Modification of Co/$TiO_2$ for dry reforming of methane at 2MPa by Pt, Ru or Ni. *Appl. Catal., A* **2004,** *268* (1), 151-158.
191. Takanabe, K.; Nagaoka, K.; Nariai, K.; Aika, K.-i., Titania-supported cobalt and nickel bimetallic catalysts for carbon dioxide reforming of methane. *J. Catal.* **2005,** *232* (2), 268-275.
192. Zhang, J.; Wang, H.; Dalai, A. K., Kinetic Studies of Carbon Dioxide Reforming of Methane over Ni−Co/Al−Mg−O Bimetallic Catalyst. *Ind. Eng. Chem. Res.* **2009,** *48* (2), 677-684.
193. Fabrichnaya, O.; Mercer, C., Phase relations in the $HfO_2$–$Y_2O_3$–$Al_2O_3$ system. *Calphad* **2005,** *29* (3), 239-246.
194. Saxton, M. J., Anomalous diffusion due to obstacles: a Monte Carlo study. *Biophys. J.* **1994,** *66* (2, Part 1), 394-401.
195. Li, Y.; Liu, C.; Zhang, T.; Jiang, M.; Peng, C., Thermodynamic assessment of $Al_2O_3$–$SiO_2$–$Ce_2O_3$ system. *Metall. Res. Technol.* **2017,** *114* (3).
196. Serrazina, R.; Dean, J. S.; Reaney, I. M.; Pereira, L.; Vilarinho, P. M.; Senos, A. M. O. R., Mechanism of densification in low-temperature FLASH sintered lead free potassium sodium niobate (KNN) piezoelectrics. *J. Mater. Chem.* **2019,** *7* (45), 14334-14341.
197. Stokkan, T. Structural investigation of a Ni-Nb-O phase by electron diffraction. University of Oslo, Oslo, Norway, 2011.

198. Shannon, R., Revised effective ionic radii and systematic studies of interatomic distances in halides and chalcogenides. *Acta Crystallogr. Sect. A: Found. Crystallogr.* **1976,** *32* (5), 751-767.
199. Kofstad, P.; Ruzicka, D., On the defect structure of $ZrO_2$ and $HfO_2$. *J. Electrochem. Soc.* **1963,** *110* (3), 181-184.
200. Wolten, G. M., Diffusionless Phase Transformations in Zirconia and Hafnia. *J. Am. Ceram. Soc.* **1963,** *46* (9), 418-422.
201. Vest, R. W.; Tallan, N. M., Electrical Properties and Defect Structure of Zirconia: II, Tetragonal Phase and Inversion. *J. Am. Ceram. Soc.* **1965,** *48* (9), 472-475.
202. Aldebert, P.; Traverse, J.-P., Structure and Ionic Mobility of Zirconia at High Temperature. *J. Am. Ceram. Soc.* **1985,** *68* (1), 34-40.
203. Bratton, R. J., Initial Sintering Kinetics of $MgAl_2O_4$. *J. Am. Ceram. Soc.* **1969,** *52* (8), 417-419.
204. Linder, R., Åkerstrom, Å., Diffusion von $^{63}Ni$ in Nickelspinellen. *Z. Phys. Chem.* **1958,** *18* (5_6), 303.
205. Moon, S. K.; Komatsu, W., Concurrent Measurement of Surface and Volume Diffusion Coefficients in the Ni–Al Spinel Formation Reaction. *Z. Phys. Chem.* **1974,** *89* (1-4), 47-54.
206. Atkinson, A.; Taylor, R. I., The diffusion of $^{63}Ni$ along grain boundaries in nickel oxide. *Philos. Mag. A* **1981,** *43* (4), 979-998.
207. Chiang, Y.-M.; Kingery, W. D., Grain-Boundary Migration in Nonstoichiometric Solid Solutions of Magnesium Aluminate Spinel: I, Grain Growth Studies. *J. Am. Ceram. Soc.* **1989,** *72* (2), 271-277.
208. Chiang, Y.-M.; Kingery, W. D., Grain-Boundary Migration in Nonstoichiometric Solid Solutions of Magnesium Aluminate Spinel: II, Effects of Grain-Boundary Nonstoichiometry. *J. Am. Ceram. Soc.* **1990,** *73* (5), 1153-1158.
209. Sheng, Y. J.; Wasserburg, G. J.; Hutcheon, I. D., Self-diffusion of magnesium in spinel and in equilibrium melts: Constraints on flash heating of silicates. *Geochim. Cosmochim. Acta* **1992,** *56* (6), 2535-2546.
210. Andre, M.; Hermann, S., Diffusion und Fehlordnung in Spinellen. *Z. Phys. Chem.* **1962,** *32* (1_2), 76-90.
211. Suzuki, A. M.; Yasuda, A.; Ozawa, K., Cr and Al diffusion in chromite spinel: experimental determination and its implication for diffusion creep. *Phys. Chem. Miner.* **2008,** *35* (8), 433.
212. Miller, M. Nanoporous glass-ceramics for gas separation. Ph.D. Thesis, Alfred University, Alfred, NY, 2008.
213. Vogt, K.; Dohmen, R.; Chakraborty, S., Fe-Mg diffusion in spinel: New experimental data and a point defect model. *Am. Mineral.* **2015,** *100* (10), 2112-2122.
214. Liermann, H.-P.; Ganguly, J., Diffusion kinetics of $Fe^{2+}$ and Mg in aluminous spinel: experimental determination and applications. *Geochim. Cosmochim. Acta* **2002,** *66* (16), 2903-2913.
215. Murphy, S. T. Atomistic simulation of defects and diffusion in oxides. PhD, Imperial College, London, U.K., 2009.
216. Murphy, S. T.; Gilbert, C. A.; Smith, R.; Mitchell, T. E.; Grimes, R. W., Non-stoichiometry in $MgAl_2O_4$ spinel. *Philos. Mag. A* **2010,** *90* (10), 1297-1305.

217. Gan, L.-Y.; Akande, S. O.; Schwingenschlögl, U., Anisotropic O vacancy formation and diffusion in $LaMnO_3$. *J. Mater. Chem.* **2014,** *2* (46), 19733-19737.
218. Kubicek, M.; Cai, Z.; Ma, W.; Yildiz, B.; Hutter, H.; Fleig, J., Tensile Lattice Strain Accelerates Oxygen Surface Exchange and Diffusion in $La_{1-x}Sr_xCoO_{3-\delta}$ Thin Films. *ACS Nano* **2013,** *7* (4), 3276-3286.
219. Kim, S. J.; Akbay, T.; Matsuda, J.; Takagaki, A.; Ishihara, T., Strain Effects on Oxygen Reduction Activity of $Pr_2NiO_4$ Caused by Gold Bulk Dispersion for Low Temperature Solid Oxide Fuel Cells. *ACS Appl. Energy Mater.* **2019,** *2* (2), 1210-1220.
220. Newbury, D. E.; Ritchie, N. W. M., Performing elemental microanalysis with high accuracy and high precision by scanning electron microscopy/silicon drift detector energy-dispersive X-ray spectrometry (SEM/SDD-EDS). *J Mater Sci* **2014,** *50* (2), 493-518.
221. Ritchie, N.; Davis, J.; Newbury, D., DTSA-II: A New Tool for Simulating and Quantifying EDS Spectra - Application to Difficult Overlaps. *Microsc. Microanal.* **2008,** *14* (Supplement S2), 1176-1177.
222. Ritchie, N. W. M., A new Monte Carlo application for complex sample geometries. *Surf. Interface Anal.* **2005,** *37*, 1006-1011.
223. Ritchie, N. W. M., Using DTSA-II to Simulate and Interpret Energy Dispersive Spectra from Particles. *Microsc. Microanal.* **2010,** *16* (3), 248-58.
224. Ritchie, N. W. M., Spectrum Simulation in DTSA-II. *Microsc. Microanal.* **2009,** *15* (5), 454-68.
225. Docherty, F. T.; Craven, A. J.; McComb, D. W.; Skakle, J., ELNES investigations of the oxygen K-edge in spinels. *Ultramicroscopy* **2001,** *86* (3), 273-288.
226. Suenaga, K.; Bouchet, D.; Colliex, C.; Thorel, A.; Brandon, D. G., Investigations of alumina/spinel and alumina/ zirconia interfaces by spatially resolved electron energy loss spectroscopy. *J. Eur. Ceram. Soc.* **1998,** *18* (10), 1453-1459.
227. Bruley, J.; Tseng, M.-W.; Williams, D. B., Spectrum-Line Profile Analysis of a Magnesium Aluminate Spinel Sapphire Interface. *Microsc. Microanal. Microstruct.* **1995,** *6* (1), 1-18.
228. Docherty, F. T. ELNES investigation of spinels. University of Glasgow, Glasgow, U.K., 2001.
229. van Benthem, K.; Kohl, H., Methods for ELNES-quantification: characterization of the degree of inversion of Mg–Al-spinels. *Micron* **2000,** *31* (4), 347-354.
230. de Groot, F. M. F.; Grioni, M.; Fuggle, J. C.; Ghijsen, J.; Sawatzky, G. A.; Petersen, H., Oxygen 1s x-ray-absorption edges of transition-metal oxides. *Phys. Rev. B: Condens. Matter* **1989,** *40* (8), 5715-5723.
231. Brydson, R.; Mullejans, H.; Bruley, J.; Trusty, P. A.; Sun, X.; Yeomans, J. A.; Rühle, M., Spatially resolved electron energy-loss studies of metal–ceramic interfaces in transition metal/alumina cermets. *J. Microsc. (Oxford, U.K.)* **1995,** *177* (3), 369-386.
232. Ostanin, S.; Craven, A. J.; McComb, D.; Vlachos, D.; Alavi, A.; Finnis, M.; Paxton, A., Effect of relaxation on the oxygen K-edge electron energy-loss near-edge structure in yttria-stabilized zirconia. *Phys. Rev. B* **2000,** *62*.

233. Vlachos, D.; Craven, A. J.; McComb, D. W., The influence of dopant concentration on the oxygen K-edge ELNES and XANES in yttria-stabilized zirconia. *J. Phys.: Condens. Matter* **2001,** *13* (48), 10799-10809.
234. Ayoola, H.; Li, C.-H.; House, S.; Kas, J.; Rehr, J.; Jinschek, J.; Saidi, W.; Yang, J.; Bonifacio, C., Probing the Cation Distribution in Gamma-Alumina Enabled by O-K Edge Artifact Suppression Using Cryo-EELS. *Microsc. Microanal.* **2020**, 1-3.
235. Ayoola, H. O.; Bonifacio, C. S.; Curnan, M. T.; House, S. D.; Li, M.; Kas, J.; Rehr, J. J.; Stach, E. A.; Saidi, W. A.; Yang, J. C., Determination of the Crystal Structure of Gamma-Alumina by Electron Diffraction and Electron Energy-Loss Spectroscopy. *Microsc. Microanal.* **2019,** *25* (S2), 2036-2037.
236. Ayoola, H. O.; Bonifacio, C. S.; Zhu, Q.; Li, C.-H.; House, S. D.; Kas, J. J.; Jinschek, J.; Rehr, J. J.; Saidi, W. A.; Yang, J. C., Probing the Local Bonding at the Pt/$\gamma$-$Al_2O_3$ Interface. *J. Phys. Chem. C* **2020,** *124* (18), 9876-9885.
237. Engelhart, W.; Dreher, W.; Eibl, O.; Schier, V., Deposition of alumina thin film by dual magnetron sputtering: Is it $\gamma$-$Al_2O_3$? *Acta Mater.* **2011,** *59* (20), 7757-7767.
238. Vand, V.; Hanoka, J. I., Epitaxial theory of polytypism; observations on the growth of $PbI_2$ crystals. *Mater. Res. Bull.* **1967,** *2* (2), 241-251.
239. Forty, A. J., The growth of cadmium iodide crystals: I—Dislocations and spiral growth. *Philos. Mag. A* **1952,** *43* (336), 72-81.
240. Baronnet, A., Sur les origines des dislocations vis et des spirales de croissance dans les micas. *J. Cryst. Growth* **1973,** *19* (3), 193-198.
241. Strunk, H. P.; Dorsch, W.; Heindl, J., The Nature of Micropipes in 6H-SiC Single Crystals. *Adv. Eng. Mater.* **2000,** *2* (6), 386-389.
242. Stein, R. A., Formation of macrodefects in SiC. In *Wide-Band-Gap Semiconductors*, Van de Walle, C. G., Ed. Elsevier: Amsterdam, 1993; pp 211-216.
243. Scholz, R.; Gösele, U.; Niemann, E.; Leidich, D., Carbonization-induced SiC micropipe formation in crystalline Si. *Appl. Phys. Lett.* **1995,** *67* (10), 1453-1455.
244. Scholz, R.; Gösele, U.; Niemann, E.; Wischmeyer, F., Micropipes and voids at $\beta^{-}$SiC/Si(100) interfaces: an electron microscopy study. *Appl. Phys. A* **1997,** *64* (2), 115-125.
245. Liliental-Weber, Z.; Chen, Y.; Ruvimov, S.; Swider, W.; Washburn, J., Nano-Tubes in GaN. *MRS Online Proc. Libr.* **1996,** *449*, 417.
246. Büttner, C. C.; Langner, A.; Geuss, M.; Müller, F.; Werner, P.; Gösele, U., Formation of Straight 10 nm Diameter Silicon Nanopores in Gold Decorated Silicon. *ACS Nano* **2009,** *3* (10), 3122-3126.
247. Kirkendall, E., Diffusion of zinc in alpha brass. *Trans. AIME* **1942,** *147*, 104-110.
248. Kirkendall, E., Rates of diffusion of copper and zinc in alpha brass. *Trans. AIME* **1939,** *133*, 186-203.
249. Kirkendall, E.; Smigelskas, A., Zinc diffusion in alpha brass. *Aime Trans* **1947,** *171*, 130-142.
250. Yin, Y.; Rioux, R. M.; Erdonmez, C. K.; Hughes, S.; Somorjai, G. A.; Alivisatos, A. P., Formation of Hollow Nanocrystals Through the Nanoscale Kirkendall Effect. *Science* **2004,** *304* (5671), 711.

251. Fan, H. J.; Gösele, U.; Zacharias, M., Formation of Nanotubes and Hollow Nanoparticles Based on Kirkendall and Diffusion Processes: A Review. *Small* **2007,** *3* (10), 1660-1671.
252. Dehdari Vais, R.; Heli, H., The Kirkendall Effect: its Efficacy in the Formation of Hollow Nanostructures. *J. Biol. Today's World* **2016,** *5* (8).
253. Fan, H.; Knez, M.; Scholz, R.; Nielsch, K.; Pippel, E.; Hesse, D.; Gösele, U.; Zacharias, M., Single-crystalline $MgAl_2O_4$ spinel nanotubes using a reactive and removable MgO nanowire template. *Nanotechnology* **2006,** *17* (20), 5157-5162.
254. Fan, H. J.; Knez, M.; Scholz, R.; Nielsch, K.; Pippel, E.; Hesse, D.; Zacharias, M.; Gösele, U., Monocrystalline spinel nanotube fabrication based on the Kirkendall effect. *Nat. Mater.* **2006,** *5* (8), 627-631.
255. Fan, H. J.; Knez, M.; Scholz, R.; Hesse, D.; Nielsch, K.; Zacharias, M.; Gösele, U., Influence of Surface Diffusion on the Formation of Hollow Nanostructures Induced by the Kirkendall Effect: The Basic Concept. *Nano Lett.* **2007,** *7* (4), 993-997.
256. Garcia-Barriocanal, J.; Rivera-Calzada, A.; Varela, M.; Sefrioui, Z.; Iborra, E.; Leon, C.; Pennycook, S. J.; Santamaria, J., Colossal Ionic Conductivity at Interfaces of Epitaxial $ZrO_2$:$Y_2O_3$/$SrTiO_3$ Heterostructures. *Science* **2008,** *321* (5889), 676.
257. Kushima, A.; Yip, S.; Yildiz, B., Competing strain effects in reactivity of $LaCoO_3$ with oxygen. *Phys. Rev. B: Condens. Matter* **2010,** *82* (11), 115435.
258. Han, J. W.; Yildiz, B., Enhanced one dimensional mobility of oxygen on strained $LaCoO_3$ (001) surface. *J. Mater. Chem.* **2011,** *21* (47), 18983.
259. Schichtel, N.; Korte, C.; Hesse, D.; Janek, J., Elastic strain at interfaces and its influence on ionic conductivity in nanoscaled solid electrolyte thin films—theoretical considerations and experimental studies. *PCCP* **2009,** *11* (17), 3043.
260. Ando, K.; Oishi, Y., Effect of Ratio of Surface Area to Volume on Oxygen Self-Diffusion Coefficients Determined for Crushed MgO-$Al_2O_3$ Spinels. *J. Am. Ceram. Soc.* **1983,** *66* (8), C-131-C-132.

# VII. APPENDIX

Below are permalinks to each video used in this thesis. Digital media hard copies (flash drive or CD-ROM) are included with the physical copy of this thesis. All compositions have an implied 2.5 wt. % $ZrO_2$ unless otherwise stated.

### Particle Migration and Coalesence Videos

$NiAl_2O_4$ Parent Oxide – https://ensemble.alfred.edu/Watch/y8H4BnNq

$NiAl_2O_4$ Reduced 900°C (Low Mag) – https://ensemble.alfred.edu/Watch/w8Z3SqCt

$NiAl_2O_4$ Reduced 900°C (High Mag) – https://ensemble.alfred.edu/Watch/Nf5o6C4R

$NiAl_2O_4$ Reduced 750°C – https://ensemble.alfred.edu/Watch/Mw56PzTx

$NiAl_2O_4$ Reduced 800°C – https://ensemble.alfred.edu/Watch/Na78HiDc

$Ni_{0.25}Mg_{0.75}Al_2O_4$ Reduced 800°C – https://ensemble.alfred.edu/Watch/d9R8Fmt2

### Tunneling Videos

$NiAl_2O_4$ (Spike 1100°C) – https://ensemble.alfred.edu/Watch/Mf2p6F4C

$Ni_{0.375}Co_{0.375}Mg_{0.25}Al_2O_4$ – https://ensemble.alfred.edu/Watch/Dx23Xdc6

$Ni_{0.50}Mg_{0.50}NiAl_2O_4$ – need link yet

$NiAl_2O_4$ + 2.5 wt. % $HfO_2$ – https://ensemble.alfred.edu/Watch/Hw78RmCa

$MgAl_2O_4$ – https://ensemble.alfred.edu/Watch/f7R9Ttp4